

AFOSR-TR- 79 - 1807

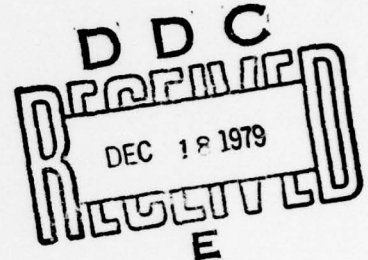
Lamont-Doherty Geological Observatory,
~~of Columbia University~~
Palisades, New York 10964

AD A078981

LEVEL II

THE USE OF PULSE SHAPES IN SEISMIC BODY WAVES,
TO DETERMINE THE NATURE OF THE SEISMIC SOURCE

Final Technical Report
Contract F49620-77-C-0098



The views and conclusions contained in this document are those of the authors and should not be interpreted as necessarily representing the official policies, either expressed or implied, of the Defense Advanced Research Projects Agency or the U.S. Government.

31 March 1979

Sponsored by
Advanced Research Projects Agency (DOD)
ARPA Order No. 3291

Monitored by AFOSR Under Contract # F49620-77-C-0098

DDC FILE COPY

404 497
Approved for public release;
distribution unlimited.

79 12 18 29

UNCLASSIFIED		READ INSTRUCTIONS BEFORE COMPLETING FORM
1. REPORT NUMBER AFOSR/TK-79-1307		2. GOVT ACCESSION NO.
3. TITLE (and Subtitle) The Use of Pulse Shapes in Seismic Body Waves, to Determine the Nature of the Seismic Source,		4. RECIPIENT'S CATALOG NUMBER 9
5. AUTHOR(s) Paul G. Richards, JO L. Boatwright Leigh House		6. TYPE OF REPORT & PERIOD COVERED Final Technical Report, 1 April 1977 - 31 March 1979
7. PERFORMING ORGANIZATION NAME AND ADDRESS Columbia Univ. in the City of New York, Box 20, Low Memorial Library, New York, N.Y. 10027 (Lamont-Doherty Geological Observatory, Palisades, New York 10964)		8. CONTRACT OR GRANT NUMBER(s) F49620-77-C-0098, ARPA Order-3291
9. CONTROLLING OFFICE NAME AND ADDRESS DARPA/NMR 1400 Wilson Blvd. Arlington, VA 22209		10. PROGRAM ELEMENT, PROJECT, TASK AREA & WORK UNIT NUMBERS 62107E 7F10 A.C. 3291-06
11. MONITORING AGENCY NAME & ADDRESS (if different from Controlling Office) AFOSR/NP Bolling AFB, Bldg. #410 Wash DC 20332		12. REPORT DATE 31 Mar 1979
13. DISTRIBUTION STATEMENT (of this Report) Approved for public release; distribution unlimited.		14. NUMBER OF PAGES 114
15. SECURITY CLASS. (of this report) Unclassified		16. DECLASSIFICATION/DOWNGRADING SCHEDULE
17. DISTRIBUTION STATEMENT (of the abstract entered in Block 20, if different from Report)		
18. SUPPLEMENTARY NOTES		
19. KEY WORDS (Continue on reverse side if necessary and identify by block number) Seismic body waves Seismic sources Slip function for earthquakes		
20. ABSTRACT (Continue on reverse side if necessary and identify by block number) We describe some new and practical methods for using seismic body waves set up by an earthquake to learn about the motions which must have occurred at the seismic source. The method entails working with recordings of the ob- served pulse shape of ground motion, and matching this with synthetics that are appropriate for a fracture theory of earthquake faulting. We describe the theory, the details of the data analysis, and applications to several different earthquakes.		

Final Technical Report

ARPA Order Number: 3291
Program Code Number: 7F10
Contractor: The Trustees of Columbia University
in the City of New York
Effective Date of Contract: 1 April 1977
Contract Expiration Date: 30 September 1978
Amount of Contract: \$61,992
Contract Number: F49620-77-C-0098
Principal Investigator: Prof. Paul G. Richards
914-359-2900 x 389
Program Manager: Prof. Paul G. Richards
914-359-2900 x 389
Short Title: Pulse Shapes and the Nature of the
Seismic Source

Sponsored by
Advanced Research Projects Agency (DOD)
ARPA Order No. 3291
Monitored by AFOSR Under Contract # F49620-77-C-0098

AIR FORCE OFFICE OF SCIENTIFIC RESEARCH (AFSC)
NOTICE OF TRANSMITTAL TO DDC
This technical report has been reviewed and is
approved for public release in accordance with FAR 101-12 (7b).
Distribution is unlimited.
A. D. BLOSE
Technical Information Officer

TECHNICAL REPORT SUMMARY

In this contract, we set out to find practical methods of using the pulse shape of observed seismic body waves to infer as much as possible about the motions which must have occurred at the seismic source itself. Previous attempts on this problem had given insufficient attention to the constraints which follow from requiring a physically plausible stress on the fault plane. We believe we have made substantial progress towards the solution of this problem. Full details of what we have done are contained in papers already published or now in preparation. It is likely that a total of six papers will result from the support provided by this contract. They are as follows:

(i) *Detailed Spectral Analysis of Two Small New York Earthquakes*, by J. Boatwright, published in the Bulletin of the Seismological Society of America, 68, 1117-1131, 1978. This work was described in full in a previous semi-annual report. It gave a complete account of the inversion of amplitude spectra of strong-motion accelerograms obtained at epicentral distances of only about 1 kilometer, to obtain source dimensions and stress drops for two events in the eastern U.S.

(ii) *A Spectral Theory for Circular Seismic Sources; Simple Estimates of Source Dimension, Effective Stress and Radiated Seismic Energy*, by J. Boatwright, submitted for publication in the Bulletin of the Seismological Society of America. This work was described in full in a previous semi-annual report. It described the pulse shapes to be expected for a fault rupture which initiated at a point and subsequently grew as an expanding circle. A variety of stopping mechanisms were discussed, and it was shown that a useful method of data processing involved working with the square of the observed particle velocity recorded at a given station.

(iii) *Quasi-Dynamic Models of Simple Earthquakes and the Implications of Energy Flux Pulse Shapes as Modelling Constraints*, by J. Boatwright, now in final stages of preparation for submission probably to the Bulletin of the Seismological Society of America. A copy of this manuscript is included in this report. A model of fault slip that is satisfactory during stages of rupture, healing and stopping is discussed in terms of the far-field pulse shapes it will generate. An application is given for two earthquakes which occurred in Alaska. Estimates are given of rupture velocity and stress release.

(iv) *Investigations of Two High Stress-Drop Earthquakes in the Shumagin Seismic Gap, Alaska*, by L. House and J. Boatwright. It is currently intended that this paper will be submitted for publication in the Journal of Geophysical Research. A copy of the manuscript is given in this report. It is inferred that the two earthquakes analysed had stress-drops in excess of 500 bars.

(v) *Body Wave Analysis of the St. Elias Earthquake*, section written by J. Boatwright for inclusion (with contributions from other authors) in a major paper on this large and recent event. From the far-field pulse shapes, it was inferred that three separate sub-events could be distinguished within this rupture. A copy of the manuscript is included in this report.

(vi) *Elementary Solutions to Lamb's Problem for a Point Source and Their Relevance to the Study of Spontaneous Crack Propagation in Three Dimensions*, by Paul G. Richards, accepted for publication in the August 1979 issue of the Bulletin of the Seismological Society of America. In order to determine the slip occurring on a rupturing fault plane, the dynamic consideration of effects of initial stress and varying fault strength can be handled if a certain fundamental problem in elasticity theory is solved in a fashion that admits rapid computation of the solution. This paper (a copy is included in this report) gives such a solution, and discusses its significance in the analysis of rupturing fault planes.

The four sections that follow are the expanded accounts of (iii), (iv), (v) and (vi) above.

Accession For	
NTIS GRA&I	<input checked="checked" type="checkbox"/>
DDC TAB	<input type="checkbox"/>
Unannounced	<input type="checkbox"/>
Justification	
By	
Distribution/	
Availability Codes	
Dist	Avail and/or special
A	

QUASI-DYNAMIC MODELS OF SIMPLE EARTHQUAKES AND THE
IMPLICATIONS OF ENERGY FLUX PULSE SHAPES
AS MODELLING CONSTRAINTS¹

John Boatwright

Lamont-Doherty Geological Observatory and

Department of Geological Sciences

of Columbia University

Palisades, New York 10964

ABSTRACT

We have designed a code by which one can compute the far-field body wave displacement and energy flux pulse shapes from a series of "quasi-dynamic" models of rupture. The integration over the (kinematic) slip velocity is calculated on a radial grid using the Fraunhofer approximation. The specification of the slip velocity on the grid is derived from theoretical and finite difference solutions for the mixed boundary value problem of a 3-D frictional rupture model. The analytic form for the slip velocity is naturally divided into two phases: the rupture growth, in which the slip distribution is self-similar and elliptical, and the healing, during which the slip velocity, multiplied by a linearly decreasing factor, goes to zero. The arrival of a P-wave stopping phase, generated by the stopping events which determine the fault perimeter, determines the onset of the healing.

¹ Lamont-Doherty Geological Observatory Contribution Number 0000.

The form of the healing factor, applied to the rupture front, produces a realistic stopping of the rupture, enabling one to model directly a wide range of high-frequency body wave spectra.

These quasi-dynamic models yield radiation efficiencies consistent with the theoretical results of Kostrov (1974), so that the computed energy flux pulse shapes and the time-integrated energy flux may be used as constraints in the modelling of simple ruptures. In particular, the distinct variation of the energy flux pulse shapes provides seismologists with a useful model discriminant, with implications for the determination of both rupture growth and stopping behavior for multiply recorded earthquakes.

We have applied this waveform modelling approach to the analysis of two high stress drop earthquakes which occurred in the Shumagin Islands, Alaska, on May 6, 1974. We analysed both short period WWSSN data and strong motion accelerograph data obtained from an SMAL at Sand Point. The energy flux modelling is shown to provide an estimate of the rupture velocity and thereby establish closer bounds for the estimates of stress release.

INTRODUCTION

The forward problem of modelling seismic sources by matching the waveforms observed at a restricted set of stations is strongly non-unique, as has been shown by a number of authors, notably Anderson and Richards (1976) and Boore and Stierman (1976). These and other papers have established the possibility of fitting the observed waveforms equally well with different source models incorporating a wide range of prescribed slip-functions. Analysis of the inverse problem of seismic source theory (Kostrov, 1975) indicates that this non-uniqueness results from the inherent nature of the seismic observations, in particular the integral nature of the source representation, rather than from inadequate station coverage.

While the appropriate slip function cannot be resolved from seismic observations, the final source models determined using different slip functions can differ substantially, particularly in their estimates of rupture velocity and source dimension. Since both the usual modelling estimates of stress released in tectonic earthquakes (i.e., the dynamic stress drop, τ_e , and the static stress drop, $\Delta\sigma$) depend strongly on these parameters (Boatwright, 1979), the problem of choosing an appropriate slip function is of obvious seismological significance. It is this choice which this paper seeks to restrict in a heuristic fashion, through the use of dynamically consistent rupture models.

In order to determine a suitable source model, or class of source models, it is necessary to consider both a general fracture model and an appropriate set of initial conditions. Our fracture model is

derived from a frictional theory of rupture, i.e., the rupture is modelled as a growing region of stress relaxation, where the stress acting on the (unhealed) rupture area is specified to be the dynamic frictional stress. We presume the initial loading stress to be approximately constant or to decrease away from the rupture origin, and the final rupture area to be simple and planar. These assumptions restrict the application of our rupture model to small and moderate sized earthquakes, as large earthquakes may have strongly complex ruptures (Kanamori and Stewart, 1977).

To complete our model description, we need to assume a fracture criterion and a suitable distribution of fracture strength, which will then determine the motion of the crack tip. For simplicity, however, the rupture velocity is assumed to be constant and subsonic. While this behavior approximately corresponds to a particular fracture criterion (i.e., the strain weakening model of Andrews, 1976), the resulting source model adequately describes ruptures which grow with weakly varying rupture velocities. The rupture velocities determined from the modelling will then represent average rupture velocities.

Our source models are kinematic descriptions of the relative slip velocity which solve, in an approximate fashion, the dynamic problem outlined above. These "quasi-dynamic" models incorporate two basic physical considerations. First, because of the abrupt stress release of the frictional model, the crack tip is the dominant source of radiated energy. The dynamic solution of Kostrov (1964) for rupture growth with a constant rupture velocity gives the self-similar, "elliptical" slip distribution, in which the slip velocity is at a maximum as the

crack tip passes and then slows asymptotically to a constant value. Second, the healing of the rupture starts at the perimeter of the rupture area as a result of the stopping of the crack tip, and the onset of healing propagates into the interior at the compressional wave velocity. The healing is also assumed to be monotonic, i.e., we do not attempt to incorporate breakout phases which result from the interaction of the rupture with a free surface (Burridge and Halliday, 1971), and we presume that in the presence of a finite dynamic frictional stress the rupture will heal without reversal of slip.

These dynamic considerations for our kinematic models naturally divide the slip at any point within the rupture area into two distinct parts, which we will refer to as the rupture growth and the healing. It should be noted that this healing behavior is most directly incorporated into descriptions of the relative slip velocity, rather than the relative dislocation. This is particularly opportune considering the usual far-field source representation, where the pulse shapes are determined from the integral,

$$\Omega_c(\underline{x}, t) = \iint_{\Sigma} \dot{\Delta u}(\underline{\xi}, t - T^c(\underline{x}, \underline{\xi})) d\Sigma, \quad (1)$$

over the fault surface Σ of the relative slip velocity $\dot{\Delta u}(\underline{\xi}, t)$ using the travel time, $T^c(\underline{x}, \underline{\xi})$, between the source point and the receiver, to determine the correct delay.

THE QUASI-DYNAMIC MODEL

Kinematic Description

During the rupture growth, the relative slip velocity at a point ξ from the hypocenter is given by

$$\dot{\Delta u}(\xi, t) = At / (t^2 - |\xi|^2/v^2)^{1/2} \quad t > |\xi|/v \quad (2)$$

where v is the rupture velocity and A is a slip velocity which depends on the dynamic stress drop, τ_e , and the rupture velocity approximately as $A \approx v\tau_e/\mu$ (Dahlen, 1974). Figure 1 shows the resulting slip velocity as a function of time for a representative point on the fault. The continuation of the elliptical slip distribution is shown as a dotted line. Note that for a rupture which grows steadily, the slip velocity at any point of the rupture area does not decrease below the velocity A .

In order both to stop the rupture growth and to approximate the causal healing described in this introduction, we multiply this slip distribution by the function

$$h(\xi, t) = \begin{matrix} 1 & t \leq T_s(\xi) \\ (T_h(\xi) - t)/\bar{h} & T_s(\xi) < t < T_h(\xi) \\ 0 & t \geq T_h(\xi) \end{matrix} \quad (3)$$

where $T_s(\xi)$ is the time of the onset of healing for the point ξ , $T_h(\xi)$ is the healing time (i.e., $\Delta u(\xi, T_h(\xi)) = 0$), and $\bar{h} = T_h(\xi) - T_s(\xi)$ is the healing interval, during which the slip velocity decreases to zero.

For all the models used in this paper, the onset of healing, $T_s(\xi)$, is given by

$$T_s(\xi) = T_0 - \bar{h} - |\xi - x_0|/\alpha \quad (4)$$

where T_0 is the time from the nucleation to the complete healing of the rupture, α is the compressional wave velocity, and x_0 (the position of the last point to heal on the fault plane) is a vector which determines the direction and relative extent of the asymmetry of the final rupture area. The healing function $h(\xi, t)$ thus describes a smoothed (by \bar{h}) circular support function for the rupture which is imploding at the compressional wave velocity. The interaction of this function with the growing rupture produces a source with a finite rupture area which heals into the interior of the fault as desired.

The final rupture area of these models is approximately elliptical, with eccentricity $e < .4$, which may be varied by varying x_0 . In Figure 2, snapshots of the relative slip velocity of a strongly asymmetrical version of the model are shown. The slip velocity has been smoothed so that it may be readily plotted. The regions where the rupture is healing are shown darkened. Note how this rupture is intermediate between a circular rupture and a unilaterally propagating one.

Healing

During the healing interval, the slip velocity at ξ is given by

$$\dot{\Delta u}(\xi, t) = \frac{At(T_h(\xi) - t)}{\bar{h}(t^2 - |\xi|^2/v^2)^{1/2}} \quad T_s(\xi) < t < T_h(\xi). \quad (5)$$

For computational simplicity, the healing interval \bar{h} is assumed to be constant over the rupture. This description of healing does not incorporate any of the complex diffraction effects (i.e., inhomogeneous wave effects) which generally occur as a result of a deceleration of the crack tip (Madariaga, 1977; Achenbach, 1978). However, the causal initiation of healing which propagates into the interior of the rupture area at the compressional wave velocity, is characteristic of both in-plane and circularly symmetric numerical fracture models (Madariaga, 1976).

The assumption that the P-wave stopping phase initiates the healing is a natural result of the frictional model we are using. While the fault is in motion, the shear stress acting across the rupture surface is the dynamic frictional stress. The self-similar solution of Kostrov (1964) implies that motion will continue until information (carried by the P-wave stopping phase) concerning the finiteness of the fault reaches it. The delay between the stopping event and the arrival of the stopping phase produces an overshoot in the distribution of slip on most of the rupture area; that is, at the arrival of the stopping phase, the slip is generally greater than the static slip distribution which would result from a stress drop equal to the dynamic stress drop.

Because the shear stress remains at the dynamic frictional level during healing, the slip cannot reverse direction. After the rupture has healed, the shear stress across the fault surface re-adjusts so that generally the static stress drop is greater than the dynamic stress drop. In healing, the kinetic energy of the fault motions is mostly dissipated in frictional heating, although some is radiated seismically. In stress release models where the dynamic frictional stress is zero, the slip reverses slightly during healing, oscillating around the static offset whose stress drop equals the dynamic stress drop. The kinetic energy of the fault motion is radiated seismically, damping the oscillations (Burridge, personal communication).

In Figure 3, snapshots of the relative dislocation for the same model as Figure 2 are shown with the healing regions again darkened. The rupture area to the left of the healing region is healed. In the topmost graph, the slip is at the final static offset. Note the slight cusp to the right; this is exactly at x_0 and results from the uniform healing behavior for the whole rupture area: in Madariaga's (1976) results, the last point to heal decelerated more rapidly than the rest of the fault.

Stopping Behavior

The constant healing interval for the entire rupture, combined with the constant rupture velocity, produces a perimeter region of width

$$\Delta x = \bar{h} \frac{av}{v+a} \quad (6)$$

across which the particle velocity at the crack tip decreases continuously to zero as described by eq. (5), but where the beginning of the interval is given by $|\xi|/v$ rather than $T_h(\xi)$. This interaction produces a reasonable approximation of a rupture which stops gradually. Since \bar{h} is a free parameter, this allows us to model ruptures which stop in an arbitrarily gradual or sudden fashion by varying $\Delta\xi$, thereby obtaining body wave spectra which show spectral falloffs $\omega^{-\gamma}$ with $2 < \gamma < 3$ and the general two corner frequency envelopes of the type discussed by Boatwright (1978b). The possibility of modelling this range of stopping behaviors represents a significant advance in source modelling. As a motivation for this kinematic stopping behavior, note that for this region the function $h(\xi, t)$ can be written as

$$\frac{(T_h(\xi) - t)}{\bar{h}} = \frac{(T_h(\xi) - |\xi|/v)}{\bar{h}} \frac{(T_h(\xi) - t)}{(T_h(\xi) - |\xi|/v)}, \quad (7)$$

where we may identify the first term as an appropriate decrease of A resulting from a decrease in the dynamic stress drop. The second term, $(T_h(\xi) - t)/(T_h(\xi) - |\xi|/v)$, contains the time dependence of the healing we have used for the interior rupture area.

As shown in the series of snapshots in Figure 4, detailing the change of the slip velocity on this fault perimeter, the interaction of the rupture growth and healing produces a realistically gradual stopping at the fault boundary. As a result, the slip distributions of these models are generally more smooth than those of constant stress drop models. This smoothness is evident in Figure 3, where the dislocation at the healed edge of the rupture decreases gradually to zero.

Using the technique of Andrews (1974), we have calculated the static stress drop for one of these models. The results are displayed in Figure 5. The effect of the smoothed dislocation is to smooth the stress drop, weakening the stress concentration at the perimeter of the fault. The peaked behavior of the stress drop at x_0 is a result of our healing specification, as mentioned above. A variation of \bar{h} over the interior of the fault could be determined such that the static stress drop was smooth at x_0 but this would have little effect on the radiated pulse shapes.

ENERGY FLUX PULSE SHAPES

A significant feature of the "quasi-dynamic" source models is that the seismic energy radiated is consistent with the theoretical results of Kostrov (1974) and Madariaga (1976) for general frictional models of rupture, as described in the Introduction. This agreement allows us to use both the energy flux pulse shapes and the time integrated energy flux (the radiated energy per unit area) of the body wave arrivals as modelling constraints. The energy flux across a surface at \underline{x} , in a body wave travelling with velocity $c(\underline{x})$, normally incident to the surface, is given by

$$\dot{\epsilon}(\underline{x}, t) = \rho(\underline{x})c(\underline{x})\dot{u}^2(\underline{x}, t) \quad (8)$$

where $\rho(\underline{x})$ is the density and $u(\underline{x}, t)$ is the ground displacement (Bullen, 1965, p. 127]. Thus, if the phase distortion of the free surface is corrected for, the time history of the square of the ground velocity

represents the energy flux of the body wave arrival. These v^2 -plots were first used by Hanks (1974) in an analysis of the Pacoima Dam recording, and more recently, by Boatwright (1978a) in an analysis of a multiply recorded aftershock of the 1975 Oroville, California earthquake. Because of their non-linear signal enhancement, v^2 -plots provide generally coherent, noise-free pulse shapes, suppressing echoes and low frequency contamination.

The v^2 -plots can provide seismologists with particularly useful waveform constraints. In discussing v^2 pulse shapes, we consider only the undistorted (elastic whole-space) pulse shapes. As squaring the ground velocity is a non-linear operation, any phase distortion must be corrected in the ground velocity before squaring. The (undistorted) far-field velocity pulse shapes from simple sources are made up of one positive and one negative pulse with equal areas; therefore the resulting v^2 -plots show two distinct pulses separated by an actual zero. We will refer to the first pulse as the rupture phase, as it details the growth of the rupture and refer to the second pulse as the healing phase.

There are three distinct pulse measurements which may be obtained from v^2 -plots. The first of these measurements, the width of the rupture phase, provides an estimate of the pulse rise time (or the first half-cycle of the velocity trace, $\tau_{1/2}$) and has been discussed in detail by Boatwright (1979). This rise time, affected by directivity, can readily be used to estimate the duration of the rupture growth in the direction of the station at which the pulse was observed. A second measurement, the separation of the healing- and rupture-phase peaks, provides a pulse duration estimate giving information about the geometry

of the rupture if the azimuthal distribution of the observed pulse shapes is adequate. Finally, the relative amplitude of the two phases establishes a useful constraint on the fault motions. In general, this relative energy content varies substantially over the focal sphere. This is a direct result of the difference in the particle velocity behavior behind the crack tip and during healing. The enhanced constructive interference of the rupture phase for body waves with phase velocities on the fault surface which approach the rupture velocity dominates the v^2 -plots of shear wave pulse shapes radiated along the fault. In directions near the normal to the fault plane the healing phase increases in amplitude and in these directions the relative amplitude of the phases is very sensitive to the rupture velocity and the rupture geometry. For the two events discussed in the second part of this paper, this particular feature of the waveform, combined with an approximate description of the rupture geometry, is used to estimate the rupture velocity and is therefore a crucial aspect of the analysis.

MODELLING OF TWO SHUMAGIN ISLANDS EARTHQUAKES

On April 6, 1974, two moderate size ($m_b = 5.8, 6.0$) earthquakes occurred within a local network of short period seismograph stations (run by Lamont-Doherty Geological Observatory) in the Shumagin Islands, Alaska. They were followed by 69 recorded aftershocks over the next two weeks. Both main shocks triggered a strong motion accelerograph (SMAL) at Sand Point, 50 km NNW of their epicenters. In Figure 6, we show a map view of the epicentral area.

A thorough analysis of the sequence is presently in preparation (House and Boatwright) which includes a full discussion of the after-shock locations, the sequence b -value, the fault plane solution, the far-field waveform analysis and the source modelling. We have included only the far-field waveform analysis and the source modelling in this paper, as an example of the application of the quasi-dynamic sources for energy flux modelling.

SMA1 Waveform Analysis

The SMA1 records from the 0153 and 0356 events were photographically enlarged, digitized and instrument corrected using the technique discussed by Boatwright (1978b). Since the Sand Point station was at an SH node, the vertical and horizontal components were combined to obtain the incident SV pulse shape, using the free surface transformation,

$$u_{SV}(t) = \frac{\cos 2j}{2\cos j} u_x(t) + \sin j u_z(t). \quad (9)$$

Here j ($= 33^\circ$) is the angle of incidence of the S-wave, $u_x(t)$ is the horizontal component (positive away from the source) and $u_z(t)$ is the vertical component (positive downward). This (real) transformation was derived from Chapter 5, problem 5.6, of Aki and Richards (1970). Because the transformation is essentially a rotation into the particle motion of the incident SV wave, it suppresses the evanescent SP arrival expected at this range (Anderson, 1976) by a factor of 8.

The resulting SV acceleration traces for both events are shown in Figures 7 and 8, along with their respective velocity and v^2 traces. The integration to velocity was performed using a parabolic baseline technique detailed in Perez et al. (1979). Both accelerograms show a significant 12 Hz site response which is substantially reduced in the integration to velocity.

The v^2 -plots of the SV phases at Sand Point are remarkably similar in shape and amplitude, although the 0153 pulse shape is noticeably more impulsive. This similarity indicates that the events probably share nearly the same rupture geometry, as they have the same focal mechanism. The large relative amplitude of the healing phase suggests either that the rupture propagated towards the Sand Point station (downdip) or that the rupture velocity was slow, about .6 of the shear wave velocity, if the rupture was approximately circular. These two possibilities are considered in the discussion of the WWSSN short period data. The final model v^2 -plots are shown along with the data as dashed lines.

In Figures 9 and 10, we show the displacement spectra for the two events, as well as the final model spectra (dashed lines). The data has been corrected for attenuation assuming a shear wave Q of 300. The site amplification at 10-15 Hz shows up very strongly in these spectra. The corner frequencies, marked by dots, were estimated assuming this amplification to be spurious. The corrected velocity spectra were integrated to obtain the integral of the squared ground velocity, which we will call I_{SV} .

In order to estimate the source dimension, we have used three different measurements of the SMA1 pulse shapes and spectra; i.e., the

corner frequency, the characteristic frequency and the pulse rise time. The necessary spectral and pulse parameters are listed in Table 1. Following Boatwright (1979), the characteristic frequency, η_B , is defined as

$$\eta_B = \left(\frac{I_{sv}}{\bar{u}_{sv}^2} \right)^{1/3} \quad (10)$$

where \bar{u}_{sv} is the low frequency asymptote. This spectral measurement provides an estimate of the source dimension (radius = a) through the relation,

$$\kappa_B = \frac{a}{v} \eta_B \quad (11)$$

where v is the rupture velocity and $\kappa_B = 1.9$ for this takeoff angle. The pulse rise time, $\tau_{1/2}$, defined here to be the measurable width of the first pulse of the v^2 -plot (the rupture phase), may also be used to estimate the source dimension, from the empirical relation (Boatwright, 1979),

$$\tau_{1/2} = \frac{(13-12\zeta)}{16} \frac{a}{v} \quad (12)$$

Here, $\zeta = \frac{v}{c} \sin \theta$ is the ratio of the rupture velocity to be the phase velocity of the ray along the fault surface. The results from these three source dimension estimates are shown in Table 2. If we assume the ratio

of the rupture velocity to the shear wave velocity to be bounded as $.55 < \frac{v}{\beta} < .8$, then we obtain the first order estimates of $1.0 < a < 1.4$ km for the 0153 event and $1.4 < a < 2.0$ km for the 0356 event.

WWSSN Waveform Analysis

Before fitting for a particular rupture model, it is necessary to investigate the rupture geometry of the 0356 event. We have analysed 9 short-period P-wave arrivals from 6 WWSSN stations. The steps of this analysis are shown in Figure 11, using the P-wave recorded at GDH as an example. The lowest trace is the seismogram as digitized, and the trace above it, the seismogram after filtering with a zero-phase band-pass filter. This filter is made up from a triangle smoothing operator and a second order Butterworth high pass filter (corner at .3 Hz) run forwards and backwards on the trace. The third trace is the ground velocity, obtained by a recursive deconvolution scheme derived from a bilinear approximation (Kanasewich, 1975, p. 194) to the coupled galvanometer-seismometer response. The uppermost trace is the square of the ground velocity. It is the variation of these v^2 -plots which we will use to determine the rupture geometry of the event.

In Figure 12, we show how the pulse shapes vary over the focal sphere. The P, pP, and sP takeoff directions are plotted relative to the fault plane obtained by House and Boatwright, so that the fault plane is the horizontal plane of the stereonet. To account for the pulse shape differences between the P and S body waves, the phase leaving as P-waves have been corrected to the appropriate takeoff direction

(open circles) for S-waves having the same phase velocity along the fault surface, which requires the far-field pulse shapes to be identical. From Kostrov (1970), this corrected takeoff angle is

$$\theta_s = \sin^{-1} \left(\frac{\beta}{\alpha} \sin \theta_p \right) \quad (13)$$

where θ_β and θ_α are measured from the normal to the fault plane. Note that almost all the corrected takeoff angles lie between 20° and 30°. The line across the stereonet marks the strike of the Benioff zone.

In order to evaluate the variation of these v^2 -plots, in Figure 13 we show the synthetic variation of the v^2 -plots over our model range. For these synthetics, we have used both circular and slightly asymmetrical versions of the quasi-dynamic models, fixing the ratio $\frac{a}{v}$.

In the left-hand column of Figure 13, we show the variation of the v^2 pulse shape for different rupture velocities where the takeoff angle of the ray is at 30° from the normal to the fault plane. These same synthetics may also be used to describe the variation of the v^2 pulse shapes for different takeoff angles. For a circular rupture with velocity $v = .6\beta$, the upper and lower figures approximate the v^2 pulse shapes at 35° and 25°, respectively, from the fault normal. The contrasting interpretations of these synthetics results from the approximate similarity of pulse shapes having similar values of $\frac{v}{c} \sin \theta$, for similar rupture models (Boatwright, 1979).

In the right-hand column, we detail the pulse shape variations for different directions of asymmetrical rupture growth relative to the observer. In these synthetics, the takeoff angle is 30° from the fault

normal and the rupture velocity is $v = .6\beta$. The asymmetrical models have about an 10% unilateral rupture. If $\xi_f(\phi)$ is the distance from the hypocenter to the perimeter of the fault of the ϕ direction, the percent unilateral rupture is given as

$$100 \cdot \max_{\phi} \frac{\xi_f(\phi) - \xi_f(\phi + \pi)}{\xi_f(\phi) + \xi_f(\phi + \pi)} \quad (14)$$

For an elliptical fault whose hypocenter is at one of the foci, the percent unilateral rupture is simply $100 \cdot e$, where e is the eccentricity.

In Figure 13, much of the more striking variations of the v^2 -plots appears to result from differences in the crustal structure beneath the stations used. The Sand Point v^2 pulse shape has been plotted with the same time scale, in order to show the relative attenuation present in the short period WWSSN data. In particular, it is necessary to point out the broadening (perhaps due to attenuation) of the HKC pulse shapes, with respect to the pulse shapes at nearly the same takeoff direction. Also the pulses at GDH and AAM appear to have a crustal reverberation which is interfering destructively with the healing phase of the v^2 pulse shape. This interference may be seen in the plot of the WWSSN analysis in Figure 11 as well.

The slight difference (in relative amplitude and timing) of the depth phase (updip) pulse shapes relative to the downdip pulse shapes suggests that the rupture had a slight downdip component of unilateral rupture (about 5%) and a rupture velocity of about $v = .6\beta$. Because

of the narrow band of the short period WWSSN instruments and the unknown crustal structure beneath the stations whose P-waves were analysed, we can use these results only qualitatively. However, it is important to note that nearly all of the v^2 -plots fall within the model range spanned by Figure 13, from which we have determined the variance of our source parameter estimates. As we have already estimated the ratio $\frac{a}{v}$ for these events, specifying an approximate rupture velocity and rupture geometry thus determines our final models.

Final Source Models

For the final source modelling we have used synthetics generated by two circular versions of the quasi-dynamic models. Since the displacement spectra from these events falloff faster than ω^{-2} , we presume that the rupture stopped gradually rather than abruptly (Madariaga, 1978), and this gradual stopping is incorporated into the models.

Since both events were fit with circular models, the rupture velocities of the two models are slightly different: $v = .68$ for the 0153 event and $v = .558$ for the 0356 event; similar results would have been obtained if we had fixed the rupture velocity and used asymmetrical rupture geometries. Using a slightly asymmetrical model and a rupture velocity of $.68$ for the 0356 event, lowers the stress estimates by $\approx 20\%$.

The source parameters obtained from our model fits are listed in Table 3. We have calculated the moment and radiated seismic energy using the formulae,

$$M_0 = 4\pi \rho(\xi_0)^{1/2} \beta(\xi_0)^{5/2} \rho(x)^{1/2} \beta(x)^{1/2} \frac{R(x, \xi_0)}{F^{SV}(\theta, \phi)} \cdot \bar{u}_{sv} \quad (15)$$

$$E_s = \frac{\rho(x)\beta(x)}{e_\beta(\theta)} \left(\frac{R(x, \xi_0)}{F^{SV}(\theta, \phi)} \right)^2 I_{sv} \quad (16)$$

where $\rho(\xi_0)$, $\rho(x) = 3.4, 2.5$ gm/cm³ and $\beta(\xi_0)$, $\beta(x) = 4.4, 2.5$ km/sec are the densities and shear wave velocities at the source and receiver, respectively, $R(x, \xi_0) = 52$ km is the geometrical spreading factor, calculated following Newman (1973) and $F^{SV}(\theta, \phi) = .46$ is the radiation pattern coefficient. $e_\beta(30^\circ) = .2$ is the fractional energy flux, which relates the time integrated energy flux at a particular takeoff angle to the total radiated seismic energy (Boatwright, 1979).

The dynamic stress drop also may be calculated directly from this modelling. Since the quasi-dynamic models incorporate the self-similar slip distribution described by Kostrov (1964), Burridge and Willis (1969) and others, the slip distribution is scaled by the initial relative slip velocity, A . Thus, any model fit may also be used to determine the dynamic stress drop, via the formula (Boatwright, 1979),

$$\tau_e = \frac{4\pi}{av^2} \rho(\xi_0)^{1/2} \beta(\xi_0)^{5/2} \rho(x)^{1/2} \beta(x)^{1/2} \frac{R(\xi_0, x)}{F^C(\theta, \phi)} \left\langle \frac{\dot{u}(x, t)}{\dot{\Omega}(x, t)} \right\rangle, \quad (17)$$

where $\left\langle \frac{\dot{u}(x, t)}{\dot{\Omega}(x, t)} \right\rangle$ is obtained by scaling the data, $\dot{u}(x, t)$ to the

synthetics, $\dot{\Omega}(x,t)$. The model fits give $\left\langle \frac{\dot{u}(x,t)}{\dot{\Omega}(x,t)} \right\rangle = .38$ cm/sec and .34 cm/sec for the 0153 and 0356 events, respectively.

The results compiled in Table 3 show two systematic anomalies. For both events, the dynamic stress drop is greater than the average static stress drop, while the apparent stress is substantially lower than $\tau_e/4$, which is the expected value for frictional ruptures with $v = .68$ (Madariaga, 1976). However, the gradual stopping of these events may explain both anomalies. If the rupture nucleated in a localized region of high stress, and grew beyond this region, the average stress drop over the rupture area would be lower than the initial stress drop, while the radiated energy would be low due to the gradual stopping in the less loaded region. Note also the consistent differences in the stress estimates for the two events, that the larger 0356 event has a stress drop = 70% of the 0153 event.

CONCLUSIONS

The first goal of this modelling effort is the determination of the rupture velocity of these two events. The estimate of rupture velocity is critical both for the modelling, because of the trade-off in the directivity between rupture velocity and rupture geometry, and for the estimates of stress release ($\Delta\sigma$ and τ_e), because they depend strongly on the estimate (or a priori assumption) of the rupture velocity.

To illustrate the second point, note that if the rupture velocities were estimated to be .98, then both the static and dynamic stress drop estimates would be approximately 30% of the values listed in Table 3.

This non-linear dependence obviously requires a strong estimate of the rupture velocity in order to obtain reliable estimates of stress release.

In Figure 14, we have plotted the locations of 29 aftershocks of the two events, projected onto the fault plane. Note the fit of the estimated rupture perimeter of the 0153 event to its aftershock cluster. The aftershock cluster of the 0356 event is more diffuse, perhaps because of its lower stress drop. While these aftershock locations cannot be used to confirm our estimates of the source dimension (owing to their relative uncertainty and the small dimensions of the earthquakes), they indicate that the two events represent spatially distinct ruptures (see also Figure 6). This interpretation is reinforced by the systematic differences in stress released by the two events. Because of the similarity of the fault plane solutions and the SMAL waveforms, the uncertainty of the ratio of any estimate of stress release is approximately 10%, and therefore these differences are significant.

These arguments lead naturally to the conclusion that the two main shocks represent the failure of two distinct asperities, or stress concentrations. Thus, the extremely high stress drops are not directly indicative of a similarly high average stress over the region although these events may be presumed to load the unruptured part of the fault plane. The stress concentrations are inferred to be the result of patches of high strength which have not yielded with the rest of the fault plane. Andrews (1975) has called these stress concentrations anti-dislocations, as they represent distributions of negative slip relative to the rest of the fault system. The gradual stopping character of both events (inferred from the ω^{-3} falloff of their displacement

spectra and incorporated into the final source models) also supports this interpretation, as this stopping behavior is to be expected of a rupture which grows beyond the localized stress concentration where it nucleated. This is equivalent to the "seismic gap" stopping mechanism discussed by Hussein et al. (1976). Using their formula for fracture energy,

$$\gamma_0 = \frac{a\tau_e^2}{2\pi\mu} \quad (18)$$

where a is the fault radius, we obtain $\gamma \approx 3 \times 10^{10}$ ergs/cm² for the two events. This extremely high fracture energy implies that the fault zone for these events had a similarly high fracture strength, and further corroborates the asperity interpretation.

ACKNOWLEDGEMENTS

I am indebted to my brother Bill for his help in the original specification of the model, and to both B. V. Kostrov and Raul Madariaga, with whom I have enjoyed brief but illuminating discussions. Helpful criticism from Paul Richards enabled me to improve the paper enormously. This paper was reviewed by Larry Burdick and Chris Scholz. The research was supported by the Advanced Research Projects Agency of the Department of Defense and was monitored by the Air Force Office of Scientific Research under Contract Number F49620-77-C-0098.

REFERENCES

- Achenbach, J.D., Ray method for elastodynamic radiation from a slip zone of arbitrary shape, J. Geophys. Res., 83, 2283-2302, 1978.
- Anderson, J.G., Motions near a shallow rupturing fault: evaluation of effects due to the free surface, Geophys. J. R. astr. Soc., 46, 575-593, 1977.
- Anderson, J.G., and P.G. Richards, Comparison of strong ground motion from several dislocation models, Geophys. J. R. astr. Soc., 42, 347-373, 1975.
- Andrews, D.J., Evaluation of static stress on a fault plane from a Green's function, Bull. Seism. Soc. Am., 64, 1629-1633, 1974.
- Andrews, D.J., From antimoment to moment: plane-strain models of earthquakes that stop, Bull. Seism. Soc. Am., 65, 163-182, 1975.
- Andrews, D.J., Rupture propagation with finite stress in antiplane shear, J. Geophys. Res., 81, 3575-3582, 1976.
- Aki, K., and P.G. Richards, Quantitative Seismology: Theory and Methods, accepted for publication by W.H. Freeman and Company, San Francisco, to appear 1980.
- Boatwright, J., Radiated seismic energy and the implications of energy flux measurements for strong motion seismology, Proc. Sem.-Workshop on Strong Ground Motion, 1978a, in preparation.
- Boatwright, J., Detailed spectral analysis of two small New York State earthquakes, Bull. Seism. Soc. Am., 68, 1117-1131, 1978b.
- Boatwright, J., A spectral theory for circular seismic sources; simple estimates of source dimension, effective stress and radiated seismic energy, submitted to Bull. Seism. Soc. Am., 1979.

- Boore, D.M., and D.J. Stierman, Source parameters of the Pt. Mugu, California earthquake of February 21, 1973, Bull. Seism. Soc. Am., 66, 385-404, 1976.
- Burridge, R., Admissible speeds for plane-strain self-similar shear cracks with friction but lacking cohesion, Geophys. J. R. astr. Soc., 35, 439-455, 1973.
- Burridge, R., and G.S. Halliday, Dynamic shear cracks with friction as models for shallow focus earthquakes, Geophys. J. R. astr. Soc., 25, 261-283, 1971.
- Burridge, R., and J.R. Willis, The self-similar problem of the expanding elliptical crack in an anisotropic solid, Proc. Camb. Phil. Soc., 66, 443-468, 1969.
- Dahlen, F.A., On the ratio of P-wave to S-wave corner frequencies for shallow earthquake sources, Bull. Seism. Soc. Am., 64, 1159-1180, 1974.
- Husseini, M.I., and M.J. Randall, Rupture velocity and radiation efficiency, Bull. Seism. Soc. Am., 66, 1173-1187, 1976.
- Husseini, M.I., D.B. Jovanovich, M.J. Randall, and L.B. Freund, The fracture energy of earthquakes, Geophys. J., 43, 367-386, 1975.
- Kanamori, H., and G.S. Stewart, Seismological aspects of the Guatemala earthquake, J. Geophys. Res., 83, 3427-3434, 1978.
- Kanasewich, E.R., Time Sequence Analysis in Geophysics, University of Alberta Press, Edmonton, Alberta, 1975.
- Kostrov, B.V., Selfsimilar problems of propagation of shear cracks, PMM, vol. 28, no. 5, 889-898, 1964.
- Kostrov, B.V., The theory of the focus for tectonic earthquakes, Izv. Earth Physics, no. 4, 84-101, 1970 [translated by D.G. Fry].

Kostrov, B.V., Seismic moment and energy of earthquakes, and seismic flow of rock, Izv. Fizika Zemli, 1, 23-40, 1974.

Kostrov, B.V., The Mechanics of the Focus of Tectonic Earthquakes, Nauka, Moscow, 1975.

Madariaga, R., Dynamics of an expanding circular fault, Bull. Seism. Soc. Am., 66, 639-666, 1976.

Madariaga, R., High frequency radiation from crack (stress drop) models of earthquake faulting, Geophys. J., 51, 625-652, 1977.

Newman, P., Divergence effects in a layered earth, Geophysics, 38, 481-488, 1973.

Perez, O., R. Husid, and A. Espinosa, Spectral analysis of accelerograms recorded during Nicaraguan earthquakes, submitted to Bull. Seism. Soc. Am., 1979.

Richards, P.G., The dynamic field of a growing plane elliptical shear crack, Int. J. Solids Structures, 9, 843-861, 1973.

TABLE 1 — Spectral Parameters

	0153	0356
\bar{u}_{SV}	$.13 \pm .04 \text{ cm/sec}$	$.25 \pm .07 \text{ cm/sec}$
I_{SV}	$2.2 \pm .6 \text{ cm}^2/\text{sec}$	$3.1 \pm .8 \text{ cm}^2/\text{sec}$
ν_{β}	1.2 Hz	.8 Hz
η_{β}	5.1 Hz	3.5 Hz
$\tau_{1/2}$.24 sec	.37 sec

TABLE 2 — Rupture Duration $\left(= \frac{a}{v} \right)$

Method	0153	0356
corner frequency	.41 ± .1 sec	.62 ± .2 sec
characteristic frequency	.37 ± .1 sec	.53 ± .15 sec
rise time	.39 ± .08 sec	.60 ± .1 sec
average	.39 ± .05 sec	.59 ± .1 sec

TABLE 3 — Source Parameters

0153 eventradius - $a = 1.2$ kmmoment - $M_0 = 3.5 \pm .8 \times 10^{24}$ dyne-cmstatic stress drop - $\Delta\sigma = 890$ bars range 600-1100 barsdynamic stress drop - $\tau_e = 1040 \pm 350$ barsradiated energy - $E_s = 8.7 \pm 3.0 \times 10^{20}$ dyne-cmapparent stress - $\tau_a = 160 \pm 60$ bars0356 eventradius - $a = 1.65$ kmmoment - $M_0 = 6.7 \pm 1.5 \times 10^{24}$ dyne-cmstatic stress drop - $\Delta\sigma = 650$ bars range 350-800 barsdynamic stress drop - $\tau_e = 780 \pm 250$ barsradiated energy - $E_s = 12.4 \pm 4.0 \times 10^{20}$ dyne-cmapparent stress - $\tau_a = 120 \pm 50$ bars

FIGURE CAPTIONS

- Figure 1: Generalized plot of the quasi-dynamic slip velocity. T_r is the rupture arrival time, T_s the arrival time of the first stopping phase and T_h the time of healing. The slip velocity scales with the velocity A , which depends on the rupture velocity and dynamic stress drop approximately as $A \approx v \frac{\tau_e}{\mu}$.
- Figure 2: Snapshots of the slip velocity distribution of a quasi-dynamic model, with time increasing from the bottom. The slip is healing in the darkened regions. The slip velocity has been smoothed (by dx) so that it may be easily plotted. Note how the character of the rupture changes from a circular rupture to a unilateral propagation.
- Figure 3: Snapshots of the slip distribution of the model shown in Figure 2. The slip has healed to the left of the darkened regions. In the top figure, the static slip distribution is shown; note the smoothed slip at the rupture perimeter, and the cusp at x_0 .

Figure 4: Snapshots of the slip velocity distribution at one edge of the model, detailing the stopping behavior. The healing regions have not been darkened. The stopping phase can be seen as a discontinuity in slope at times $t = .16$ and $t = .18$. By $t = .22$ the perimeter has healed completely.

Figure 5: Distribution of static stress drop and final slip for one of the models. Note how the smoothed distribution of slip naturally weakens the stress concentration at the perimeter of the rupture. The sharp stress node is an unphysical artifact of the healing description.

Figure 6: Map of the Aleutian arc near the Shumagin Islands, showing the epicentral area of the events to be discussed and the stations used to locate the events and their aftershocks. The inset shows the epicenters of the two events along with the 29 located aftershocks. Note the clear grouping of the aftershocks into two distinct clusters.

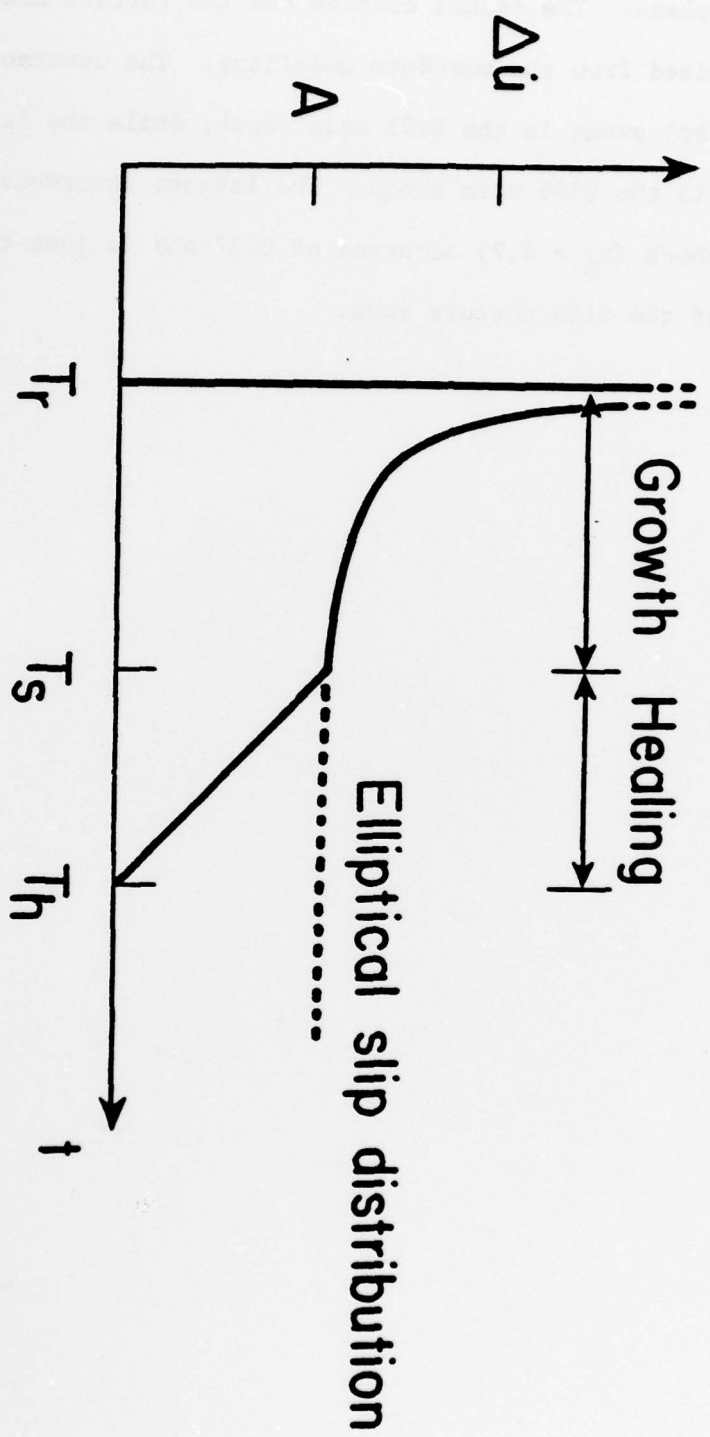
Figure 7: SV acceleration, velocity and v^2 pulse shapes for the 0153 event. The dashed line in the v^2 -plot is the synthetic pulse shape from the final model.

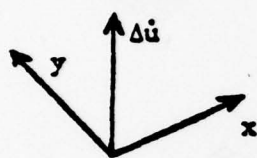
Figure 8: SV acceleration, velocity and v^2 pulse shape for the 0356 event. The dashed line in the v^2 -plot is the synthetic pulse shape from the final model.

- Figure 9: Displacement amplitude spectrum for the 0153 event. The dot marks the measured corner frequency. The spectrum has been corrected for attenuation. The spectral amplification at 10-15 Hz is a site response. The dashed line is the synthetic spectrum.
- Figure 10: Displacement amplitude spectrum for the 0356 event. See explanation for Figure 9.
- Figure 11: Detail of short-period WWSSN analysis. The lowermost trace is the seismogram as digitized with the bandpassed seismogram above it. The next traces are the deconvolved velocity and finally the v^2 -plot.
- Figure 12: Variation of the short-period WWSSN v^2 pulse shapes from the 0356 event over the focal sphere. The takeoff angles of the phases have been rotated so that the fault plane is the plane of the stereonet. The phases which took off as P-waves are corrected (solid lines) to the equivalent takeoff angles for S-waves. The two arcs are at 20° and 30° from the fault normal. The Sand Point SMA1 v^2 -plot is plotted at the same time scale for reference.
- Figure 13: The variation of the v^2 pulse shapes over the model range. The left-hand column shows the variation of the pulse shapes with the variation of rupture velocity or takeoff angle (see text), while the right-hand column shows the variation resulting from a slightly asymmetrical rupture geometry.

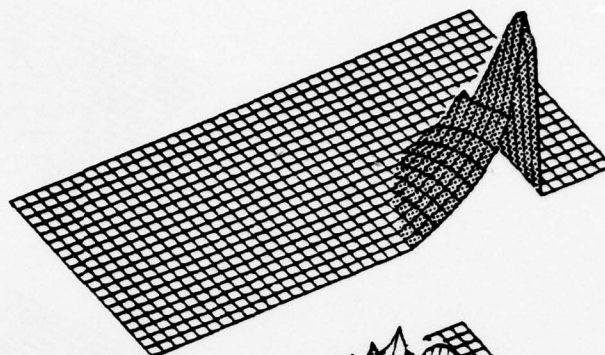
Figure 14: Plot of the aftershock locations projected onto the fault plane. The dashed circles are the rupture areas determined from the waveform modelling. The uppermost (smaller) event is the 0153 main shock, while the larger event is the 0356 main shock. The largest intervening aftershock ($m_b = 4.7$) occurred at 0227 and is just to the left of the 0153 rupture zone.

QUASI-DYNAMIC SLIP VELOCITY

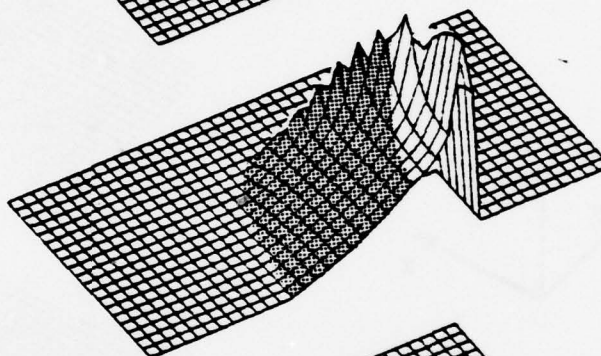




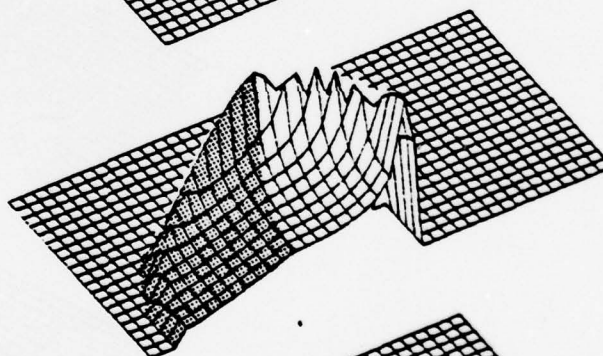
$t = .4$



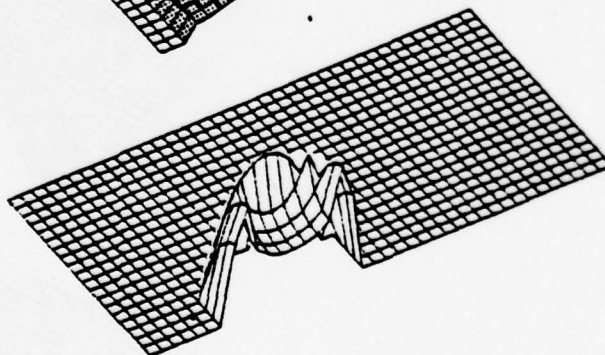
$t = .3$

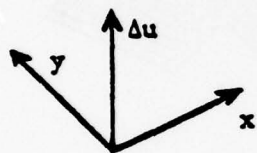


$t = .2$

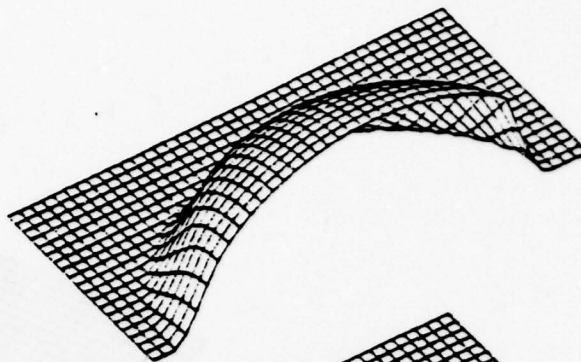


$t = .1$

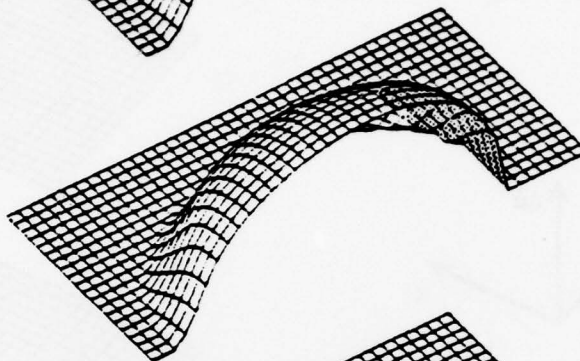




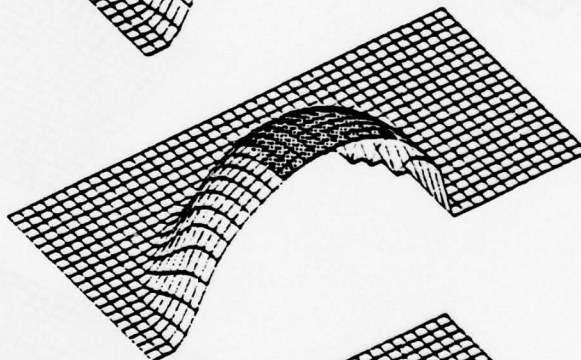
$t = .5$



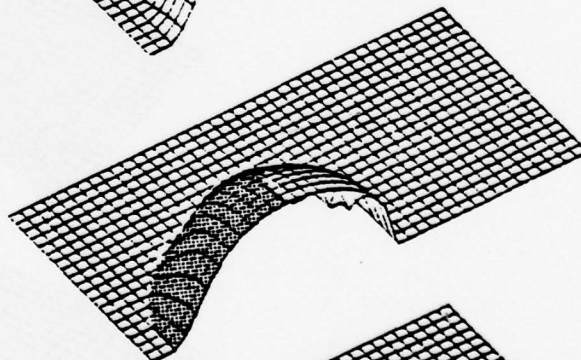
$t = .4$



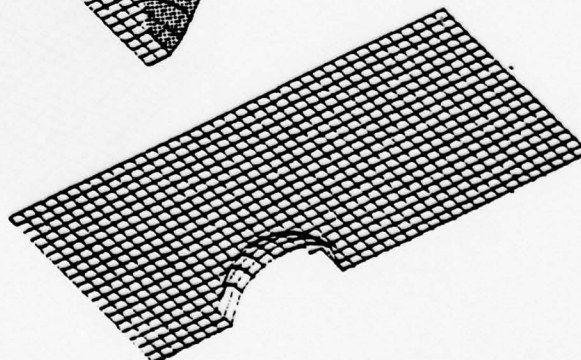
$t = .3$



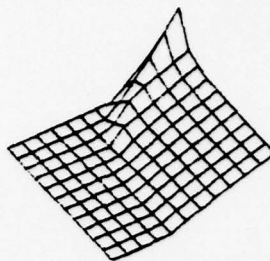
$t = .2$



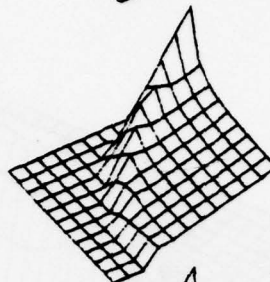
$t = .1$



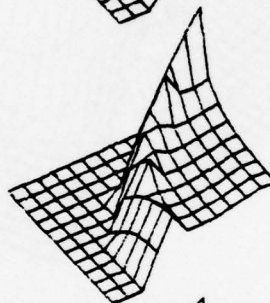
$t = .22$



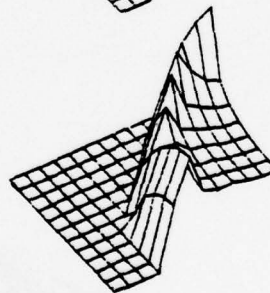
$t = .20$



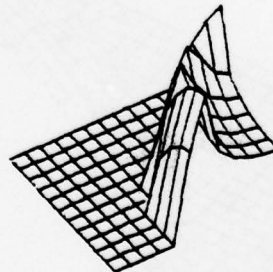
$t = .18$



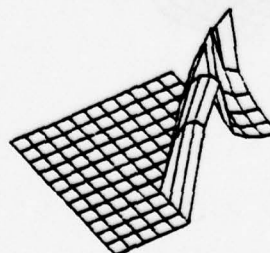
$t = .16$

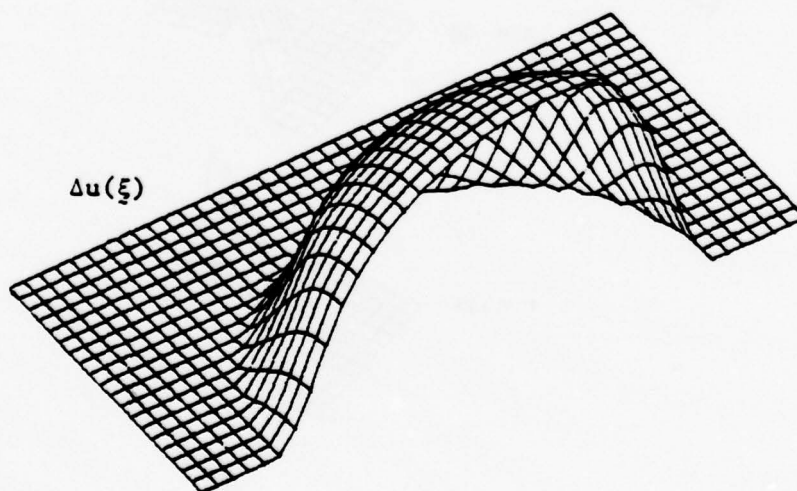
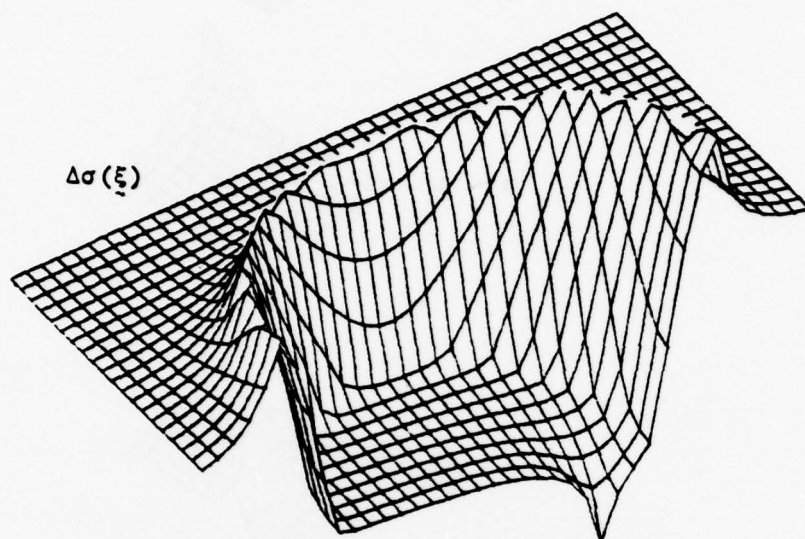


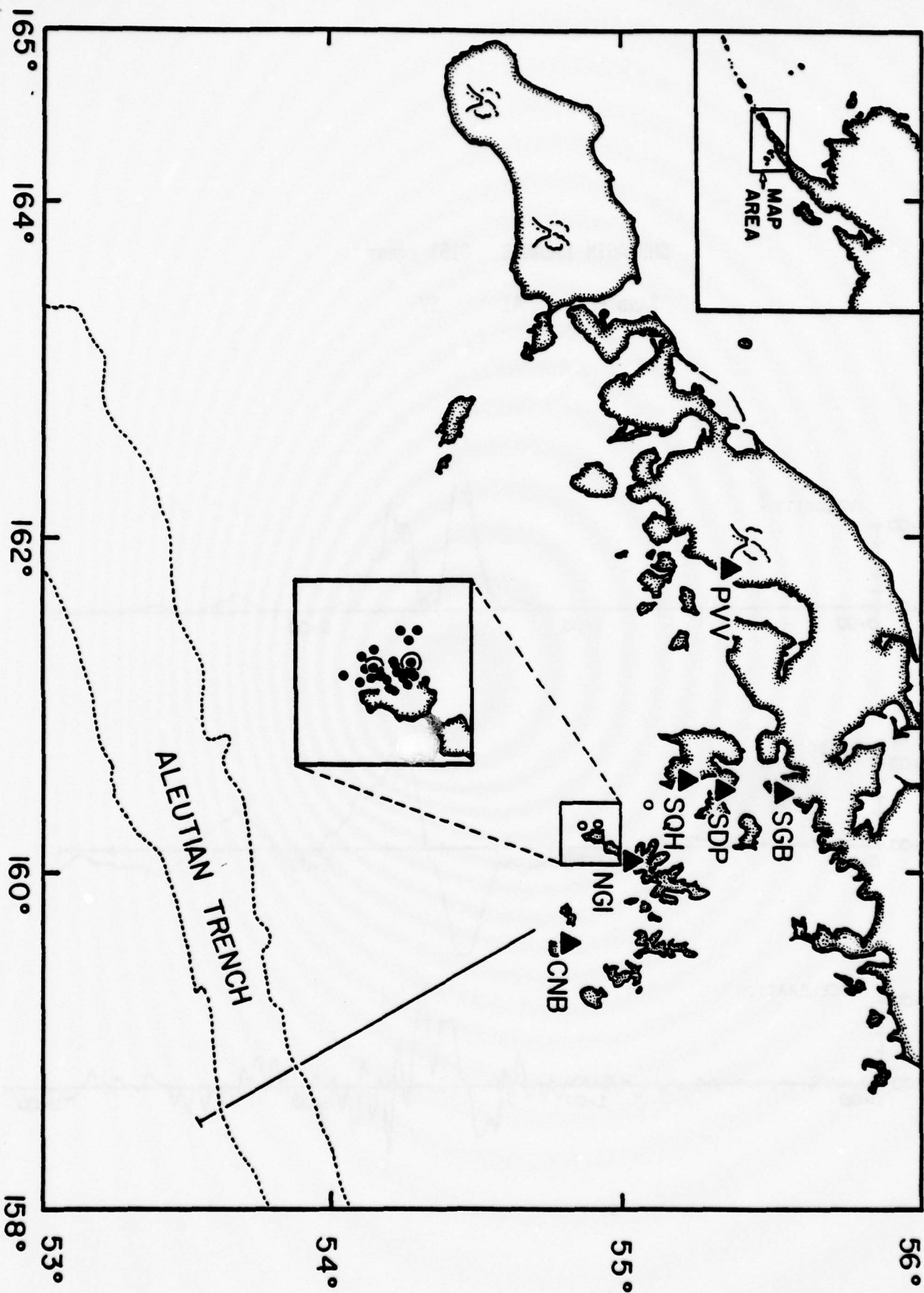
$t = .14$



$t = .12$

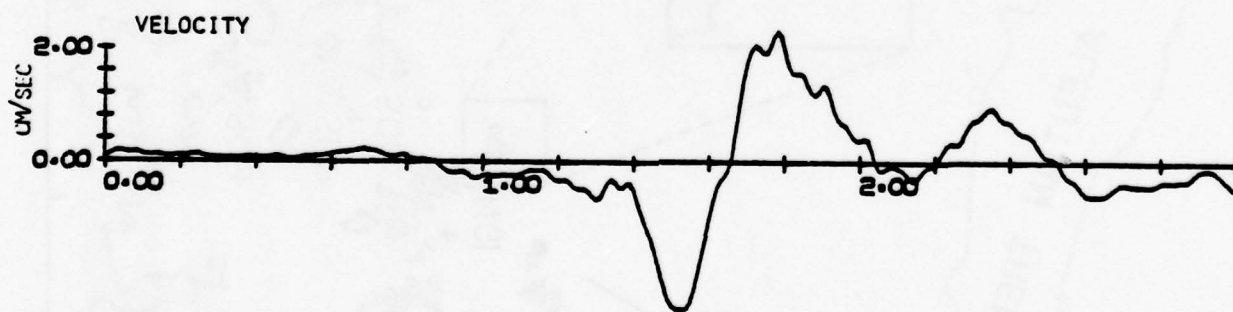
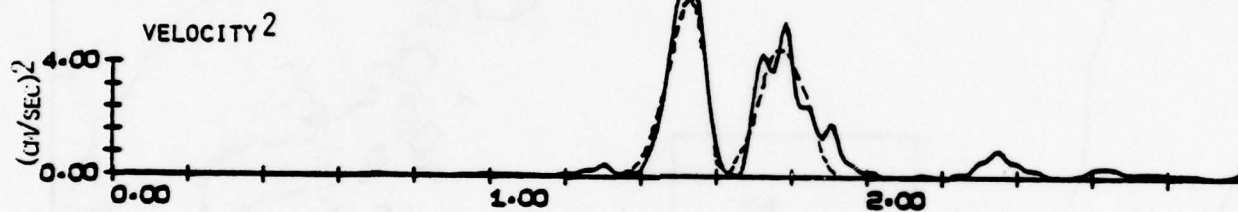






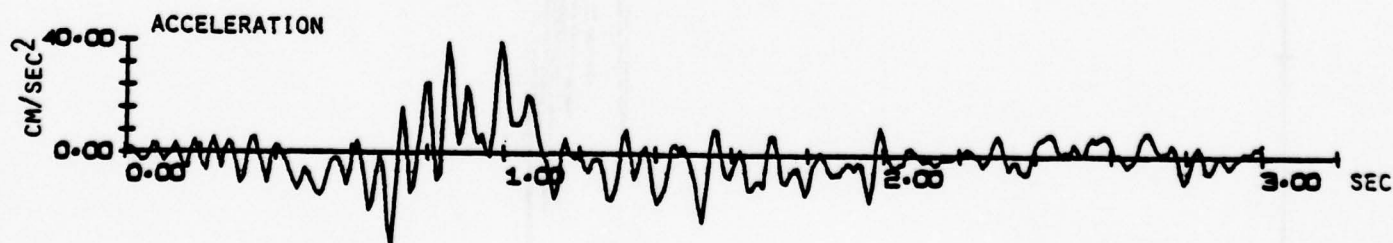
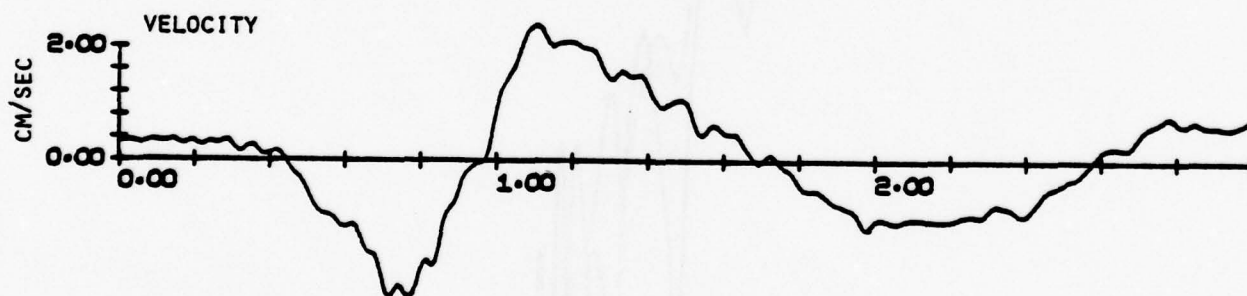
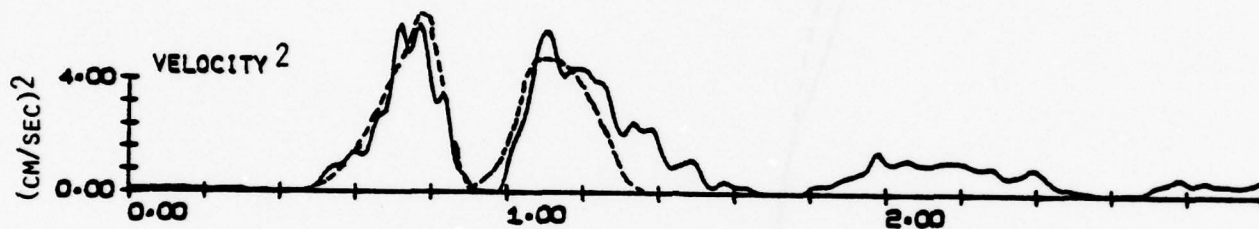
SHUMAGIN ISLANDS 0153 EVENT

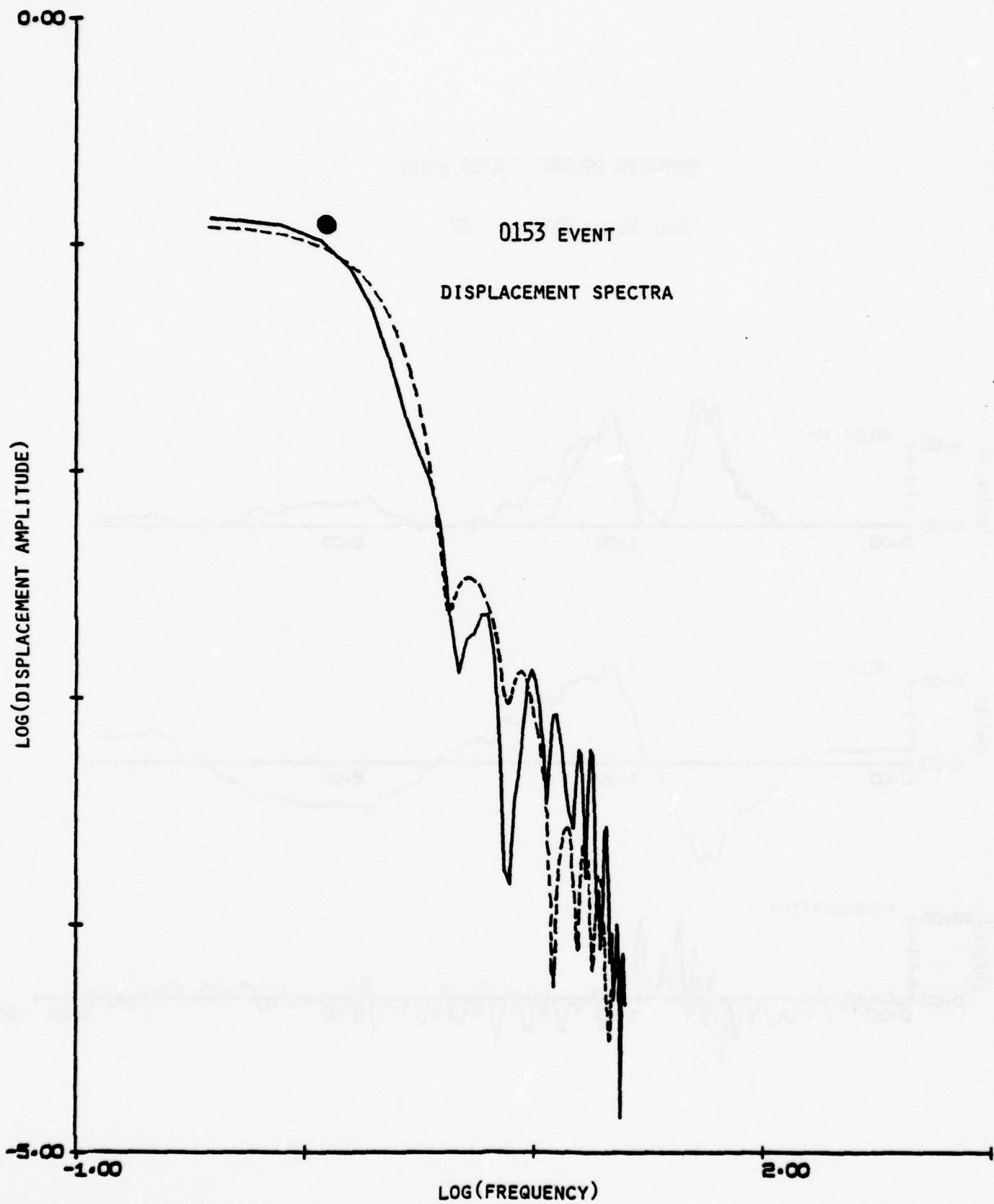
SAND POINT SMA1 SV

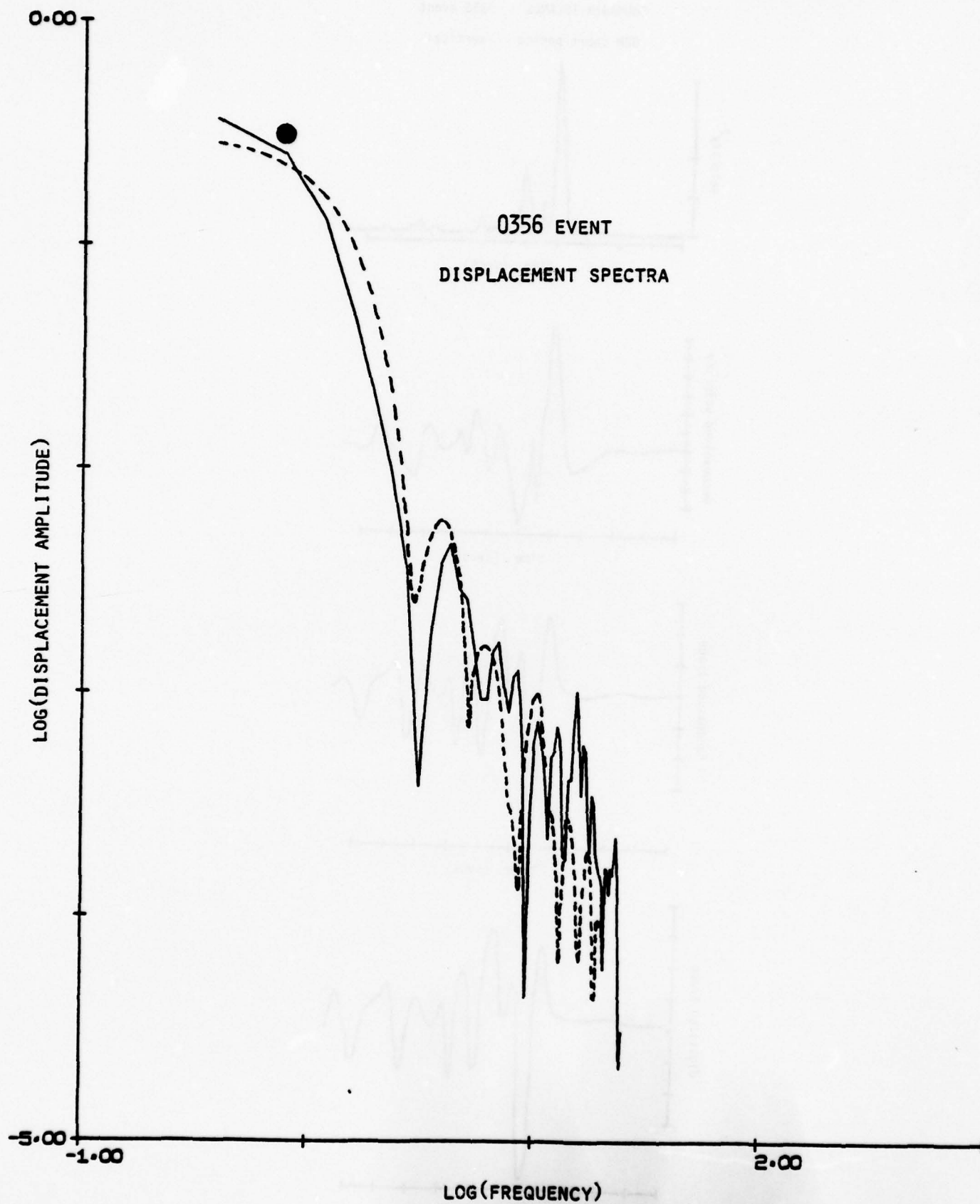


SHUMAGIN ISLANDS 0356 EVENT

SAND POINT SMA1 SV

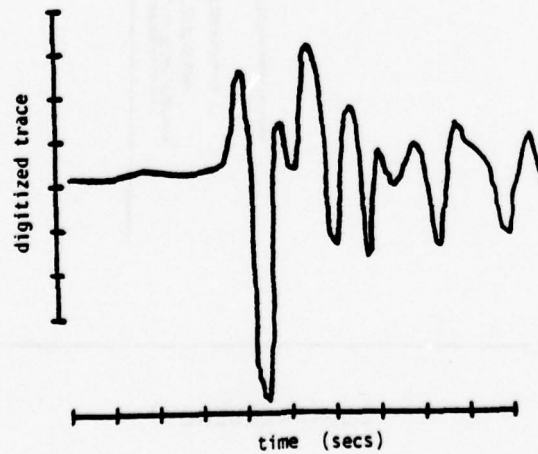
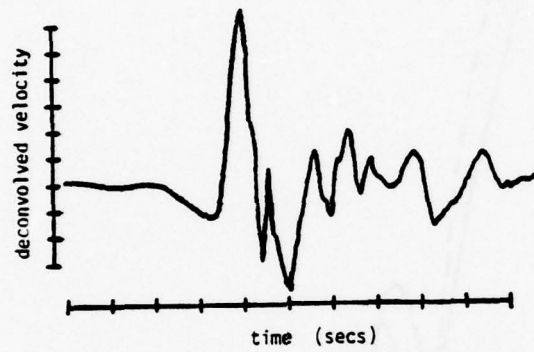
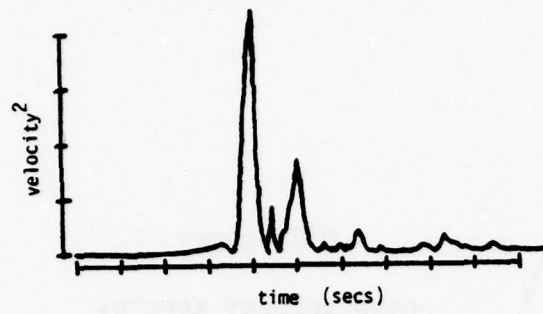


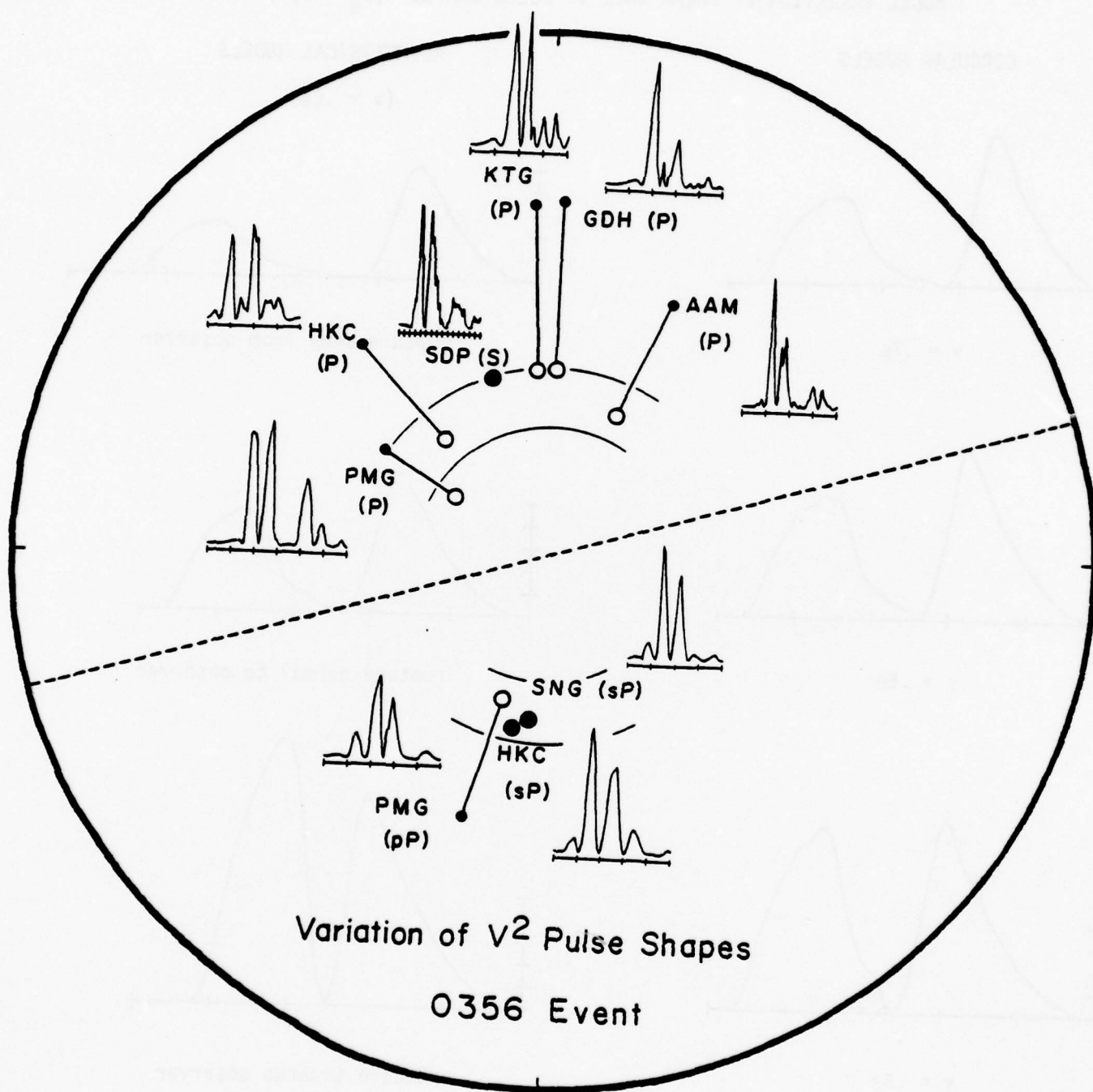




SHUMAGIN ISLANDS 0356 event

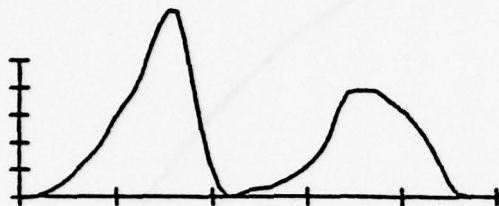
GDH short period vertical



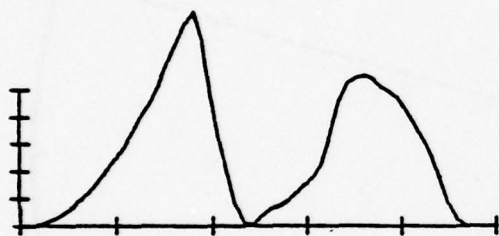


MODEL VARIATION OF SHEAR WAVE v^2 PULSE SHAPES ($\theta_\beta = 30^\circ$)

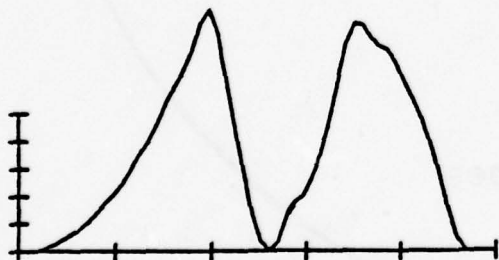
CIRCULAR MODELS



$v = .7\beta$



$v = .6\beta$



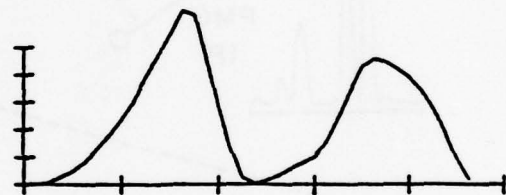
$v = .5\beta$

ASYMMETRICAL MODELS

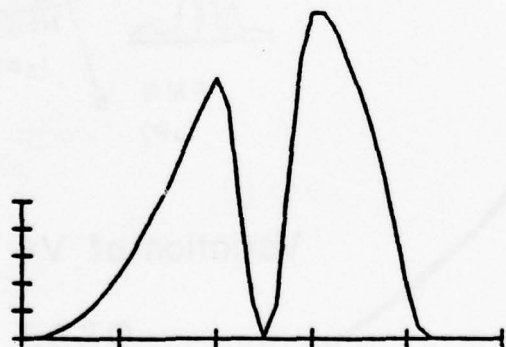
($v = .6\beta$)



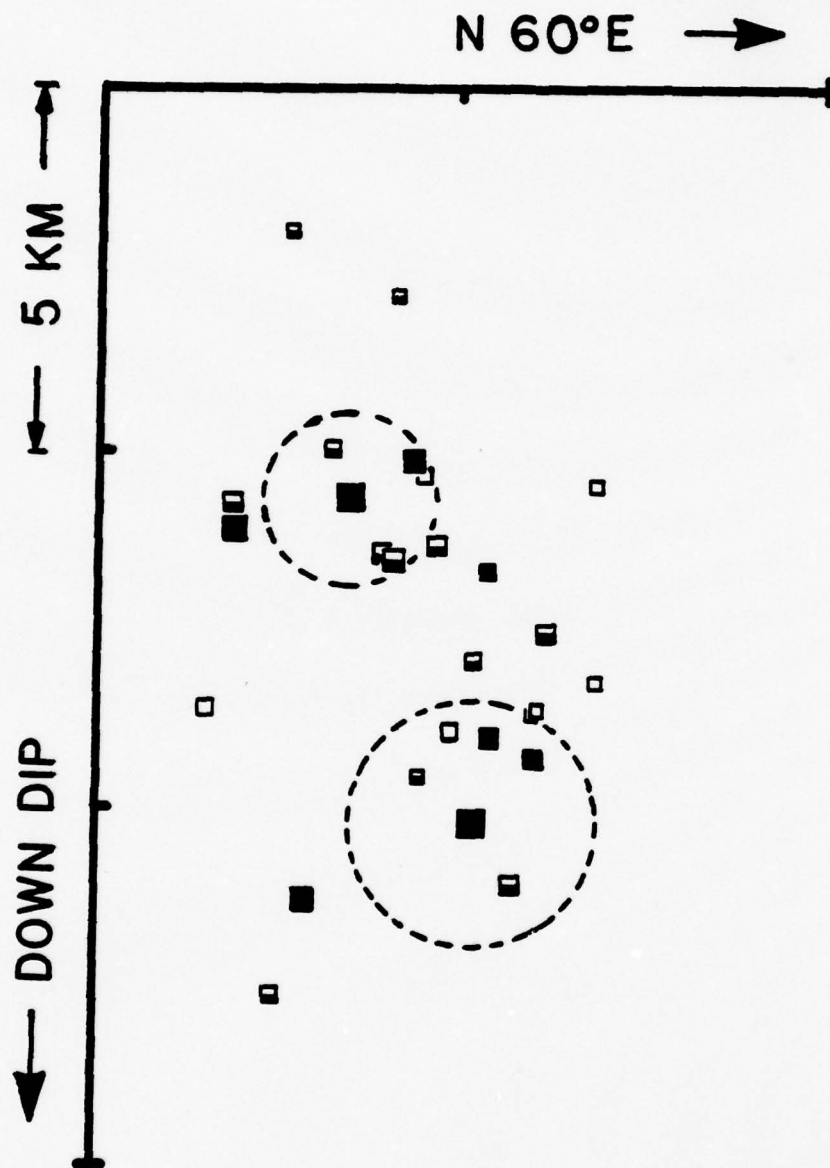
rupture away from observer



rupture normal to observer



rupture towards observer



INVESTIGATION OF TWO HIGH STRESS-DROP EARTHQUAKES
IN THE SHUMAGIN SEISMIC GAP, ALASKA¹

Leigh House and John Boatwright

*Lamont-Doherty Geological Observatory and
Department of Geological Sciences of Columbia University
Palisades, New York 10964*

ABSTRACT

Two moderate size ($m_b = 5.8, 6.0$) earthquakes occurred within a local network of short-period seismograph stations in the Shumagin Islands, Alaska, on April 6, 1974. They were followed by 69 aftershocks recorded over the next two weeks. Both mainshocks triggered a strong-motion accelerograph (SMA) at Sand Point, 50 km NNW of their epicenters.

High quality locations obtained from local network arrivals for the mainshocks and 29 aftershocks plot at depths between 35 km and 45 km and define a plane dipping about 30° to the NW. A nearly pure-thrust focal mechanism for the larger ($m_b = 6.0$) earthquake was obtained from long-period data. The fault plane dips 30° in the direction $N 16^\circ W$. This sequence was located along the dipping seismic zone beneath the eastern Aleutians and was presumably related to underthrusting of the Pacific plate beneath North America.

We obtained estimates of the source parameters of these earthquakes from analysis of SMA data and WWSSN short period data. WWSSN data indicates that the earthquakes ruptured a nearly circular zone. Modelling of the SMA records with a quasi-dynamic model [Boatwright, 1979] provides the following source parameter estimates for the $m_b = 5.8$ and 6.0 earthquakes respectively: moments, M_0 , 3.6 and 6.6, $\times 10^{24}$ dyne-cm and stress drops: 650 and 540 bars. A high

¹Lamont-Doherty Geological Observatory Contribution Number 0000.

frequency spectral fall-off of ω^{-3} suggests that the ruptures stopped gradually.

The Shumagin Islands region is believed to have a high potential for a future large earthquake [Kelleher, 1970; Sykes, 1971; Kelleher et al., 1973]. The location of this earthquake sequence at the deepest part of the rupture zone of the 1938 earthquake ($M_s = 8.7$) (major earthquake ruptures of ten initiate at depth and propagate updip) and the high stress-drops of the shocks in 1974 may indicate considerable accumulation of stress prior to a major earthquake in the Shumagin Islands region.

INTRODUCTION

Two moderate size ($m_b = 5.8, 6.0$) earthquakes and their aftershocks, which occurred within the Shumagin Islands Seismic Network, Alaska, have produced a unique data set for a detailed study of the tectonics at depth in an area which has been identified as a seismic gap. In order to fully describe this earthquake sequence, this study integrates the locations and magnitudes from the seismic network, the strong motion accelerograph recordings of both events, and short-period WWSSN data from the larger event.

The April, 1974 sequence began at 0153 hours on April 6, 1974, with a moderate size ($m_b = 5.8$) mainshock. This was immediately followed by aftershocks, including one of magnitude 4.3 at 0227 hours. A second, and larger ($m_b = 6.0$), mainshock occurred at 0356 hours. Over the next two weeks there were nearly 70 aftershocks, three of which had body wave magnitudes greater than 4. Considering only the teleseismic locations, the sequence resembles a swarm as the mainshocks are so close in both location and magnitude. Using the local network locations, however, it is clear that there were two distinct mainshocks which had separate rupture areas. The range of hypocentral depths for these events is between 37 and 43 km.

The Lamont-Doherty Geological Observatory has operated a network of vertical short-period, radio-telemetered stations in the Shumagin Islands region of Alaska since July 1973. As originally installed, the network consisted of high-remote stations which telemetered their data to a central recording site at Sand Point (SDP, see Figure 1). Severe environmental factors resulted in numerous station outages over the winter season. By April, 1974, when the sequence occurred, only four of the remote stations were operating.

Both mainshocks triggered a strong motion accelerograph (SMA-1) located at Sand Point. These recordings, complemented by a qualitative analysis of the rupture geometry using WWSSN short-period data, are modelled using the techniques and models discussed by Boatwright [1979], which focus on the determination of the rupture velocity, and which provide more reliable estimates of stress release.

Archambeau [1978] made a survey of earthquakes along the Aleutian arc using m_b to M_s ratios and obtained high stress drops for these two mainshocks ($\Delta\sigma \approx 500$ bars). Our study confirms his identification of these events as high-stress drop earthquakes, and in addition, provides considerable insight into the character of the deformation at this depth in the Benioff zone.

Analysis of Shumagin Network Data

During the two weeks following the mainshocks of April 6, 1974, more than 70 aftershocks occurred which were large enough to be recorded by the station at Squaw Harbor (SQH, see Figure 1). Of these, 4 were large enough ($m_b > 4.0$) to be recorded teleseismically. Seismic stations which were operating at the time of these earthquakes were: SDP, PVV, SQH, SGB, and CNB (see Figure 1). CNB was working only intermittantly and recorded only about 1/2 of the sequence. Unfortunately, the station nearest the sequence, NGI, did not record any of the sequence.

Our earthquake location procedure consisted of reading arrival times from magnetic tape playbacks (with a precision of 0.2s) and using a variation of the HYPO 71 program [Lee and Lahr, 1972] to obtain hypocentral coordinates from the arrival times. We had no difficulty making P arrival time picks, as the P phase was generally quite impulsive. Since only vertical seismometers are installed at the remote stations, making reliable picks for S arrivals was quite difficult. In general, we used only S arrival times from the SDP station, which has 2 horizontal short period seismometers, in addition to a vertical.

In order to reduce the magnitude of the overall station residuals, we applied station corrections to arrival times. We averaged the station residuals from the two main shocks and the first large aftershock (April 6, 0227 hrs, $m_b = 4.3$), and applied the corrections to arrivals from the whole suite of events. The largest residual, -0.1s, was at station SQH; the rest were ± 0.05 s or less.

By obtaining earthquake locations both with and without arrival times from CNB, we determined that, although there is no significant bias of locations which don't use CNB arrival times as compared with those which do, there is an increase in scatter of the locations which don't use CNB arrival times recorded at CNB. This restriction reduced the number of aftershocks we located to 27. We feel that these locations are the most reliable of those from the whole sequence and estimate hypocentral location errors to be less than 5 km in an absolute sense, and in a relative sense, less than 2 km for our "A" quality solutions.

Locations of the April 6, 1974 mainshocks and well located aftershocks are plotted in map view in Figure 1. Two open circles within the box are network locations of the two mainshocks. The PDE (teleseismic) location for these events is plotted as the open circle about 20 km to the NNW of their network locations.

Network locations for the whole sequence are plotted in the inset. Main shock locations are circled; the first, at 0153 hours on April 6, is trenchward of the second, which occurred two hours later, at 0356. Note the separation of aftershocks into two adjacent, but distinct groups.

The location of the cross section in Figure 2 is indicated in Figure 1 by the line which terminates just SE of the Aleutian Trench. The cross section extends slightly beyond the northern edge of Figure 1.

Four years of Shumagin Seismic Network data are plotted in cross section views in Figure 2. This figure illustrates the well-defined 10 km thin Benioff zone which exists within the central portion of the network. The April 6 sequence occurred within the area of the box, at a depth of 40 km. Davies and House [1979] noted that if the seismicity below about 40 km occurs near the upper surface of the descending slab, then there must be a bend in the slab at about 40 km. This is necessary because the seismic zone below 40 km dips at about 30° , whereas, between the trench and 40 km depth, the slab dip is about 15° . Thus, the April 6 sequence occurred very near this bend in the slab. The inset in Figure 2 is an enlarged cross section of the area of the April 6, 1974 sequence. The first main shock, at 0153 hours, is shallower, and trenchward of, the 2nd main shock. Dashed lines represent the rupture dimensions as estimated from the source modelling. The rupture zones are plotted with a dip of 30° , which is the clip of the fault planes we infer for these events. Symbol size is scaled to magnitude, the largest event is the second mainshock ($m_b = 6.0$), the smallest event plotted has a magnitude of about 1.5. Symbol filling indicates quality of the location. Filled symbols are used for the best quality locations ("A" quality), 1/2 filled for the next best ("B" quality) and open symbols for worst quality ("C"). Relative hypocentral errors are about 1.5 km

for the "A" quality locations, 2 km for "B" quality and 3.5 km for "C" quality. Errors in "A" quality locations are about the same magnitude as the rupture radius of the first mainshock (1.3 km), those for "B" quality about the same magnitude as the rupture radius of the second mainshock (1.8 km).

Figure 3 is an inclined cross section view of the April, 1974 sequence. The projection plane is oriented parallel to the fault planes of the mainshocks, and the "view" of this figure is upwards at the fault plane. In this figure the first main shock (0153 hours) is above the second (0356 hours). The dashed circles represent the rupture areas of the two mainshocks as inferred from the SMA data. Symbol size and filling represent magnitude and quality of the solutions as in the previous figure. Note that the aftershocks cluster about the two main shocks, and, in general, are indicative of two distinct rupture areas. There is, however, some scatter, which is probably partly the result of location errors, but which may also suggest that deformation during this sequence extended beyond the immediate rupture zones of the mainshocks. The first large aftershock ($m_b = 4.3$) occurred at 0227 hours, on April 6 (just 1/2 hour after the first mainshock). It is plotted as the large, filled symbol to the left of, and slightly below the first mainshock, as shown in Figure 3. The second large aftershock ($m_b = 4.1$) occurred at 0509 hours on April 6, and plots as the solid square to the left of, and slightly below, the 2nd mainshock. Thus, the locations of these larger aftershocks also suggests that deformation during the sequence extended beyond the immediate mainshock rupture areas. The scatter in aftershocks plotted in the inset of Figure 2 is consistent with this concept.

Focal Mechanism of the Main Shocks

We obtained the focal mechanism of the second mainshock ($m_b = 6.0$), shown

in Figure 4, primarily from long period arrivals at WWSSN stations. Both S wave polarizations and P wave first motions were used. There is only one inconsistency in the first motions, and that is a less reliable pick. This mechanism is consistent with the local network short period first motions, which are the square symbols in Figure 4.

Since error in determination of the mechanism would produce error in the source parameter estimates (see below), we wanted to extract the maximum constraint possible from the data and quantify error in the focal mechanism. We selected S wave polarizations from 9 stations which had clear S arrivals, and used the S arrival from the SDP SMA, as well, and obtained a mechanism which produced a minimum S wave polarization residual. We also used this information to obtain 1-standard deviation error estimates. Focal parameters and error limits are: strike, $254^\circ \pm 15^\circ$, dip $30^\circ \pm 5^\circ$, rake (of slip vector) $90^\circ \pm 15^\circ$. These errors are indicated on Figure 4, as are the associated errors in the T and P axes. First motion and S wave polarization data are fewer, but identical, for the first mainshock ($m_b = 5.8$).

Since the network located seismic zone, and the general distribution of aftershocks (see Figure 2) are very nearly parallel to the NE-SW striking, 30° dipping nodal plane, we prefer this to be the fault plane of these events. The SMA wave forms at SDP are also consistent with this choice of fault plane. Thus, these earthquakes were shallow-angle underthrusts of Pacific lithosphere beneath North America. Shallow angle underthrusting, with mechanisms similar to this one has been observed along the Aleutians, by investigators such as Stauder [1968] and Bollinger and Stauder [1966]. Since their fault planes are parallel to the Benioff zone, as shown by the network locations, below 40 km, it appears that the Pacific plate has already made the bend to a steeper dipping geometry by the time it has reached the 40 km depth of these earthquakes.

SMA-1 Waveform Analysis

The SMA-1 records from the 0153 and 0356 events were photographically enlarged, digitized and instrument corrected using the techniques discussed in Boatwright (1978). Since the Sand Point station was at an SH mode, the vertical and horizontal components were combined to obtain the incident SV pulse shape, using the free surface transformation,

$$u_{sv}(t) = \frac{\cos 2j}{2 \cos j} u_x(t) + \sin j u_z(t). \quad (1)$$

Here j is the angle of incidence of the s-wave, $u_x(t)$ is the horizontal component (positive away from the source) and $u_z(t)$ is the vertical component (positive downward). This (real) transformation was derived from Chapter 5, problem 5.6, of Aki and Richards (1979). The resulting SV acceleration traces for both events are shown in Figures 6 and 7, along with their respective velocity and v^2 traces. The integration to velocity was performed using a parabolic baseline technique detailed in Perez, Husid and Espinosa (1979). Both accelerograms show a significant 12 hz site response which is substantially reduced in the integration to velocity.

The v^2 -plots detail the energy flux of the body wave arrival. Their non-linear signal enhancement make them a strong tool for seismic source studies. The v^2 -plots of the sv phases at Sand Point are remarkably similar in shape and amplitude, although the 0153 pulse shape is noticeably more impulsive. This similarity indicates that the events probably share nearly the same rupture geometry as they have same focal mechanism. The large relative amplitude of the healing phase suggests either that the rupture propagated towards the Sand Point station (downdip) or that the rupture velocity was slow, about .6 of the shear wave velocity, if the rupture was approximately circular (see Boatwright, 1979). These two possibilities are considered in the discussion of the WWNSS

short period data. The final model v^2 -plots are shown along with the data as dashed lines.

In Figures 8 and 9, we show the displacement spectra for the two events, as well as the final model spectra (dashed lines). The data has been corrected for attenuation assuming a shear wave Q of 300. The site amplification at 10-15 Hz shows up very strongly in these spectra. The corner frequencies, marked by dots, were estimated assuming this amplification to be spurious. The corrected velocity spectra were integrated to obtain the integral of the squared ground velocity (say I_B).

The spectral and pulse shape parameters for the two events necessary for the estimation of the rupture dimensions are compiled in Table 1. Following Boatwright, (1978a), the characteristic frequency, η_B , is defined as

$$\eta_B = \left(\frac{I_B}{\bar{u}_B^2} \right)^{1/3} \quad (2)$$

where \bar{u}_B is the low frequency asymptote. This spectral measurement provides an estimate of the source dimension (radius = a) through the relation,

$$\kappa_B = \left(\frac{a}{v} \right) \eta_B \quad (3)$$

where v is the rupture velocity and $\kappa_B = 69$ for this takeoff angle. The rise time, $\tau_{1/2}$, to be the measurable width of the first pulse of the v^2 -plot (the rupture phase), may also be used to estimate the source dimension, from the empirical relation (Boatwright, 1979),

$$\tau_{1/2} = \frac{(13-12\phi)}{16} \left(\frac{a}{v} \right). \quad (4)$$

Here $\phi = \frac{v}{c} \sin \theta$ is the ratio of the rupture velocity to the phase velocity of the ray along the fault surface. The results from these three source dimension estimates are shown in Table 2. If we assume the ratio of the rupture velocity,

to the shear velocity to be bounded as $.55 < \frac{v}{3} < .8$, then we obtain the first order estimates of $1.0 < a < 1.4$ km for the 0153 event and $1.4 < a < 2.0$ for the 0356 event.

WWNSS Waveform Analysis

Before fitting for a particular rupture model, it is necessary to investigate the rupture geometry of the 0356 event. We have analyzed 9 short period P-wave arrivals from 6 WWNSS stations. The steps of this analysis are shown in Figure w, using the P-wave recorded at GDH as an example. The lowest trace is the seismogram as digitized, and the trace above it, the seismogram after filtering with a zero-phase bandpass filter. This filter is made up from a triangle smoothing operator and a second order Butterworth high pass filter (corner at .3 Hz) run forwards and backwards on the trace. The third trace is the ground velocity, obtained by a recursive deconvolution scheme derived from a bilinear approximation to the coupled galvanometer-seismometer response. The uppermost trace is the square of the ground velocity. It is these v^2 -plots which we will use to constrain the rupture geometry of the event.

In Figure 11 we show the variation of the v^2 -plots over the focal sphere. The P, pP and sP takeoff angles are shown relative to the fault plane, rotated into the plane of the figure, together with their respective v^2 pulse shapes. To account for the pulse shape differences between the P and S body waves, the phases leaving as P-waves have been corrected to the appropriate take-off angle (open circles) for an S-wave having the same phase velocity along the fault surface, which requires the far-field pulse shapes to be identical. From Kostrov (1970), this corrected take-off angle is

$$\theta_s = \sin^{-1} \left(\frac{\beta}{\alpha} \sin \theta_p \right) \quad (5)$$

where θ_β and θ_α are measured from the normal to the fault plane. Note that

almost all the corrected takeoff angles lie between 20° and 30° . The line across the stereonet marks the strike of the Benioff zone.

In order to evaluate the variation of these v^2 -plots, in Figure 12 we show the synthetic variations of the v^2 -plots over our model range. For these synthetics, we have used both circular and slightly asymmetrical versions of the quasi-dynamic models discussed in Boatwright (1979), fixing the ratio $\frac{a}{v}$.

In the left-hand column of Figure 12, we show the variation of the v^2 pulse shape for different rupture velocities where the takeoff angle of the ray is at 30° from the normal to the fault plane. These same synthetics may also be used to describe the variation of the v^2 pulse shapes for different takeoff angles. For a circular rupture with rupture velocity $v = .6 g$, the upper and lower figures approximate the v^2 pulse shapes at 37° and 24° , respectively, from the fault normal. The contrasting interpretations of these synthetics result from the approximate similarity of pulse shapes having similar values of $\frac{v}{c} \sin \theta$, for similar rupture models.

In the right hand column, we detail the pulse shape variations for different directions of asymmetrical rupture growth relative to the observer. In these synthetics, the takeoff angle is 30° from the fault normal and the rupture velocity is $v = .6 g$. The asymmetrical models have about an 11% unilateral rupture: if $\xi_f(\phi)$ is the distance from the hypocenter to the perimeter of the fault in the ϕ direction, the percent unilateral rupture is given as

$$100 \max \left\{ \frac{\xi_f(\phi) - \xi_f(\phi + \pi)}{\xi_f(\phi) + \xi_f(\phi + \pi)} \right\} \quad (6)$$

Note how the asymmetrical models produce a strong variation of the peak separation in the v^2 pulse shapes over the focal sphere, as well as varying the relative amplitude of the peaks. This difference will also help resolve the trade-

off between rupture velocity and rupture geometry.

In Figure 11, much of the more striking variations of the v^2 -plots appears to result from differences in the crustal structure beneath the stations used. The Sand Point v^2 pulse shape has been plotted with the same time scale, in order to show the relative attenuation present in the short period WWNSS data. In particular, it is necessary to point out the broadening (perhaps due to attenuation) of the HKC pulse shapes, with respect to the pulse shapes at nearly the same takeoff angles. Also the pulses at GDH and AAM appear to have a crustal reverberation which is interfering destructively with the healing phase of the v^2 pulse shape. This interference may be seen in the plots of the WWNSS analysis in Figure 10 as well.

The slight differences (in relative amplitude and timing) of the depth phase (updip) pulse shapes relative to the downdip pulse shapes suggests that the rupture had a slight downdip component of unilateral rupture velocity (about 5%) and a rupture velocity of about $v = .6 g$. Because of the narrow band of the short period WWNSS instruments and the (unknown) crustal structure beneath the stations whose P-waves were analyzed, we can only use these results qualitatively. However, it is important to note that nearly all of the v^2 -plots fall within the model range spanned by Figure 12, from which we have determined the variance of our source parameter estimates. As we have estimated the ratio $\frac{a}{v}$ for these events, specifying an approximate rupture velocity and rupture geometry then determines our final models.

Final Source Models

For the final source modelling we have used two circular versions of the quasi-dynamic models. These models have the dynamically feasible "elliptical" or self-similar slip distribution during rupture growth, and causal healing.

Figure 13 shows half-view snapshots of the slip velocity for this circular model. Since the displacement spectra from these events falloff faster than ω^{-2} , we presume that the ruptures stopped gradually rather than abruptly, [Madariaga, 1978], and this gradual stopping is incorporated into the models.

Since both events were fit with circular models, the rupture velocities of the two models are slightly different: $v = .6 \beta$ for the 22 0153 event and $v = .55 \beta$ for the 0356 event; similar results would have been obtained if we had fixed the rupture velocity using a slightly asymmetrical model for the 0356 event, and a rupture velocity of $.6 \beta$ lowers the stress estimates by $\sim 20\%$. The source parameters obtained from our model fits are listed in Table 3. We have calculated the moment and radiated seismic energy using the formulae,

$$m_0 = 4\pi \rho(\xi_0)^{\frac{1}{2}} \beta(\underline{x})^{\frac{5}{2}} \ell(\underline{x})^{\frac{1}{2}} \beta(\underline{x})^{\frac{1}{2}} \frac{R(\underline{x}, \xi_0)^7}{F^{SV}(\theta, \phi)_8} \bar{u}_\beta \quad (7)$$

$$E_s = \frac{\rho(\underline{x}) \beta(\underline{x})^8}{e_\beta(\phi)_5} \left(\frac{R(\underline{x}, \xi_0)^7}{F^{SV}(\theta, \phi)_8} \right)^2 I_\beta \quad (8)$$

where $\rho(\xi_0)$, $\rho(\underline{x}) = 3.4, 2.5 \text{ gm/cm}^3$ and $\beta(\xi_0)$, $\beta(\underline{x}) = 4.4, 2.5 \text{ km/sec}$ are the densities and shear wave velocities at the source and receiver, respectively, $R(\underline{x}, \xi_0) = 52 \text{ km}$ is the geometrical spreading factor calculated following Newman [1973] and $F^{SV}(\theta, \phi) = .46$ is the radiation pattern factor. $\phi_\beta(30^\circ) .2$ is the fractional energy flux, which relates the time integrated energy flux at a particular takeoff angle to the total radiated seismic energy [Boatwright, 1979].

The effective stress or the dynamic stress drop, [Brune, 1970], also may be calculated directly from this modelling. Since the quasi-dynamic models incorporate the self-similar slip distribution described by Hoshov [1964], Burridge and Willis [1969] and others, the slip 23 distribution is scaled by the initial relative slip velocity, $A(0)$. This slip velocity is related to the dynamic stress

by the approximate relation;

$$\Delta u_o^o = v \frac{\tau}{u} \quad (9)$$

good for subsonic rupture velocities. Thus any model fit also determines effective stress by the formula;

$$\tau_e = \frac{\phi^2 \pi}{av_3^2} \rho(\xi_o)^{\frac{1}{2}} \beta(\xi_o)^{\frac{5}{2}} \rho(x)^{\frac{1}{2}} \beta(x)^{\frac{1}{2}} \frac{R(\xi_o, x)}{F^{SV}(\theta, \phi)} \frac{\dot{u}(x, t)}{\dot{\Omega}(x, t)^6} \quad (10)$$

where $\frac{\dot{u}(x, t)}{\dot{\Omega}(x, t)}$ is obtained by scaling the data, $\dot{u}(x, t)$ to the synthetics, $\dot{\Omega}(x, t)$. The model fits give $\frac{\dot{u}(x, t)}{\dot{\Omega}(x, t)} = .38$ and $.34$ for the 0153 and 0356 events,

respectively.

The results compiled in Table 3 show two systematic anomalies. For both events, the effective stress is greater than the average stress drop, while the apparent stress is substantially lower than $\tau_e/4$, which is the expected value for frictional ruptures with $v \approx .6 \beta$. However, the gradual stopping of these events may explain both anomalies. If the rupture nucleated in a localized region of high stress, the average stress drop over the rupture area might be much lower than the initial stress drop, while radiated energy would be low due to the gradual stopping. Considering the relative uncertainties of these calculations, these results are in reasonable agreement.

TABLE 1
Spectral Parameters

	<u>0153</u>	<u>0356</u>
\bar{u}_{sv}	$.13 \pm .04 \text{ cm}\cdot\text{sec}$	$.25 \pm .07 \text{ cm}\cdot\text{sec}$
I_{sv}	$2.2 \pm .6 \text{ cm}^2/\text{sec}$	$3.1 \pm .8 \text{ cm}^2/\text{sec}$
V_{β}	1.2 hz	$.8 \text{ hz}$
η_{β}	5.1 hz	3.6 hz
$\tau_{\frac{1}{2}}$	$.24 \text{ sec}$	$.37 \text{ sec}$

TABLE 2

Rupture Duration $\frac{a}{v}$

<u>Method</u>	<u>0153</u>	<u>0356</u>
Corner Frequency	.41 \pm .1 secs	.62 \pm .2 secs
Characteristic Frequency	.37 \pm .1 secs	.53 \pm .15 secs
Rise Time	.39 \pm .08 secs	.60 \pm .1 secs
Average	.39 \pm .05 secs	.59 \pm .1 secs

TABLE 3

Source Parameter0153 Event

Radius - $a = 1.2$ km

Moment - $m_0 = 3.5 \pm .8 \times 10^{24}$ dyne·cm

Stress Drop - $\Delta\sigma = 890$ bars

Range - 600-1100 bars

Effective Stress - $\tau_e = 1040 \pm 350$ bars

Radiated Energy - $E_s = 8.7 \pm 3.0 \times 10^{20}$ dyne·cm

Apparent Stress - $\tau_a = 160 \pm 60$ bars

0356 Event

Radius - $a = 1.65$ km

Moment - $m_0 = 6.7 \pm 1.5 \times 10^{24}$ dyne·cm

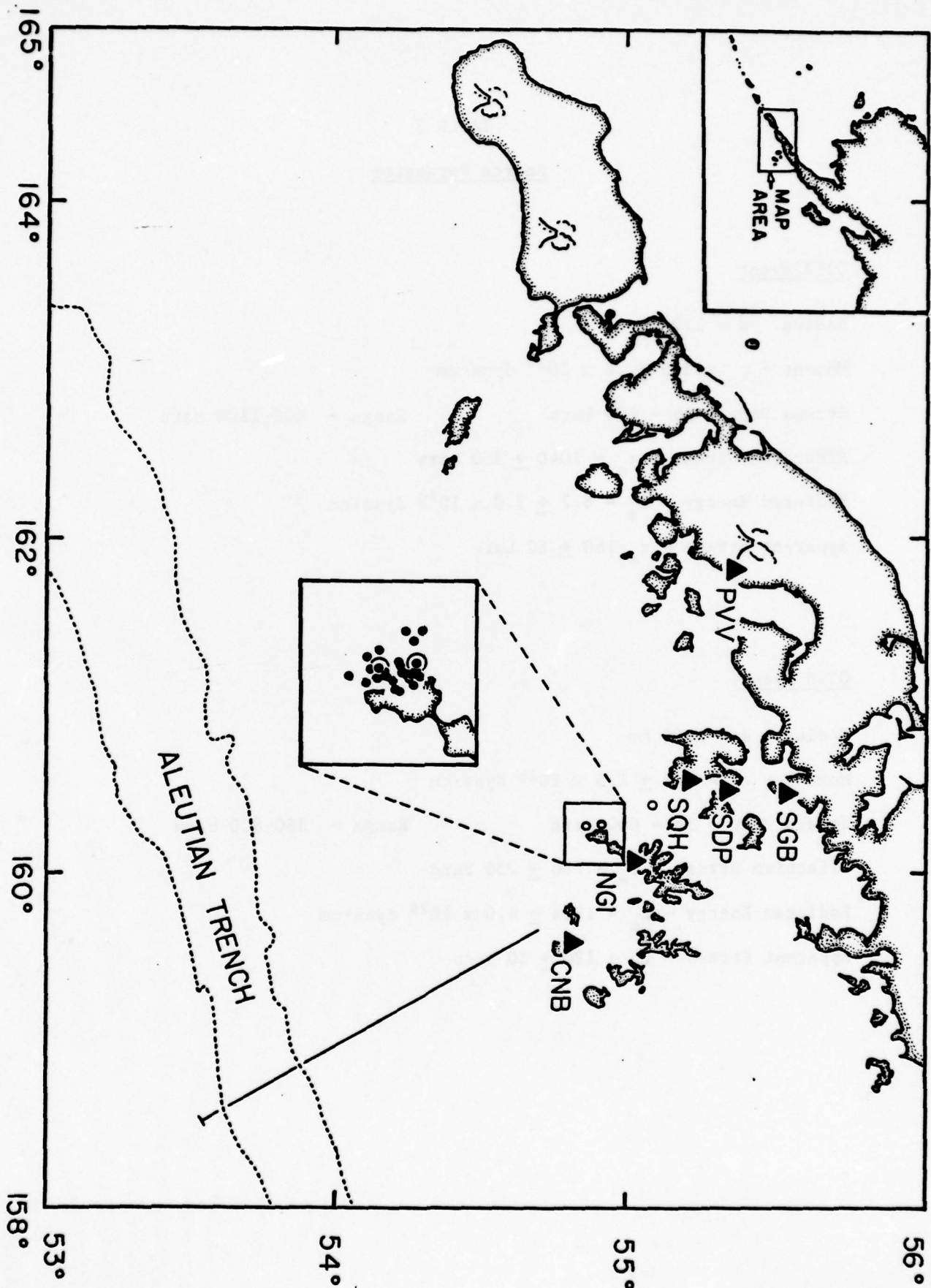
Stress Drop - $\Delta\sigma = 650$ bars

Range - 350-800 bars

Effective Stress - $\tau_e = 780 \pm 250$ bars

Radiated Energy - $E_s = 12.4 \pm 4.0 \times 10^{20}$ dyne·cm

Apparent Stress - $\tau_a = 120 \pm 50$ bars



NNW

SSE

VOLCANIC

AXIS

PVV

SGB

SDP

SQH

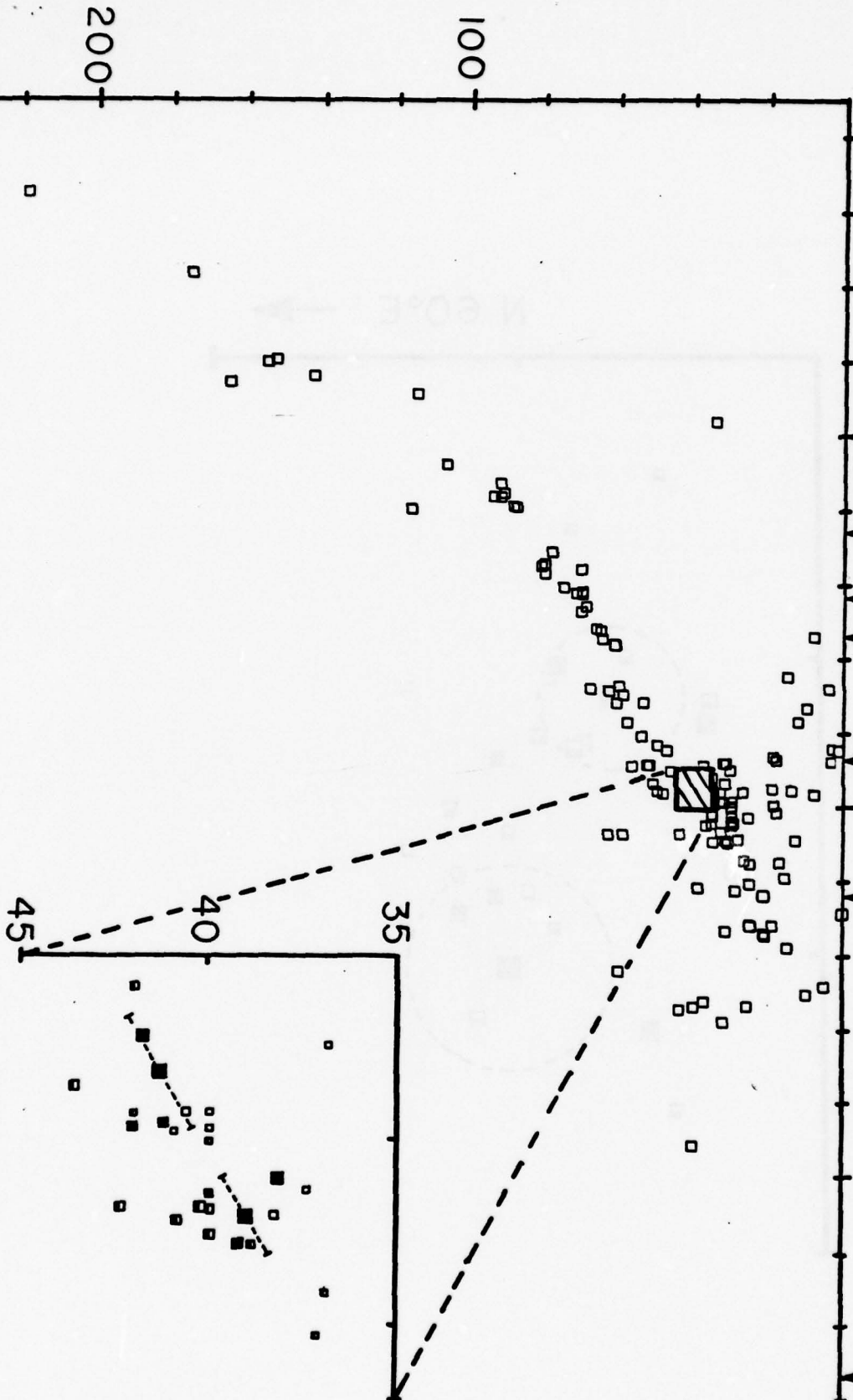
NGI

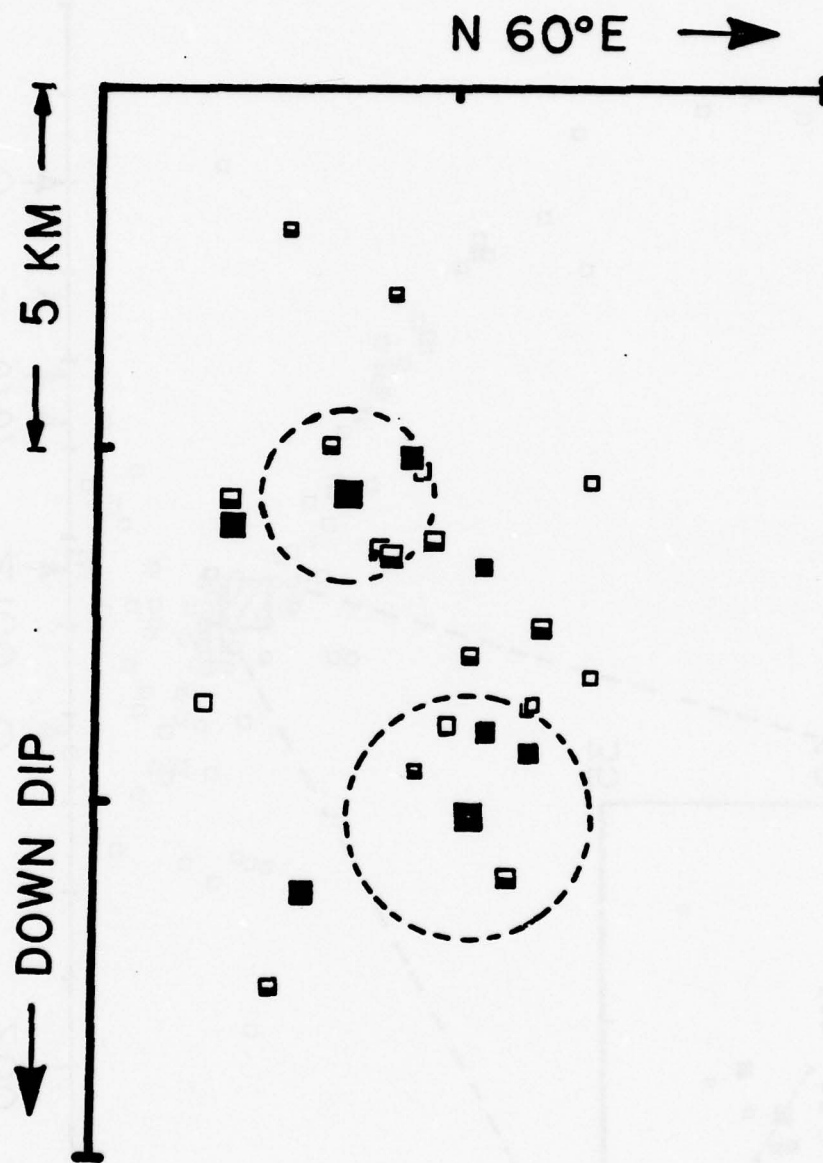
100

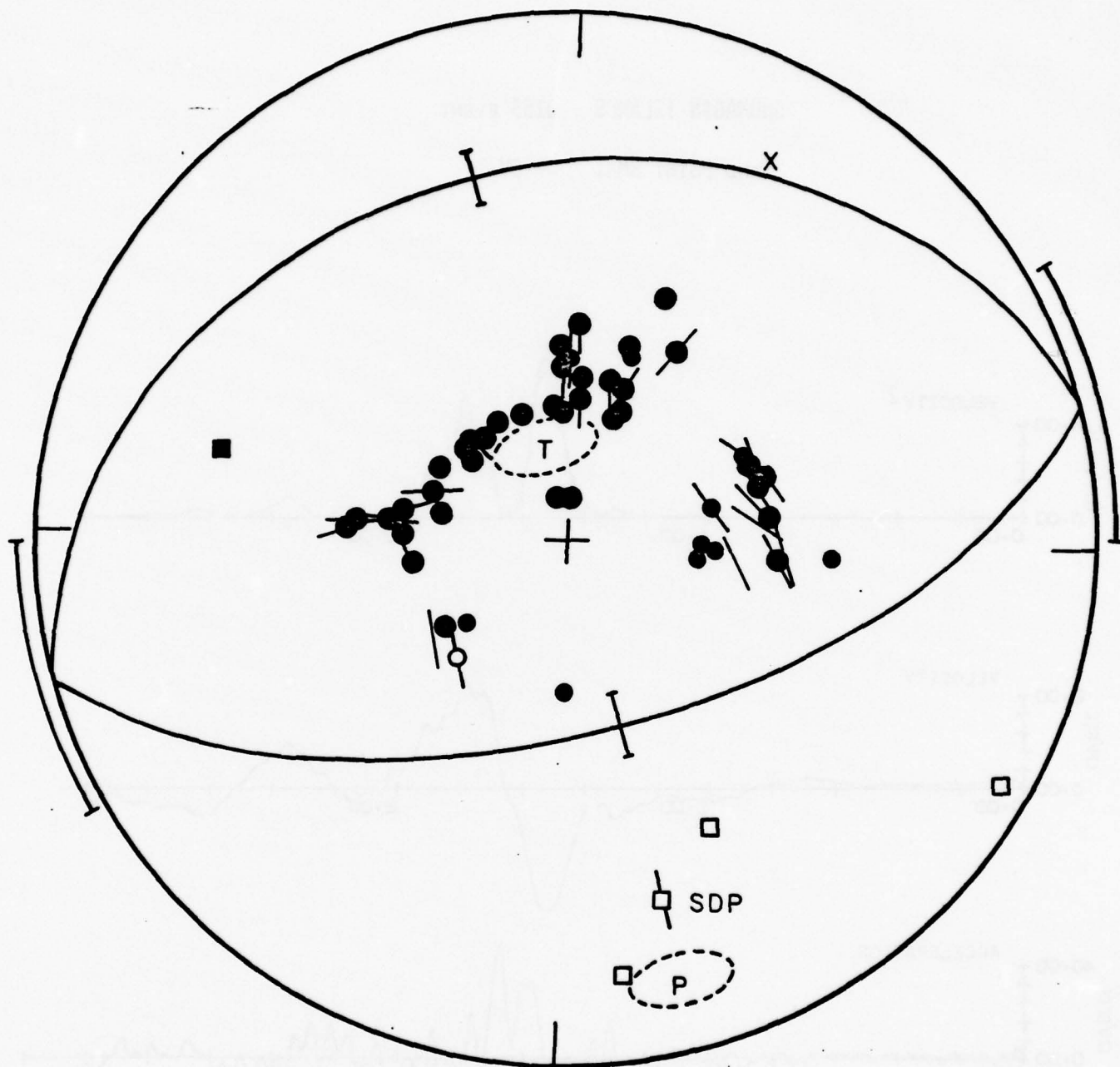
CNB

200

TRENCH



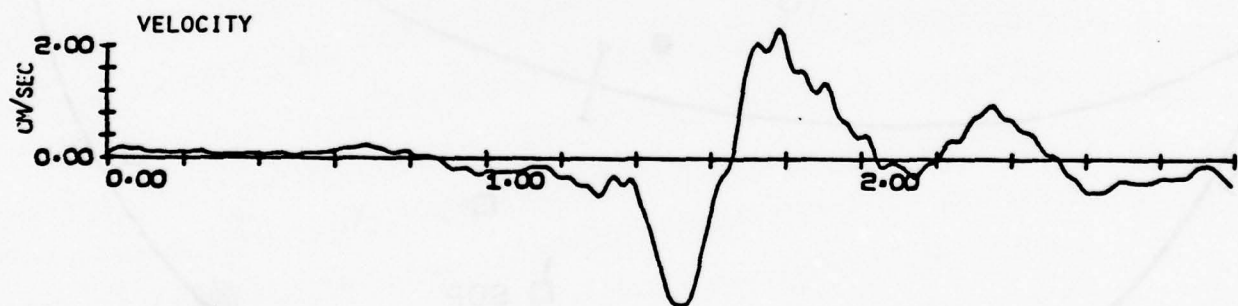
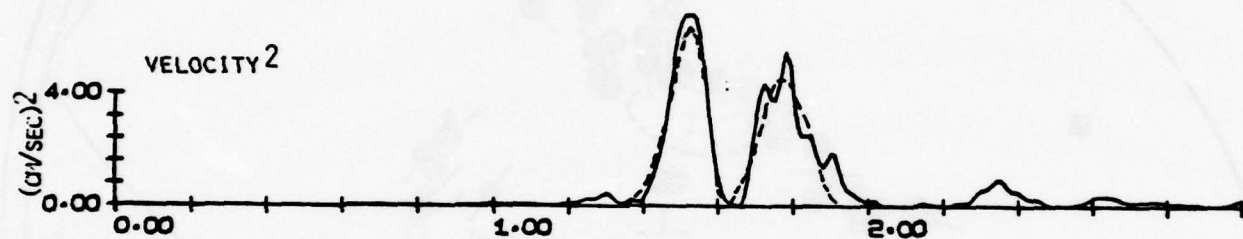




APRIL 6, 1974 0356
54.91N 160.28W 40KM

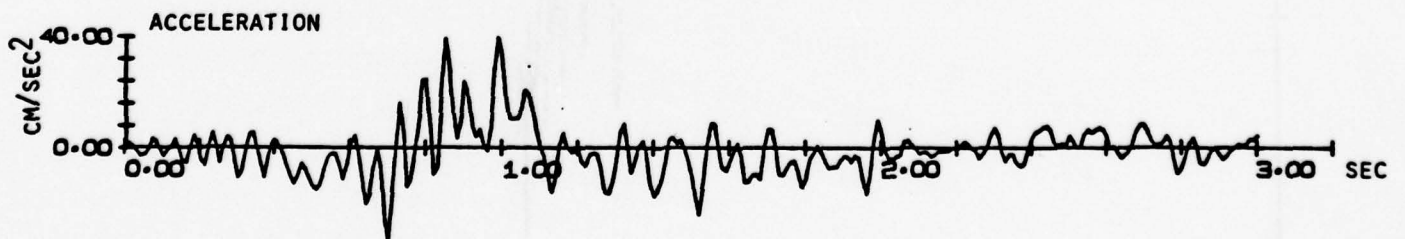
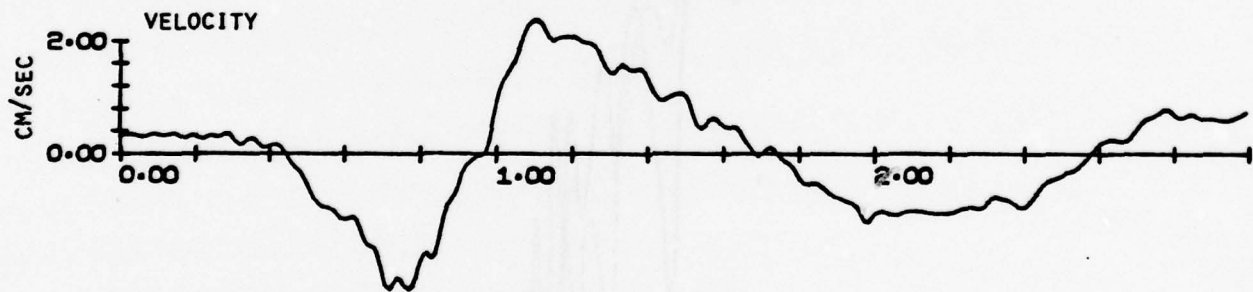
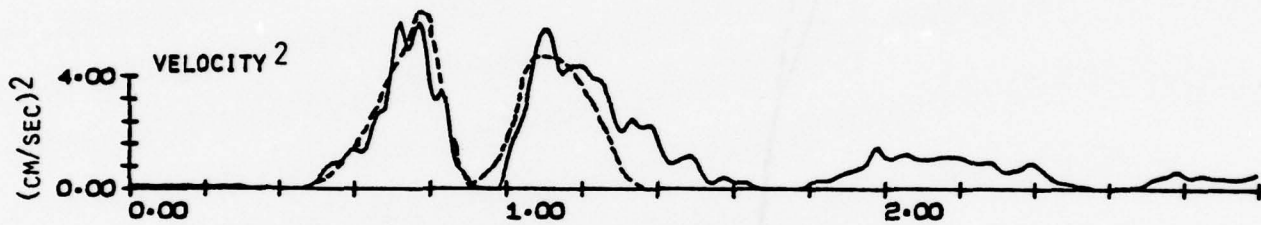
SHUMAGIN ISLANDS 0153 EVENT

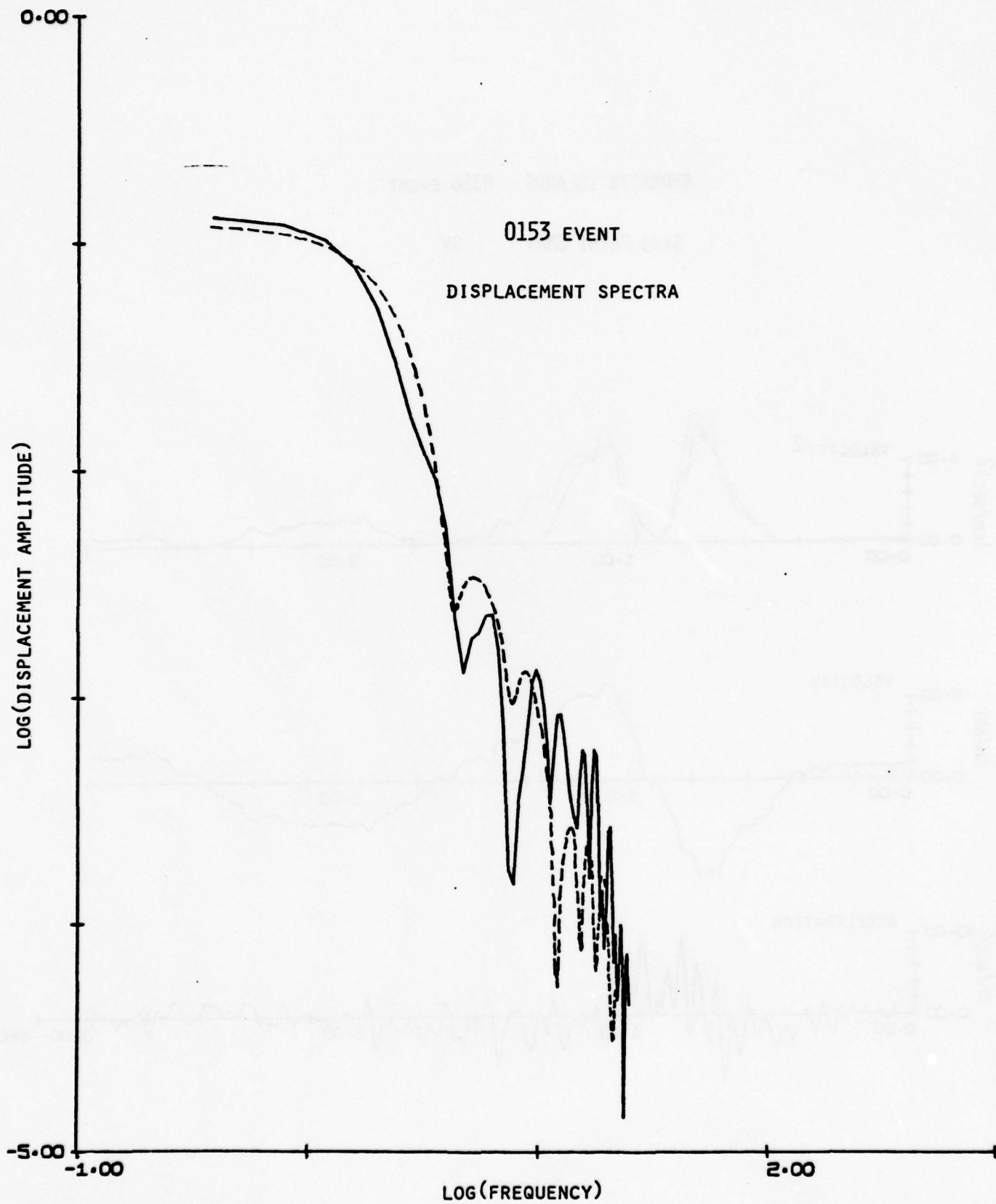
SAND POINT SMA1 SV

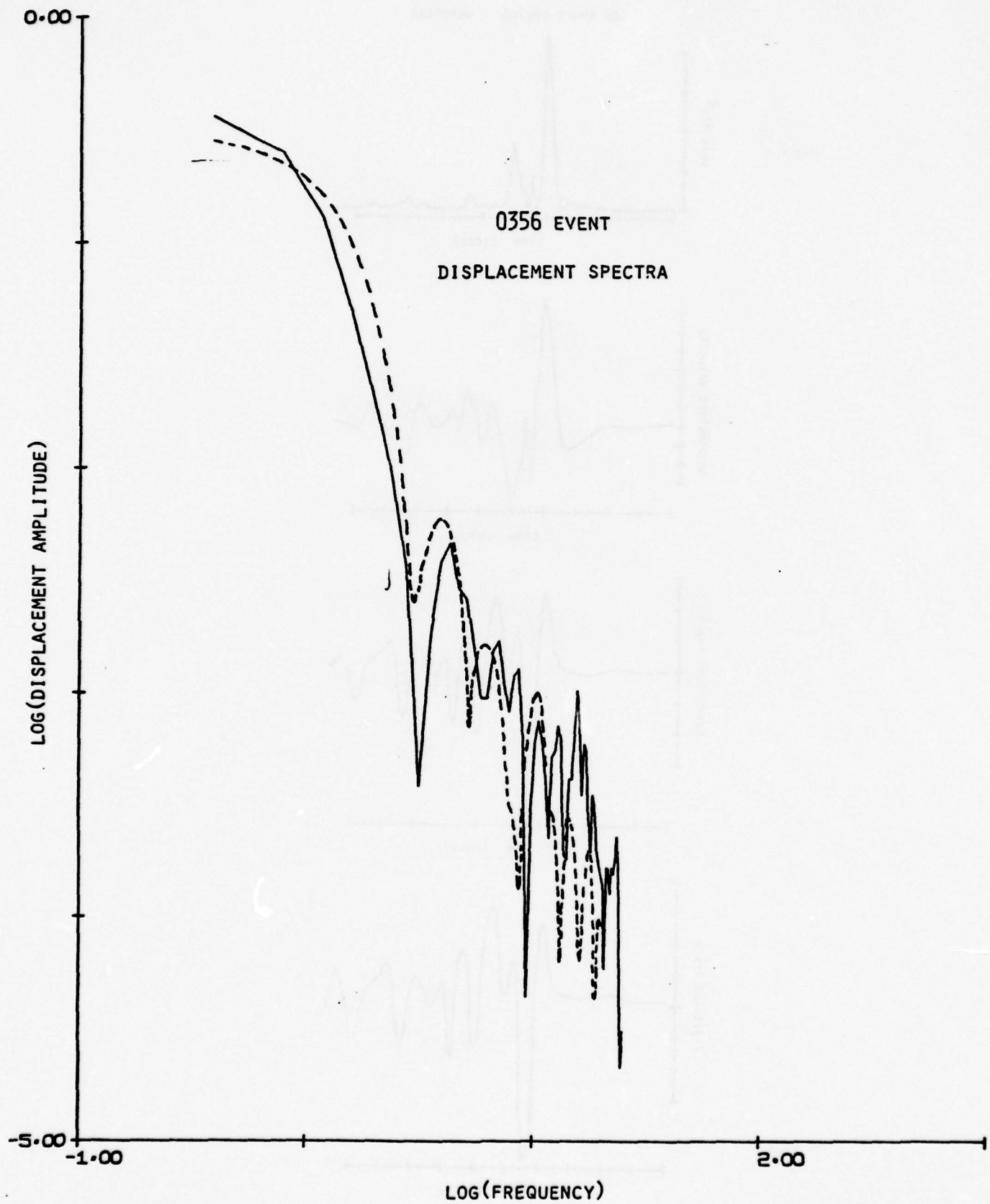


SHUMAGIN ISLANDS 0356 EVENT

SAND POINT SMA1 SV

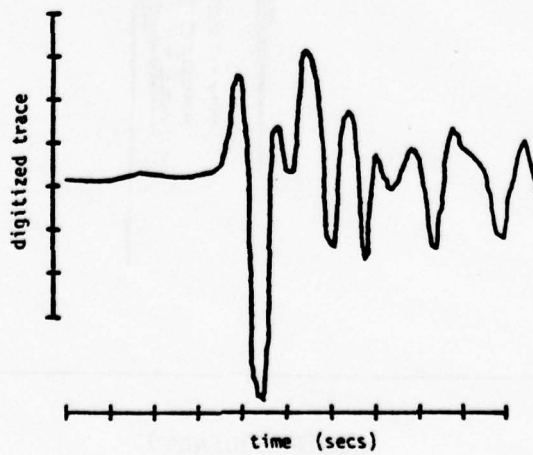
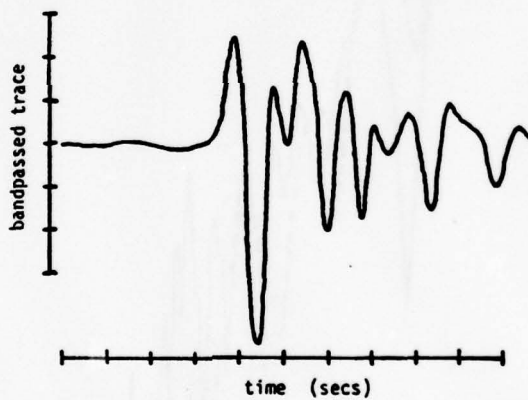
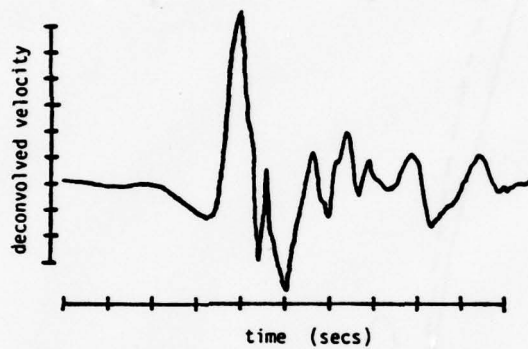
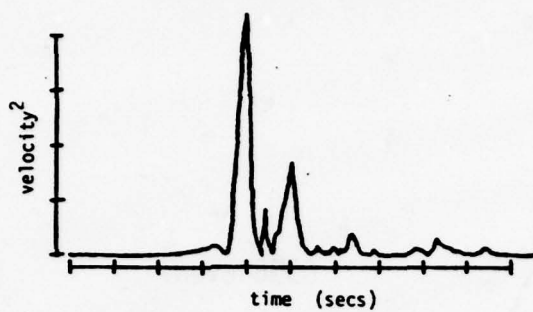






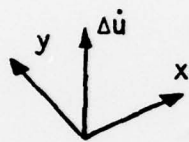
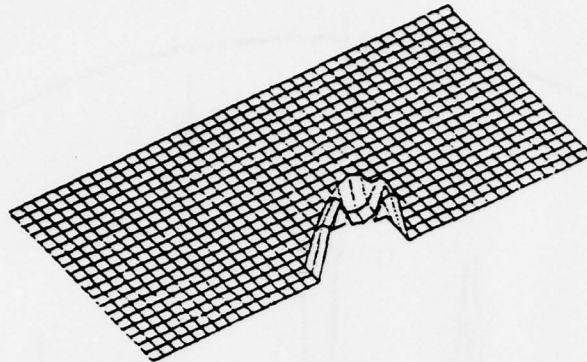
SHUMAGIN ISLANDS 0356 event

GDH short period vertical

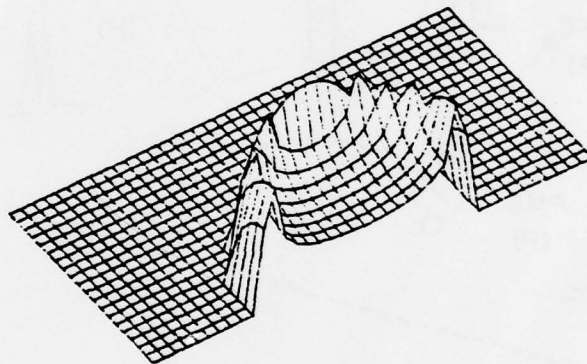


QUASI-DYNAMIC SLIP VELOCITY

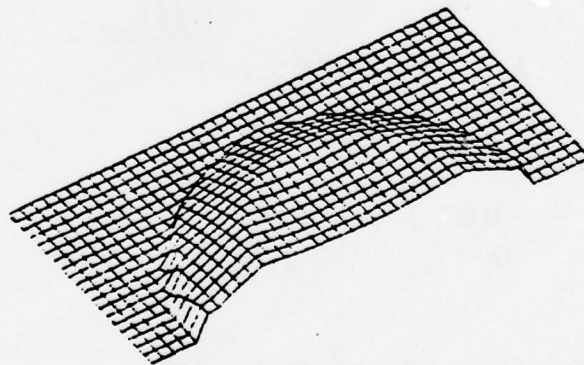
$$t = .2 \frac{a}{v}$$



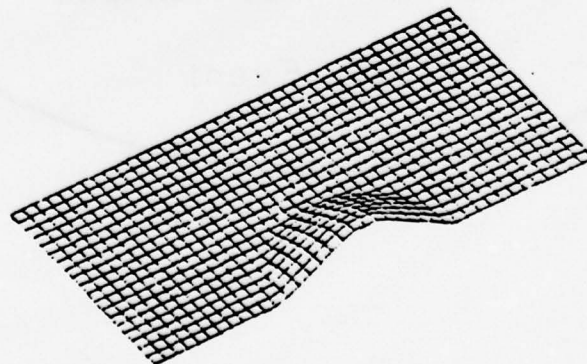
$$t = .6 \frac{a}{v}$$

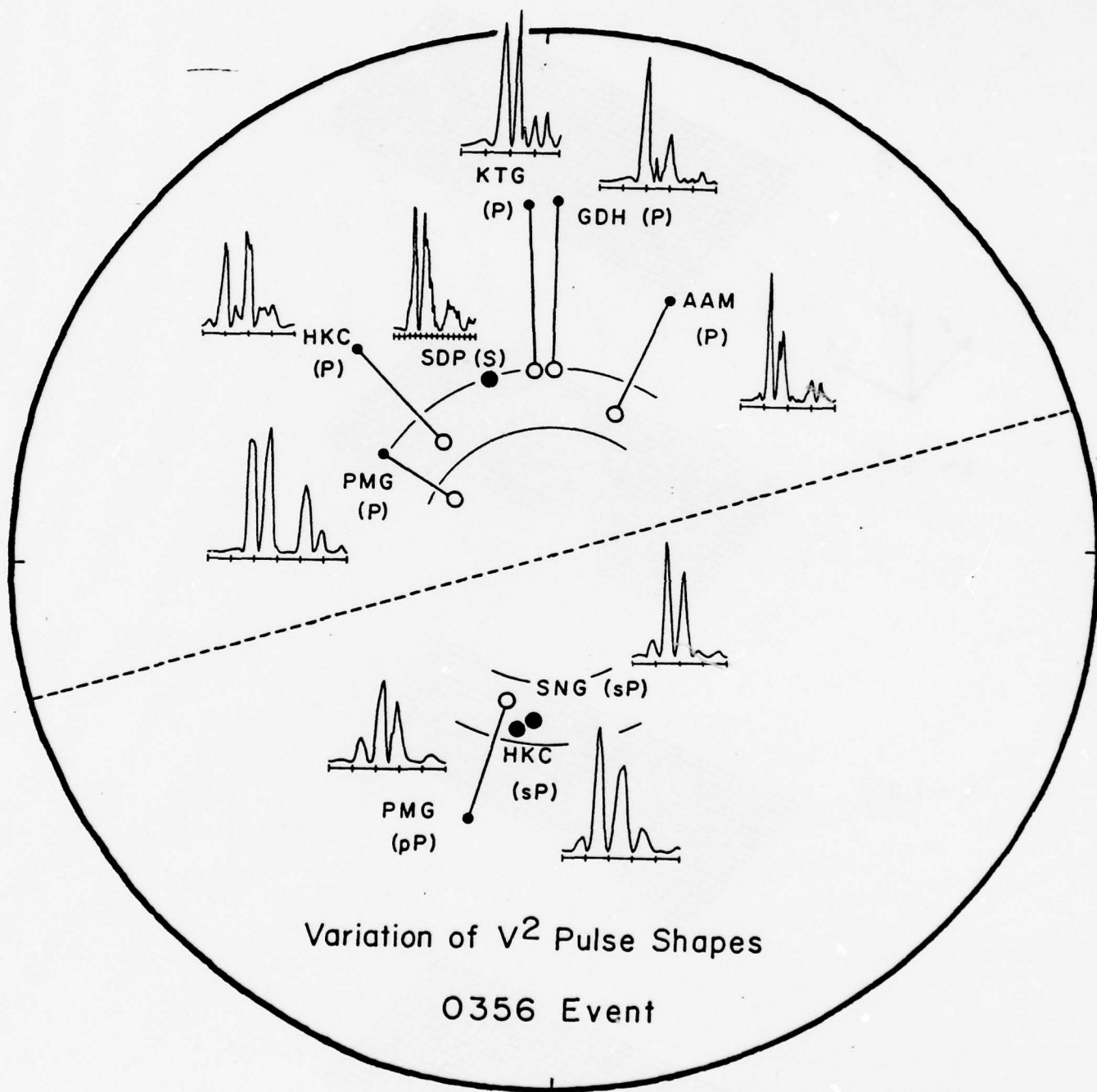


$$t = 1.0 \frac{a}{v}$$



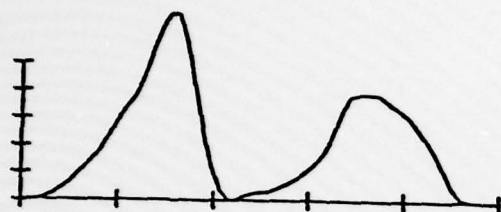
$$t = 1.2 \frac{a}{v}$$



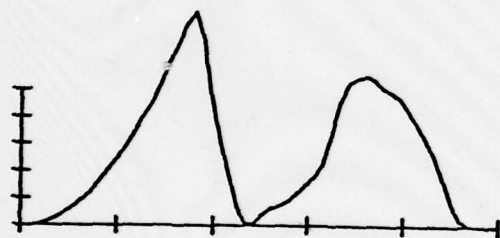


MODEL VARIATION OF SHEAR WAVE v^2 PULSE SHAPES ($\theta_\beta \approx 30^\circ$)

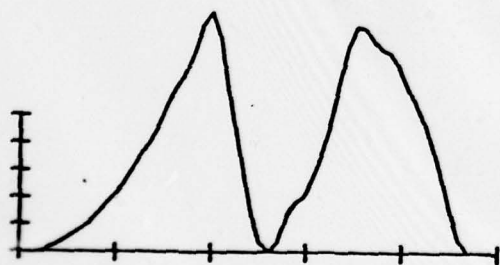
CIRCULAR MODELS



$v = .7\beta$



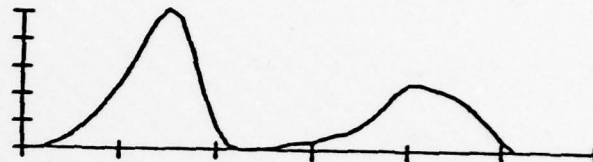
$v = .6\beta$



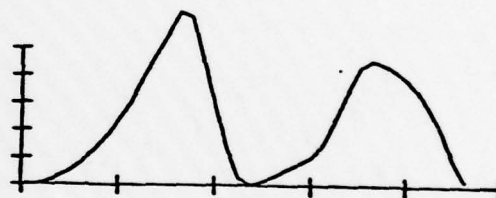
$v = .5\beta$

ASYMMETRICAL MODELS

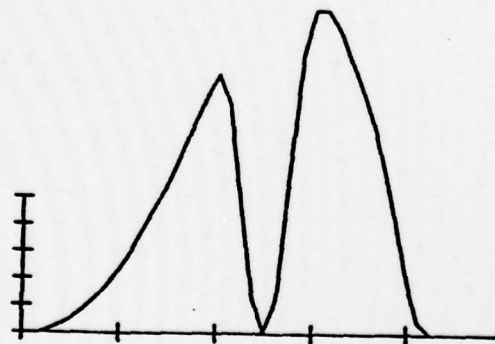
($v = .6\beta$)



rupture away from observer



rupture normal to observer



rupture towards observer

BODY WAVE ANALYSIS OF THE ST. ELIAS EARTHQUAKE

In order to investigate the complexity of this earthquake, it is useful to consider both P and S body waves in the period range from 2 secs to 50 secs. Using three WWSSN long-period seismograms and the 1-75 Benioff seismograms recorded at Palisades, we have established that the earthquake was made up of three distinct sub-events, preceded by a small initial event. The direction of rupture propagation appears to be to the southeast.

In teleseismic body waves from a shallow fault, waveform complications occur through the interference of the depth phases (i.e., the phases reflected from the free surface) and the direct phase. To take out this interference, we construct a free-surface operator, $FSO(t)$, for each body-wave arrival, using the appropriate radiation patterns and reflection coefficients for each phase to determine its relative amplitude. *These radiation patterns are plotted in figure .* The operator is then deconvolved from the actual pulse shapes in order to obtain approximate whole space (AWS) pulse shapes, i.e., pulse shapes without the interference effects of the free surface. The delays of the depth phases were adjusted by minimizing the deconvolutional noise, thereby obtaining an average source depth. This approach presumes that the pulse shapes of the depth phases are identical to the pulse shapes of the direct phases. Since far-field pulse shapes depend only on the vector slowness of the body wave along the fault plane, for a horizontal fault plane the pulse shapes

are identical. Thus this analysis is well suited to earthquakes occurring on very shallowly dipping fault planes.

The steps of the analysis are shown in Figure 1, using the P-wave arrival at station HKC (Hong Kong) as an example. The lowermost trace is the bandpassed long-period seismogram; the trace above it is the deconvolved (from the instrument response) ground velocity. For this arrival, $FSO(t)$ has a positive pulse for the direct P, a very small positive pulse for the pP and a large negative pulse for the sP. The convolutional inverse, labelled $IFSO(t)$, is shown next to it. The result of the deconvolution is the AWS velocity, which is then integrated to obtain the AWS displacement, shown at the top of the figure. The AWS pulse shapes clearly show the three major sub-events, which are labelled 1, 2, and 3. The initial event shows up as a small step in the seismogram which becomes a single bump in the velocity trace.

The AWS pulse shapes for the five body wave arrivals are compiled in Figure 2 along with their epicenter to station azimuths. There is substantial variation with take-off direction and wave-type. The pulse shapes at azimuths away from the direction of rupture propagation, i.e., the HKC P-wave and the KEV S-wave, show the longest pulse rise times (i.e., the time from the onset of event 1 to the peak of event 3), while the PAL S-wave has the shortest. Note that because these pulse shapes depend on the slowness of the body wave, the S-wave pulse shapes vary more strongly than the P-wave pulse shapes. This accounts for some of the dif-

ference between the P-wave and the S-wave at Palisades. The constructive interference of the rupture propagation, as seen in the S-wave pulse shape, smooths the three sub-events into a single pulse. The marked separation of events 2 and 3 in the PAL P-wave may be the result of a slight difference in the focal mechanism of the two events, as this arrival is at a P-pP-sP node.

Using the pulse rise times, $\tau_{1/2}$, of the sub-events, we can calculate their rupture lengths from the relation

$$\tau_{1/2} = \frac{l}{v} \left(1 - \frac{v}{c} \cos \zeta \right)$$

where l is the rupture length, ζ is the angle between the direction of rupture propagation and the takeoff direction of the body wave ^{of velocity c ,} and v is the rupture velocity, assumed to be 2.5 km/sec. This calculation gives $l = 9, 24$ and 16 km for the three events. The PAL S-wave gives a total rupture length of 68 km; however, as the average rupture velocity for the whole event must necessarily be smaller than the rupture velocities of the sub-events, this is an overestimate.

The average rupture depth was determined using the PAL pulse shapes, as the free-surface operators for these arrivals were the most sensitive to the delay times of the depth phases. A sS delay of 6 seconds and a sP delay of 5 seconds gave the least deconvolutional noise, fixing the average ^{source} rupture depth at ≈ 11 km.

The deconvolutional analysis also aids the determination of the body-wave moment, as it coalesces the amplitude information of the direct phase and the depth phases into a single pulse. The moments of the sub-events were calculated to be .8, 3.5 and 7.6×10^{26} dyne-cm, respectively, so that the total body-wave moment is 1.2×10^{27} dyne-cm. The initial event has a moment $< 4 \times 10^{25}$ dyne-cm. Because the pulse shapes for events 2 and 3 are not separated on most of the arrivals, the division of the cumulative moment between these events is somewhat ambiguous.

John Boatwright

Lamont-Doherty Geological Observatory

JB/ma

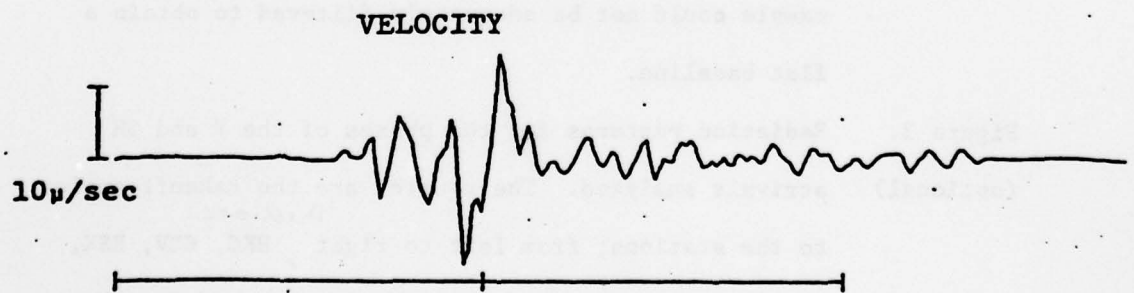
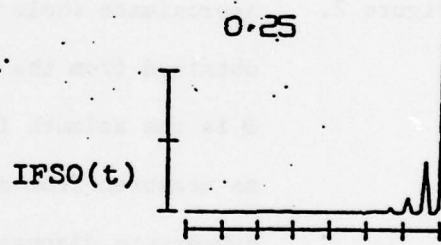
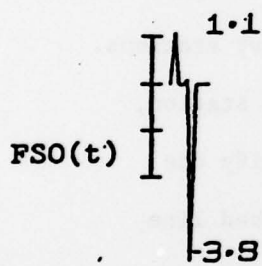
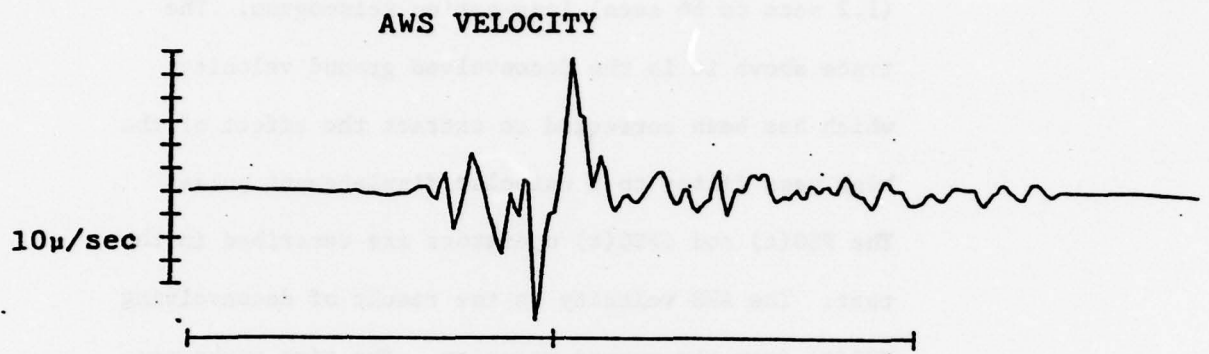
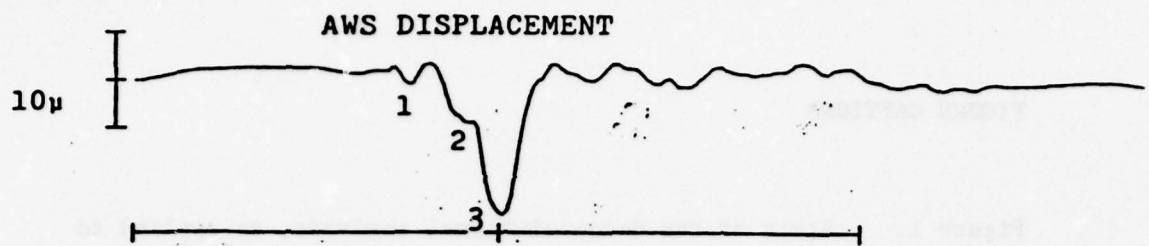
FIGURE CAPTIONS

Figure 1. Steps of the deconvolutional analysis, as applied to the HKC P-wave. The lowermost trace is the bandpassed (1.2 secs to 66 secs) long-period seismogram. The trace above it is the deconvolved ground velocity, which has been corrected to extract the effect of the high pass filter to a unipolar displacement pulse. The FSO(t) and IFSO(t) operators are described in the text. The AWS velocity is the result of deconvolving FSO(t) from the ground velocity. The time marks are at 100 sec intervals.

Figure 2. Approximate whole space displacement pulse shapes, obtained from the body-wave arrivals at four stations. ϕ is the azimuth from the epicenter to the station, as measured from north. The numbers identify the sub-events discussed in the text. The dashed line on the PAL P-wave is the presumed baseline, as the sample could not be adequately filtered to obtain a flat baseline.

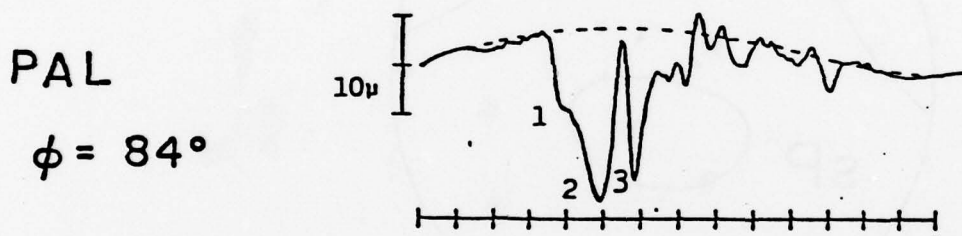
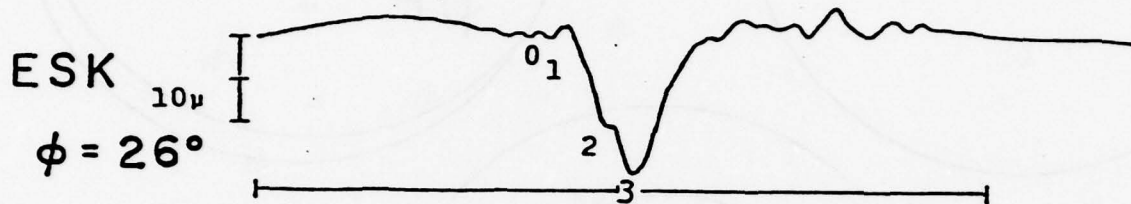
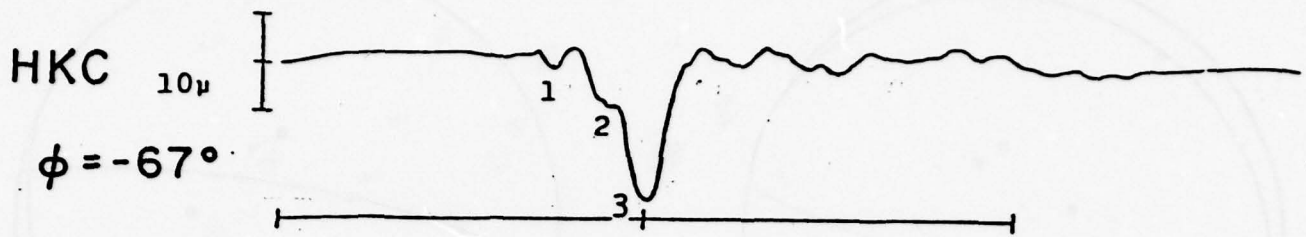
Figure 3. Radiation patterns for the phases of the P and SH (optional) arrivals analyzed. The squares are the takeoff angles ^{These are} to the stations; from left to right HKC, KEV, ESK, and PAL. The sP angles have been corrected for the S-P reflection at the free surface.

P-WAVE AT HKC ON LPZ

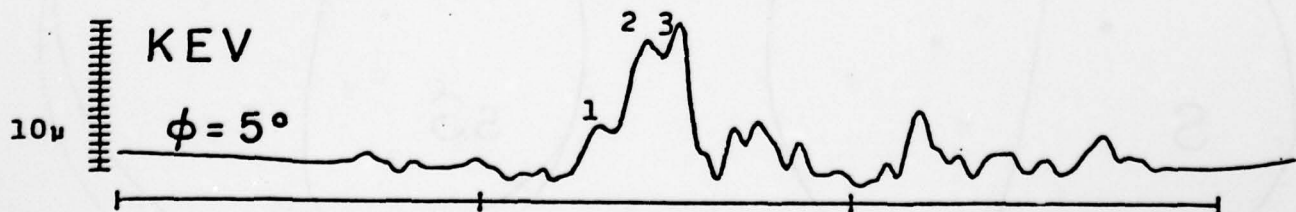
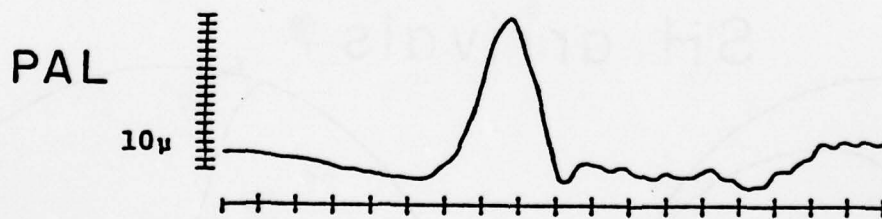


AWS PULSE SHAPES

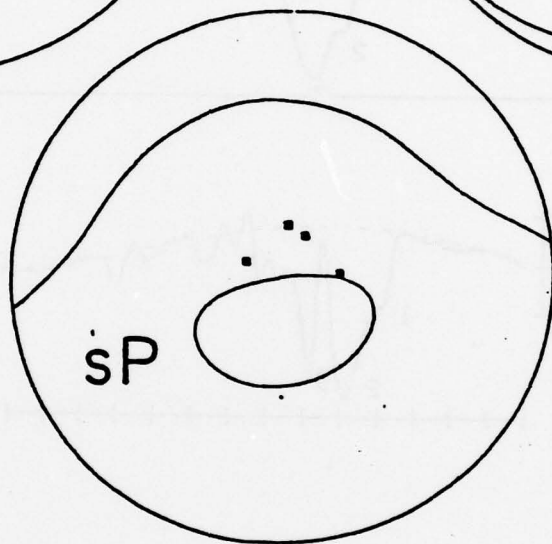
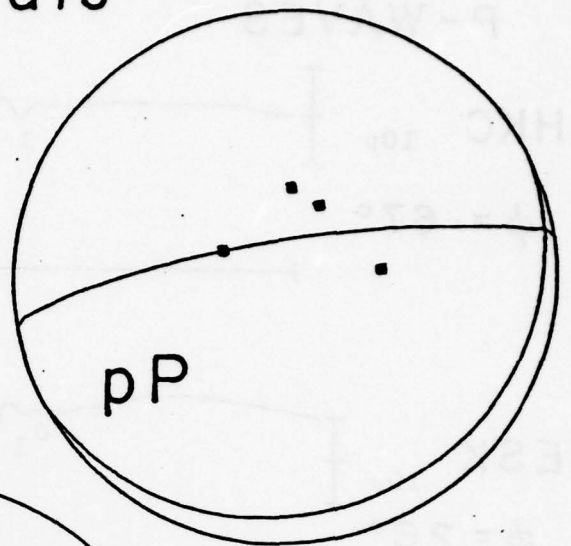
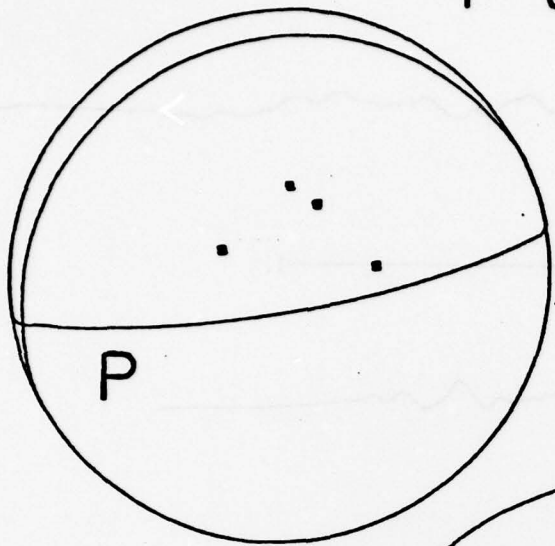
P-WAVES



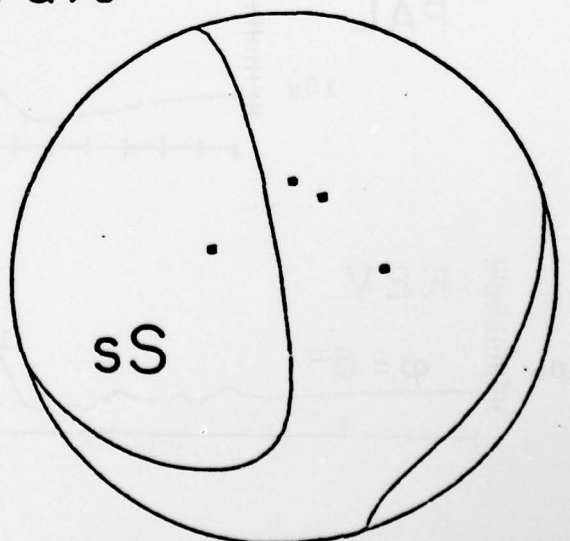
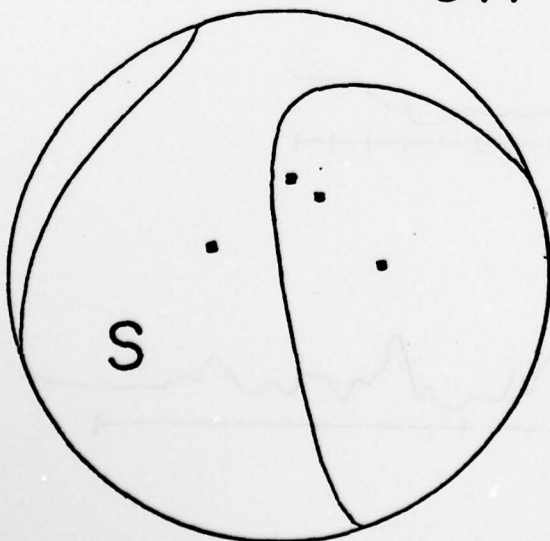
S-WAVES



P arrivals



SH arrivals



ELEMENTARY SOLUTIONS TO LAMB'S PROBLEM FOR A POINT SOURCE AND THEIR RELEVANCE
TO THE STUDY OF SPONTANEOUS CRACK PROPAGATION IN THREE DIMENSIONS

By Paul G. Richards²

ABSTRACT

Certain exact solutions to Lamb's problem (the transient response of an elastic half-space to a force applied at a point) involve the computation merely of three square roots, and about ten arithmetic operations (+, -, \times , \div). They arise when both source and receiver lie on the free surface. It is just these solutions which are needed in a method due to Hamano for obtaining the slip function (displacement discontinuity), as a function of space and time, for planar tension cracks and shear cracks which grow spontaneously with arbitrary shape. The solutions are described here in detail, for an elastic medium with general Poisson's ratio. They include perhaps the simplest-possible example of the \bar{P} wave.

¹ Lamont-Doherty Geological Observatory Contribution Number 0000.

² Lamont-Doherty Geological Observatory and Department of Geological Sciences of Columbia University, Palisades, New York 10964

INTRODUCTION

A thorough understanding of motions in an elastic half-space, subjected to an applied force, is an essential part of wave-propagation theory needed to interpret seismic waves. For this reason, half-space problems have been the subject of an enormous literature, beginning with Lamb's (1904) classic study of displacements set up by forces applied at a point and along a line on the free surface. Here, I give some new solutions, these being the horizontal motions of the free surface for a horizontal force applied as a step in time at a point also in the free surface. (Throughout this paper, the half-space is oriented with a horizontal free surface. Taking cartesian axes with x_3 as the depth coordinate, into the half-space, the free surface is $x_3 = 0$.)

Whatever the value of Poisson's ratio, the new solutions (which augment the work of Pekeris, 1955; Chao, 1960; and Mooney, 1974) are extremely simple to compute. However, these formulas would be only a minor curiosity if it were not for one very important application, in which speed of computation is essential. This application is suggested by Hamano's (1974) method for studying spontaneous crack propagation. Since it is the larger problem of crack propagation which has motivated the present study, I shall in what follows give a brief review of Hamano's method, before giving the simple solutions to Lamb's problem.

MOTIVATION

Within an infinite homogeneous elastic medium, initially at rest, suppose that a crack nucleates at time $t = 0$ and subsequently grows within the plane $x_3 = 0$. Then a useful representation of displacement $\underline{u} = \underline{u}(\underline{x}, t)$ throughout the medium can be given as

$$u_n(\underline{x}, t) = \int_{-\infty}^{\infty} d\tau \int_{-\infty}^{\infty} \int_{-\infty}^{\infty} d\xi_1 d\xi_2 G_{np}(\underline{x}, t-\tau; \xi_1, \xi_2, 0, 0) T_p(\xi_1, \xi_2, \tau). \quad (1)$$

Here, $G_{np}(\underline{x}, t; \xi, \tau)$ is the Green function for the medium, being the n -component of displacement at (\underline{x}, t) due to a unit impulse applied in the p -direction at position ξ and time τ . For purposes of computing G_{np} , it is required that the whole plane $x_3 = 0$ be a traction-free surface. $T(\xi_1, \xi_2, \tau)$ is the actual traction occurring on the whole plane $x_3 = 0$ of which the crack is a part. Equation (1) is described further, and proved, by Das and Aki (1977a) and Aki and Richards (1979, their equation 2.43). Intuitively, the above representation can be understood as replacing the actual (crack) source of radiation by a whole plane, separating the medium into two half-spaces. Into each half-space, waves are radiated due to the same tractions as those set up by the crack, applied over the half-space surfaces. From the space-time element $d\tau d\xi_1 d\xi_2$ there is an applied impulse of strength $d\tau d\xi_1 d\xi_2 T_p(\xi_1, \xi_2, \tau)$ in the p -direction. If the displacement contribution to $u_n(\underline{x}, t)$ from this element is to be considered in isolation from tractions acting elsewhere on $x_3 = 0$, then the appropriate Green function G_{np} must be constrained by having zero traction over the surface of the half-space. Hence, it must be a solution to Lamb's problem.

Hamano (1974) pointed out that for shear cracks and tension cracks, a soluble scheme for the displacement discontinuity $[u]$, say, across the crack can be set up from equation (1) by considering the \underline{x} position itself in the crack plane, $\underline{x} = (x_1, x_2, 0)$, and using symmetry properties of \underline{u} and \underline{T} across $x_3 = 0$ to constrain the displacement and traction on different parts of the plane of the crack.

For a general tension crack, $[u] = [0, 0, u_3]$ and $\underline{T} = (0, 0, T_3)$ so that the only Green function needed is G_{33} .

For a general shear crack, $[u] = [u_1, u_2, 0]$ and $\underline{T} = (T_1, T_2, 0)$ so that the only Green functions needed are G_{11} , G_{12} , G_{21} and G_{22} (see Das and Aki, 1977a, for a related study of two-dimensional cracks). The jump in u_3 is zero, because opposite faces of the crack remain in contact. T_3 is zero, because planar shearing cannot change the normal stress on the crack plane. Together with G_{33} for tension cracks, these five different Lamb problems/Green functions need be studied only for the case that both source and receiver lie in the free surface of the half-space. Hamano's method is important in offering the chance to study spontaneous crack growth for completely general shapes of planar cracking. This paper contributes to that goal, by showing that just these Green functions are almost trivially simple to compute. For completeness, a single integral is also given below, in terms of which the remaining four components, G_{13} , G_{23} , G_{31} , G_{32} , can efficiently be computed.

FORMAL STATEMENT OF PROBLEM, AND ITS SOLUTION

In this section, explicit formulas are derived for $G_{np}^H(x_1, x_2, 0, t; \xi_1, \xi_2, 0, 0)$, this being the n - component of displacement at position $(x_1, x_2, 0)$ and time t ,

within the free surface ($x_3 = 0$) of a homogeneous, isotropic elastic half-space, due to a unit-step force in the p -direction applied also within the free surface, at position $(\xi_1, \xi_2, 0)$, the step occurring at time 0. Once this solution has been found, G_{np} for an impulse (as required in the section above) is given by

$$G_{np}(\underline{x}, t-\tau; \underline{\xi}, 0) = \left. \frac{\partial}{\partial s} G_{np}^H(\underline{x}, s; \underline{\xi}, 0) \right|_{s = t-\tau}$$

Since related problems have had such a wide exposure, I shall abbreviate the description of how a solution is obtained. Thus, in general, the solution to Lamb's problem for a point source can be obtained as an integral over just one variable. In our case,

$$G_{np}^H(\underline{x}_1, \underline{x}_2, 0, t; 0, 0) = \frac{1}{\pi^2 \mu r} \operatorname{Imag} \left\{ \int_1^T \frac{H(T-1)}{(T^2-P^2)^{1/2}} \frac{L_P dP}{[(A-2P^2)^2 + 4XYP^2]} \right\} \quad (1)$$

where μ = rigidity, $r = (\underline{x}_1^2 + \underline{x}_2^2)^{1/2}$, H is the unit Heaviside step function, and capital letters in the integrand denote dimensionless quantities:

$$A = \alpha^2/\beta^2 (\alpha = \text{P-wave speed}, \beta = \text{S-wave speed})$$

$$T = \alpha t/r \quad (T = 1 \text{ being the P-wave arrival time})$$

$$X = (1-P^2)^{1/2} \text{ or } -i(P^2-1)^{1/2}, \quad Y = (A-P^2)^{1/2} \text{ or } -i(P^2-A)^{1/2},$$

$\operatorname{Imag} \{ \}$ denotes the imaginary part of $\{ \}$, and

$$L_{11} = \{ (T^2-P^2)[2Y-4X+(A-2P^2)/Y] + AY \} \cos^2 \phi \\ - \{ T^2[2Y-4X+(A-2P^2)/Y] - AY \} \sin^2 \phi$$

$$L_{12} = L_{21} = (2T^2-P^2)[2Y-4X+(A-2P^2)/Y] \cos \phi \sin \phi$$

$$L_{22} = \{(T^2 - P^2)[2Y - 4X + (A - 2P^2)/Y] + AY\} \sin^2 \phi \\ - \{T^2[2Y - 4X + (A - 2P^2)/Y] - AY\} \cos^2 \phi$$

and

$L_{13}/\cos \phi = L_{23}/\sin \phi = -L_{31}/\cos \phi = -L_{32}/\sin \phi = T(A - 2P^2) - 2TXY$, where ϕ is given by $x_1 = r \cos \phi$, $x_2 = r \sin \phi$, so that ϕ is the azimuth to \underline{x} .

Formula (1) can be written down from Johnson (1974, his equations 26-34, but using $\sqrt{P^2}$ for his $\alpha^2 t^2 r^{-2} - \alpha^2 p^2$). Our variable P is a (dimensionless) horizontal slowness, and (1) is essentially a Cagniard solution in the form advocated by Helmberger (1968). Both source and receiver lie in the free surface, so the Cagniard path lies just above the real P -axis in the complex P -plane (see Figure 1, and caption).

In fact, the P -integrals for G_{11}^H , G_{12}^H , G_{21}^H , G_{22}^H and G_{33}^H can be given in closed form. This is not possible for the four remaining entries in \underline{G}^H , but these four are all proportional to just one integral which is still fairly simple to compute. We note first that

$$\begin{aligned} G_{11}^H(x_1, x_2, 0, t; 0, 0) &= [I_1(T) \cos^2 \phi - I_2(T) \sin^2 \phi] / (\pi \mu r) \\ G_{12}^H &= G_{21}^H = [I_1 + I_2] \cos \phi \sin \phi / (\pi \mu r) \\ G_{22}^H &= [I_1 \sin^2 \phi - I_2 \cos^2 \phi] / (\pi \mu r) \\ G_{33}^H &= I_3(T) / (\pi \mu r) \end{aligned} \quad (3)$$

where arguments have been written out explicitly only for the first of equations (3). Just three functions of dimensionless time are needed to evaluate these five components of \underline{G}^H , namely

$$\begin{aligned}
 I_1(T) &= \frac{1}{\pi} \text{Imag} \left\{ \int_1^T \frac{H(T-1)}{(T^2-P^2)^{1/2}} \left(\frac{(T^2-P^2)[2Y-4X+(A-2P^2)/Y] + AY}{(A-2P^2)^2 + 4XYP^2} \right) PdP \right\} \\
 I_2(T) &= \frac{1}{\pi} \text{Imag} \left\{ \int_1^T \frac{H(T-1)}{(T^2-P^2)^{1/2}} \left(\frac{T^2[2Y-4X+(A-2P^2)/Y] - AY}{(A-2P^2)^2 + 4XYP^2} \right) PdP \right\} \quad (4)
 \end{aligned}$$

and

$$I_3(T) = \frac{1}{\pi} \text{Imag} \left\{ \int_1^T \frac{H(T-1)}{(T^2-P^2)^{1/2}} \left(\frac{AX}{(A-2P^2)^2 + 4XYP^2} \right) PdP \right\}.$$

It follows from (3) that I_1 and I_3 are displacements within the vertical plane containing source and receiver, like the dominant motion in P-SV, whereas I_2 is a displacement transverse to this plane, like the dominant motion in SH. I give analytic expressions below for each of these three integrals. A fourth dimensionless solution to Lamb's problem is introduced via

$$G_{13}^H(x_1, x_2, 0, t; 0, 0) = I_4(T) \cos\phi/(\pi\mu r), \quad (5)$$

$$G_{23}^H = I_4 \sin\phi/(\pi\mu r), \quad G_{31}^H = -I_4 \cos\phi/(\pi\mu r), \quad \text{and} \quad G_{32}^H = -I_4 \sin\phi/(\pi\mu r).$$

The integral for this solution is

$$I_4(T) = \frac{1}{\pi} \text{Imag} \left\{ \int_1^T \frac{H(T-1)}{(T^2-P^2)^{1/2}} \left(\frac{T(A-2P^2) - 2TXY}{(A-2P^2)^2 + 4XYP^2} \right) PdP \right\} \quad (6)$$

which cannot be given in closed form.

For a vertical point force, Pekeris (1955) obtained a closed-form solution for the vertical displacement (our I_3) and a sum of elliptic integrals for the horizontal displacement (our I_4). His solutions were restricted to the case $\alpha^2/\beta^2 = 3$ (Poisson's ratio = 0.25), and Mooney (1974) indicated how the evaluation of I_3 might be carried out for any value of α^2/β^2 (though Mooney did not publish the solution formulas). For a horizontal point force, in a medium with $\alpha^2/\beta^2 = 3$, Chao (1960) obtained closed-form solutions for the horizontal displacements (our I_1 and I_2) and a sum of elliptic integrals for the vertical displacement. Solutions themselves have not previously been given explicitly, for general α^2/β^2 , for any one of the four basic (dimensionless) solutions I_i .

In every case, the basic approach involves writing

$$\frac{1}{(A-2P^2)^2+4XYP^2} = \frac{(A-2P^2)^2-4XYP^2}{(A-2P^2)^4-16X^2Y^2P^4} = \frac{(A-2P^2)^2-4XYP^2}{\text{Cubic}(P^2)} \quad (7)$$

so that the new denominator, of sixth order in P , is real throughout the P -axis integration and has no branch cuts. The imaginary parts of the new integrals are easy to identify (together with a semi-residue contribution to I_4 from indenting around the Rayleigh pole: see Figure 1 caption). If roots R_1, R_2, R_3 are found for the cubic in P^2 , integration for I_1, I_2, I_3 becomes possible using the partial-fraction decomposition

$$\frac{1}{(A-2P^2)^4-16X^2Y^2P^2} = \frac{a}{P^2-R_1} + \frac{b}{P^2-R_2} + \frac{c}{P^2-R_3} \quad (8)$$

The Rayleigh pole lies at $P = R_3^{\frac{1}{2}} = \alpha/\gamma$ (always on the real P-axis, just to the right of $P = \alpha/\beta$, since Rayleigh wave speed γ is a few percent less than β). If Poisson's ratio is less than a critical value, approximately 0.263, then R_1 and R_2 are real and lie between 0 and 1. But, for greater values of Poisson's ratio, R_1 and R_2 are complex conjugates, as are a and b in (8), though c is always real. In this case there are poles in the complex P-plane which can be associated with the so-called \bar{P} wave (Gilbert *et al.*, 1962; Chapman, 1972; Aki and Richards, 1979), appearing between P- and S-arrivals. $R_1^{\frac{1}{2}}$ and $R_2^{\frac{1}{2}}$ lie on a Riemann sheet different from that which contains the Cagniard path.

Substitution of (8) into (7) and (4) leads to 24 integrable terms for each of I_1 and I_2 , and 6 such terms for I_3 . Extensive cancellation does eventually occur. The solutions, involving real positive constants c_j ($j = 1, \dots, 7$) and complex constants C_k ($k = 1, 2, 3$), are as follows:

For times prior to and including the P-arrival, $T \leq 1$,

$$I_1 = I_2 = I_3 = 0. \quad (9)$$

For times between P- and S-arrivals, $1 < T < \alpha/\beta$, there are two different kinds of elastic media to consider. If Poisson's ratio is less than 0.263 (corresponding to $A = \alpha^2/\beta^2 < 3.11$),

$$\begin{aligned} I_1 &= T^2 [c_1 (T^2 - R_1)^{-\frac{1}{2}} - c_2 (T^2 - R_2)^{-\frac{1}{2}} - c_3 (R_3 - T^2)^{-\frac{1}{2}}] \\ I_2 &= -c_4 + c_1 (T^2 - R_1)^{\frac{1}{2}} - c_2 (T^2 - R_2)^{\frac{1}{2}} + c_3 (R_3 - T^2)^{\frac{1}{2}} \\ I_3 &= c_4 - c_5 (T^2 - R_1)^{-\frac{1}{2}} + c_6 (T^2 - R_2)^{-\frac{1}{2}} - c_7 (R_3 - T^2)^{-\frac{1}{2}}. \end{aligned} \quad (10)$$

If Poisson's ratio is greater than 0.263, it is necessary first to define the complex square root (complex, because R_2 is then complex),

$$\text{CROOT} = [(1-R_2)(T^2-R_2)]^{\frac{1}{2}} \quad (11)$$

in which the choice of sign is made such that the complex number $1 + 2(1-R_2 - \text{CROOT})/(T^2-1)$ has magnitude less than unity. Then,

$$\begin{aligned} I_1 &= -T^2 [\text{Real} \{C_1/\text{CROOT}\} + c_3 (R_3-T^2)^{-\frac{1}{2}}] \\ I_2 &= -c_4 - \text{Real} \{C_2 \times \text{CROOT}\} + c_3 (R_3-T^2)^{\frac{1}{2}} \\ I_3 &= c_4 + \text{Real} \{C_3/\text{CROOT}\} - c_7 (R_3-T^2)^{-\frac{1}{2}}. \end{aligned} \quad (12)$$

For times between the S-arrival and the Rayleigh wave arrival, $\alpha/\beta < T < \alpha/\gamma$,

$$\begin{aligned} I_1 &= 0.5 - 2c_3 T^2 (R_3-T^2)^{-\frac{1}{2}} \\ I_2 &= -2c_4 + 2c_3 (R_3-T^2)^{\frac{1}{2}} \\ I_3 &= 2c_4 - 2c_7 (R_3-T^2)^{-\frac{1}{2}} \end{aligned} \quad (13)$$

For times after the Rayleigh arrival, $\alpha/\gamma < T$,

$$I_1 = 0.5$$

$$I_2 = -2c_4 \quad (14)$$

$$I_3 = 2c_4 .$$

Constants in the above solution need be evaluated just once for a given elastic medium, specified by the ratio α^2/β^2 . An effective approach is first to find the largest root R_3 of the Rayleigh cubic; then to factorise $P^2 - R_3$ from the cubic and solve a quadratic for R_1 and R_2 . Constants a, b, c in (8) are given by

$$a^{-1} = 16(A-1)(R_1-R_2)(R_3-R_1)$$

$$b^{-1} = 16(A-1)(R_1-R_2)(R_2-R_3) \quad (15)$$

$$c^{-1} = 16(A-1)(R_3-R_1)(R_2-R_3) .$$

Then

$$c_1 = -2aA(A-R_1)(1-R_1)^{\frac{1}{2}}$$

$$c_2 = 2bA(A-R_2)(1-R_2)^{\frac{1}{2}}$$

$$c_3 = -2cA(R_3-A)(R_3-1)^{\frac{1}{2}}$$

$$c_4 = A/(8A-8)$$

$$c_5 = -2aAR_1(1-R_1)(A-R_1)^{\frac{1}{2}}$$

$$c_6 = 2bAR_2(1-R_2)(A-R_2)^{\frac{1}{2}}$$

$$c_7 = -2cAR_3(R_3-1)(R_3-A)^{\frac{1}{2}}$$

$$C_1 = 4bA(A-R_2)(1-R_2)$$

$$C_2 = 4bA(A-R_2)$$

$$C_3 = bA(A-2R_2)^2(1-R_2).$$

Solutions given above for I_1, I_2, I_3 require at most the evaluation either of three real square roots, or (depending on Poisson's ratio) the evaluation of one complex square root and one real square root. These (worst) cases occur only between P- and S-arrivals. In terms of these closed-form solutions, all the five components of G^H relevant to Hamano's method for studying spontaneous shear and tension cracks can be rapidly computed via (3).

Although I_4 can be given in terms of elliptic integrals (with complex arguments when Poisson's ratio is greater than 0.263), it is probably more efficient directly to integrate as follows:

$$I_4(T) = \begin{cases} 0 & \text{for } T < 1; \\ \frac{2TA}{\pi} \int_0^{\pi/2} \frac{(P^2-1)(A-P^2)^{\frac{1}{2}}(A-2P^2)}{(A-2P^2)^4-16X^2Y^2P^4} dX & \text{for } 1 < T < \alpha/\beta, \\ \text{where } P^2 = (T^2-1) \sin^2\chi + 1; \\ \frac{2TA}{\pi} \int_0^{\pi/2} \frac{(P^2-1)(A-P^2)(A-2P^2)d\psi}{(T^2-P^2)^{\frac{1}{2}}[(A-2P^2)^4-16X^2Y^2P^4]} - \frac{H(T-\alpha/\gamma)c_8 T}{(T^2-R_3)^{\frac{1}{2}}} & \text{for } \alpha/\beta < T, \\ \text{where } P^2 = (A-1)\sin^2\psi + 1. \end{cases} \quad (16)$$

Integrals with respect to χ and ψ here have well-behaved integrands. Note that, at time $T = \alpha/\gamma = R_3^{\frac{1}{2}}$, a singular Rayleigh wave arrives (see Figure 1b

caption) with strength proportional to the positive real constant

$$c_8 = \frac{1}{2}cA(A-2R_3)^3/R_3. \quad (17)$$

In Figure 2 are shown the time-dependences of I_1 , I_2 , I_3 for four different values of α^2/β^2 . We note the following basic properties: (i) Displacements I_1 and I_3 are continuous across the P-arrival, as are I_2 and the particle velocity dI_2/dT . These results follow from (10), (12), and relations between constants appearing in these formulas. (ii) I_1 and I_3 are continuous across the S-arrival, but have discontinuous slopes, whereas I_2 itself is discontinuous. (iii) I_2 is continuous across the Rayleigh-wave arrival time, but I_1 and I_3 are singular. All three solutions are exactly constant after the Rayleigh singularity: these constants must then be the static solutions. (iv) For the horizontal displacement due to a horizontal force, the step (in I_2) at the S-arrival can be seen from (3) as having the orientation of an SH-wave, whereas the singularity (in I_1) at the Rayleigh-arrival occurs as P-SV motion. However, because P-wave motion is not in general exactly longitudinal, the transverse motion (given by I_2) does begin at the P-wave arrival. (v) A \bar{P} wave is apparent in I_3 at times between and P- and S-arrivals, becoming more apparent with increasing values of α^2/β^2 . Since it arises from a single algebraic expression, the term $Real \{C_3/CROOT\}$ in (12), detailed properties of this wave are easy to investigate.

In Figure 3 is shown the time-dependence of I_4 for four different values of α^2/β^2 . Romberg integration was used, requiring occasionally up to 128 intervals for 1% accuracy. There is a discontinuous slope at the P- and S-arrivals; a jump to a singularity at the Rayleigh arrival; and thereafter a gradual decay to the static limit.

CONCLUSIONS

Perhaps the main achievement of this paper is the exact form of constants c_1, \dots, c_8 (positive real, if used) and complex constants C_1, C_2, C_3 , in terms of which the complete solution to Lamb's problem can be given for any orientation of applied force, any displacement component and any value of Poisson's ratio, provided both source and receiver lie in the free surface.

Four scalar solutions in G , involving the cross-terms (vertical or horizontal displacements due respectively to horizontal or vertical applied force), cannot be given in closed form, but a well-behaved integral solution is possible in general.

In the case of horizontal displacements due to a horizontally applied force, the solutions are relevant to a method for studying spontaneous shear cracks. For the case of vertical displacement due to a vertical force, the solution has relevance to tension cracks. In both these cases, solutions (3), (9)-(14), for a step-applied force, are so simple that the following can readily be derived in closed form: (a) solutions for an impulsively-applied force; (b) solutions averaged over $(r, r+\Delta r)$, $(\phi, \phi+\Delta\phi)$ and $(t, t+\Delta t)$; (c) 14 of the displacement fields $\partial G_{np}/\partial \xi_q = G_{np,q}$ due to a single-couple. Specifically, we can use reciprocity on G_{np} so that the derivative is conducted with respect to receiver coordinates. From the five closed-form solutions in G , 10 single-couple displacement fields can be obtained by differentiating in the 1- and 2-directions, parallel to the free surface. The solutions for $(n,p,q) = (1,3,3), (2,3,3), (3,1,3)$ and $(3,2,3)$ can also be recovered in closed form, by using the linear strain constraints at a stress-free surface.

The simplicity of the five scalar solutions in G , which are associated with Hamano's method for studying cracks, is so remarkable that it gives high hopes of successful development of a 3-dimensional study of spontaneous shear and tension fractures.

ACKNOWLEDGEMENTS

This paper originated from conversations with Shamita Das, who is now engaged at Lamont-Doherty in applying Hamano's method in three dimensions. I thank both her and Bill Menke for help with identifying some of the fundamental integrals. Critical reviews from Shamita Das and Klaus Jacob are appreciated. Support for this work came from the Advanced Research Projects Agency of the Department of Defense, monitored by the Air Force Office of Scientific Research under Contract F49620-77-C-0098.

REFERENCES

- Aki, K. and P.G. Richards (1979). Quantitative Seismology: Theory and Methods, ~1800 p., W.H. Freeman and Company, San Francisco, California, (in press).
- Chao, C.-C. (1960). Dynamical response of an elastic half-space to tangential surface loadings, J. Appl. Mech., 27, 559-567.
- Chapman, C.H. (1972). Lamb's problem and comments on the paper 'On leaking modes' by Usha Gupta, Pure Appl. Geophys., 94, 233-247.
- Das, S. and K. Aki (1977). A numerical study of two-dimensional spontaneous rupture propagation, Geophys. J. R. astr. Soc., 50, 643-668.
- Gilbert, F., S.J. Laster, M.M. Backus and R. Schell (1962). Observations of pulses on an interface, Bull. Seism. Soc. Am., 52, 847-868.
- Hamano, Y. (1974). Dependence of rupture time history on the heterogeneous distribution of stress and strength on the fault plane [Abst.], EOS, Trans. Am. Geophys. Un., 55, 352.
- Helmburger, D.V. (1968). The crust-mantle transition in the Bering Sea, Bull. Seism. Soc. Am., 58, 179-214.
- Johnson, L.R. (1974). Green's function for Lamb's problem, Geophys. J. R. astr. Soc., 37, 99-131.
- Lamb, H. (1904). On the propagation of tremors over the surface of an elastic solid, Phil. Trans. R. Soc. Lond., A203, 1-42.
- Mooney, H.M. (1974). Some numerical solutions for Lamb's problem, Bull. Seism. Soc. Am., 64, 473-491.
- Pekeris, C.L. (1955). The seismic surface pulse, Proc. Nat. Acad. Sci., 41, 469-480.

FIGURE CAPTIONS

Figure 1: The Cagniard integration path for (1), (4) and (6) is shown as a solid heavy line. Singularities of these integrands are shown in (a). They consist of branch cuts trending to the right along the real P-axis from points 1 and α/β , and a pole at α/γ (γ being the Rayleigh wave speed). As well as the pole at $\alpha/\gamma = R_3^{1/2}$, we also show schematically the poles at $R_1^{1/2}$, $R_2^{1/2}$ in the right half-plane. R_1 , R_2 and R_3 are roots of the Rayleigh cubic in P^2 , $(A-2P^2)^4 - 16X^2Y^2P^4 \equiv 16(1-A)(P^2-R_1)(P^2-R_2)(P^2-R_3)$. For $A < 3.11$, R_1 and R_2 are real and lie between 0 and 1. But for $A > 3.11$, R_1 and R_2 are complex conjugates. Accurate locations for different A are given in Figure 3b.

In (b) is shown a path of integration in the vicinity of the Rayleigh pole. In the limit, as the semi-circle radius shrinks to zero, integration reduces to a principal value integration plus $-i\pi \times$ residue at the Rayleigh pole. The residue is imaginary from the integrands (4) of I_1 , I_2 , I_3 , and hence gives zero net effect when the imaginary part is evaluated after multiplication by $-i\pi$. But the residue from integrand (6) for I_4 is real, leading to a non-zero contribution from the Rayleigh pole when $T > \alpha/\gamma$.

Figure 2: Here are shown the fundamental time-dependences of displacement for (a) I_1 , the longitudinal horizontal displacement for a horizontally-applied force; (b) I_2 , the transverse horizontal

displacement for a horizontally-applied force; and (c) I_3 , the vertical displacement for a vertically-applied force. We have chosen to plot values of I_3 positive downwards, so that upward values in (c) correspond to $-I_3$, and hence to the convention common in seismology of recording vertical motions as positive upwards.

In each case, the time-dependence is worked out for four different values of α^2/β^2 . Time for these four cases is scaled so that P-arrivals (at $T = 1$) and S-arrivals (at $T = \alpha/\beta$) are aligned. Values are plotted, as heavy solid lines, only between amplitudes ± 1 . I_1 and I_3 in fact are singular at the Rayleigh arrival (marked R), thereafter jumping immediately to the static value.

Dotted lines give values of I_1, I_2, I_3 scaled up by a factor of 15, and hence display the detailed time-dependence at low amplitudes.

Figure 3:

(a) Values of the fundamental solution I_4 as a function of time. A closed-form solution is not possible in this case. Computation is for four different ratios of α^2/β^2 . Dotted lines show values of $15 \times I_4$.

(b) Since T can be regarded as a value of P , the dimensionless horizontal slowness, we have here shown the complex P -plane with the same scale as the T axis in (a), and Figure 2a,b,c. Values of $15 \times I_4$ are repeated from (a). Singularities $R_1^{1/2}$, $R_2^{1/2}$, $R_3^{1/2}$ here, for different values of α^2/β^2 , occur then at times (P -values) which are indicative of what turn out to be properties

of the \bar{P} and Rayleigh waves. Thus, $R_2^{1/2}$ for $\alpha^2 = 2\frac{1}{4}\beta^2$ is almost coincident with the ordinary P-wave arrival, making the latter highly impulsive for I_1 and I_3 because of the term in $(T^2 - R_2)^{-1/2}$. At larger α^2/β^2 , the occurrence of complex $R_2^{1/2}$ with real values greater than one leads to the emergent broad pulse between P- and S-arrivals in I_3 and I_4 . It is interesting that such a \bar{P} wave is not apparent for I_1 and I_2 .

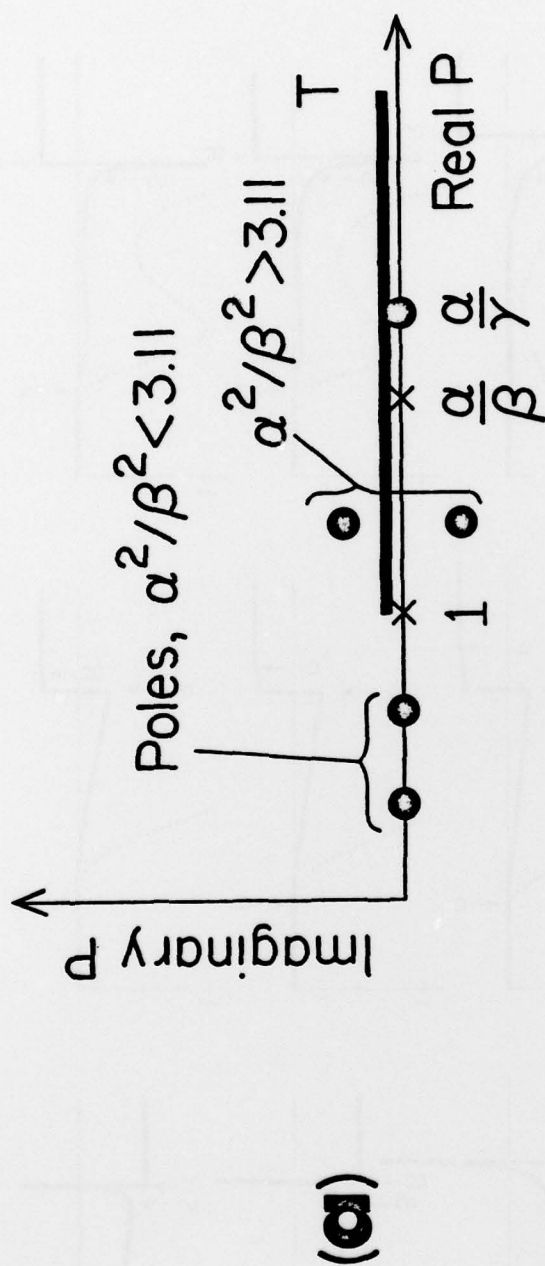


Figure 1

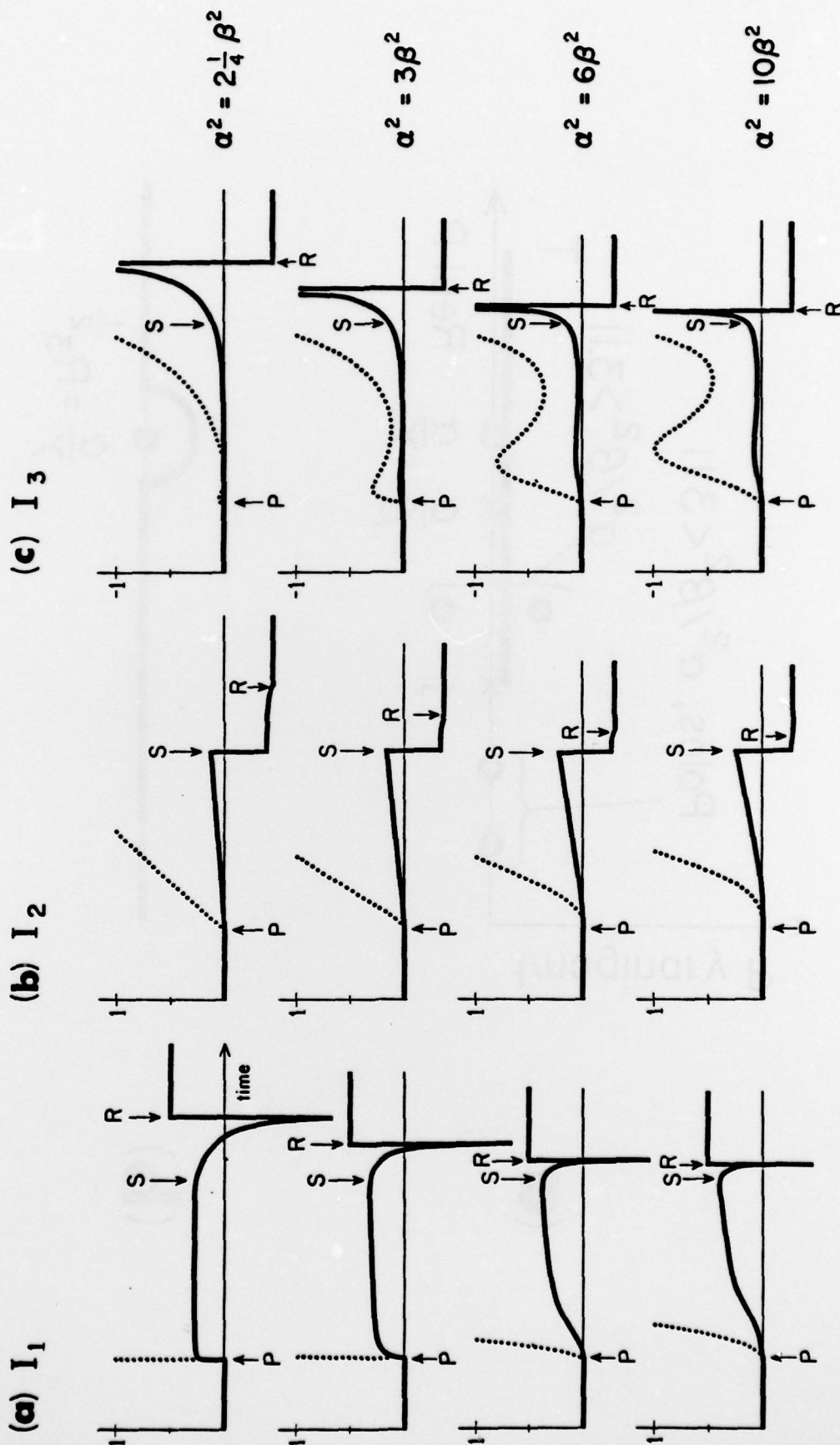
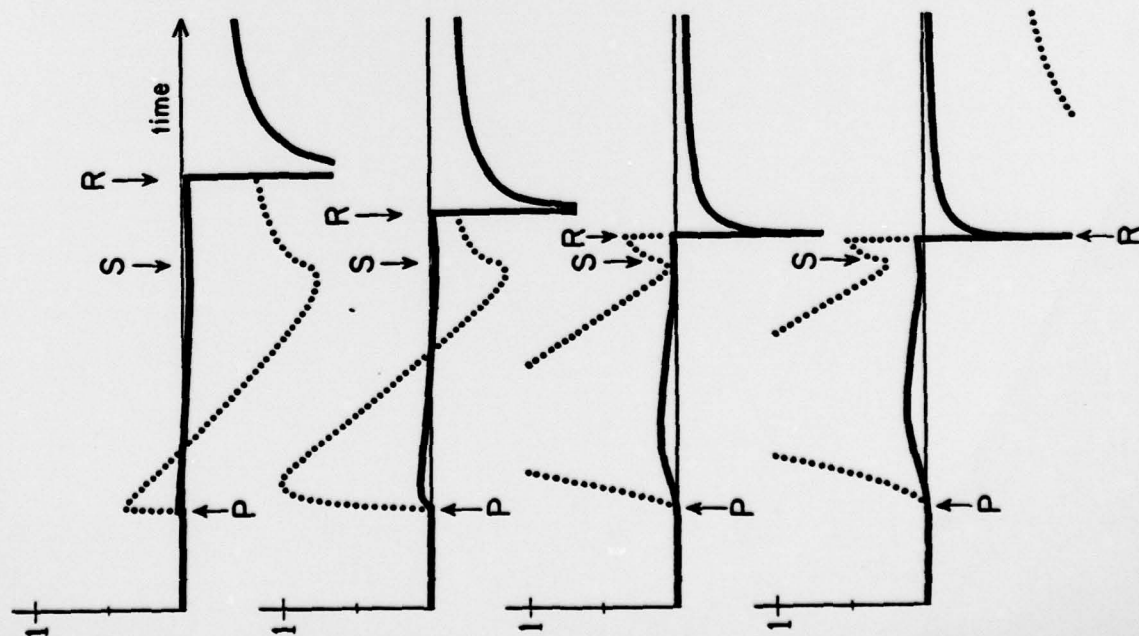


Figure 2

(a) I₄

(b) P-plane

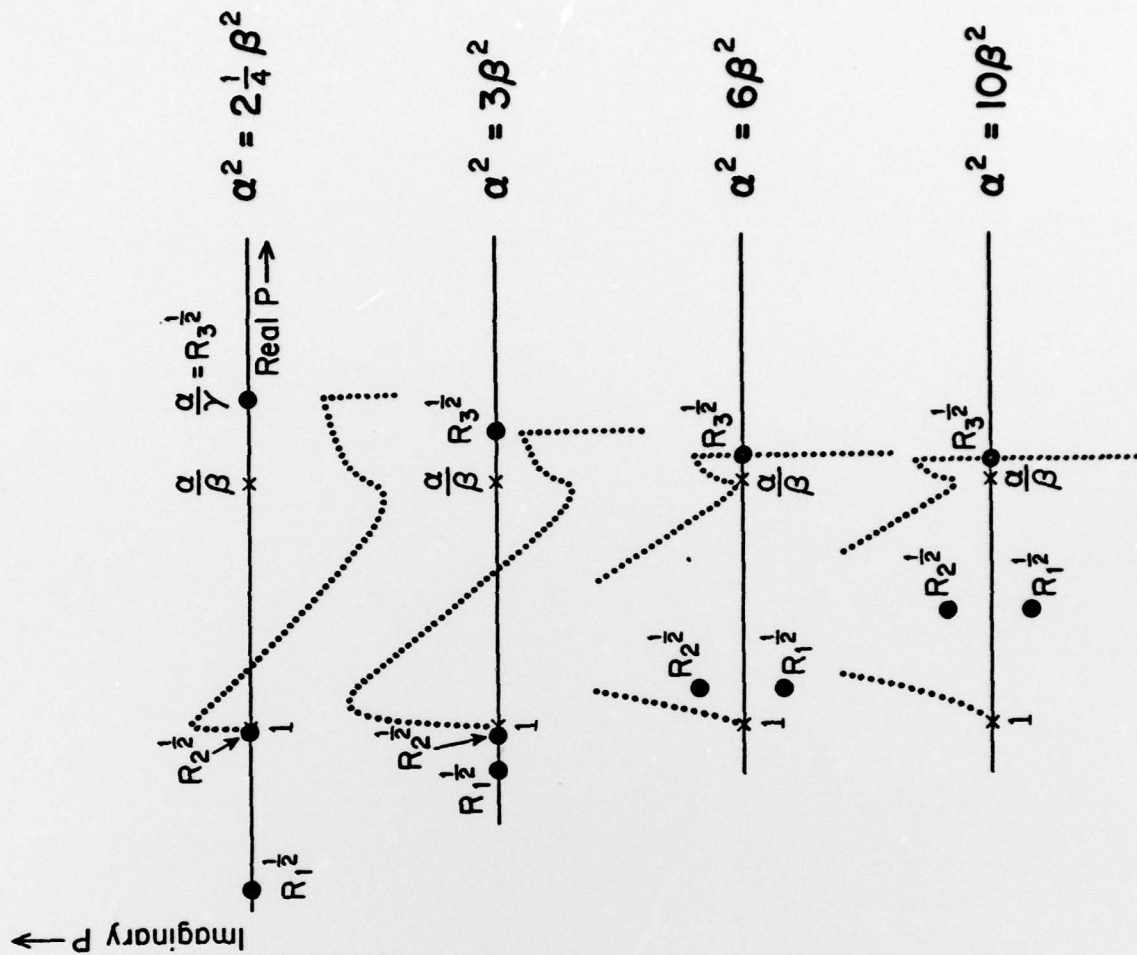


Figure 3